AFRL-VS-HA-TR-2006-1085

# The Loss Cone Imager (LCI)

E. S. Beiser
T. A. Fritz

Boston University
Center for Space Physics
725 Commonwealth Ave.
Boston, MA 02215

Scientific Report No. 1

24 July 2006




AIR FORCE RESEARCH LABORATORY
Space Vehicles Directorate
29 Randolph Road
AIR FORCE MATERIEL COMMAND
Hanscom AFB, MA 01731-3010

## NOTICES

Using Government drawings, specifications, or other data included in this document for any purpose other than Government procurement does not in any way obligate the U.S. Government. The fact that the Government formulated or supplied the drawings, specifications, or other data does not license the holder or any other person or corporation; or convey any rights or permission to manufacture, use, or sell any patented invention that may relate to them.

This report was cleared for public release by the Electronic Systems Center Public Affairs Office and is available to the general public, including foreign nationals. Qualified requestors may obtain additional copies from the Defense Technical Information Center (DTIC) (http://www.dtic.mil). All others should apply to the National Technical Information Service.

AFRL-VS-HA-TR-2006-1085 HAS BEEN REVIEWED AND IS APPROVED FOR PUBLICATION IN ACCORDANCE WITH ASSIGNED DISTRIBUTION STATEMENT.

| //Signed// | //Signed// |
|---|---|
| BRONISLAW DICHTER<br>Contract Manager | JOEL MOZER, Chief<br>Space Weather Center of Excellence |

This report is published in the interest of scientific and technical information exchange, and its publication does not constitute the Government's approval or disapproval of its ideas or findings.

# REPORT DOCUMENTATION PAGE

*Form Approved*
*OMB No. 0704-0188*



| 1. REPORT DATE *(DD-MM-YYYY)* | 2. REPORT TYPE | 3. DATES COVERED *(From - To)* |
|---|---|---|
| 24-07-2006 | Scientific Report No. 1 | 24 Mar 2005 - 24 Mar 2006 |

**4. TITLE AND SUBTITLE**
The Loss Cone Imager (LCI)

**5a. CONTRACT NUMBER**
FA8718-05-C-0013

**5b. GRANT NUMBER**

**5c. PROGRAM ELEMENT NUMBER**
63401F

**6. AUTHOR(S)**
E. S. Beiser and T. A. Fritz

**5d. PROJECT NUMBER**
4400

**5e. TASK NUMBER**
PP

**5f. WORK UNIT NUMBER**
AA

**7. PERFORMING ORGANIZATION NAME(S) AND ADDRESS(ES)**

Boston University
Center for Space Physics
725 Commonwealth Ave.
Boston, MA 02215

**8. PERFORMING ORGANIZATION REPORT NUMBER**

**9. SPONSORING / MONITORING AGENCY NAME(S) AND ADDRESS(ES)**
Air Force Research Laboratory
29 Randolph Road
Hanscom AFB, MA 01731-3010

**10. SPONSOR/MONITOR'S ACRONYM(S)**
AFRL/VSBXR

**11. SPONSOR/MONITOR'S REPORT NUMBER(S)**
AFRL-VS-HA-TR-2006-1085

**12. DISTRIBUTION / AVAILABILITY STATEMENT**
Approved for Public Release; Distribution Unlimited.

**13. SUPPLEMENTARY NOTES**

**14. ABSTRACT**

The Loss Cone Imager (LCI) will serve as an integral component for an Air Force research Laboratory (AFRL) experiment called WPIx. The WPIx experiment will be flown on the Demonstration and Science Experiment (DSX) spacecraft, to be launched in 2009, with a nominal one-year mission. The LCI will measure the local population of energetic particles, concentrating on determining their intensity within the magnetospheric loss cone. The LCI will be able to measure fluxes, energy and pitch angle of energetic electrons from 30 keV to approximately 75 keV to 60 MeV.

**15. SUBJECT TERMS**
Space particles, Electrons, Pitch angle distribution

| 16. SECURITY CLASSIFICATION OF: | | | 17. LIMITATION OF ABSTRACT | 18. NUMBER OF PAGES | 19a. NAME OF RESPONSIBLE PERSON |
|---|---|---|---|---|---|
| a. REPORT | b. ABSTRACT | c. THIS PAGE | | | Bronislaw Dichter |
| U | U | U | SAR | 160 | 19b. TELEPHONE NUMBER *(include area code)* |

## Table of Contents

## 1. SUMMARY

The Loss Cone Imager (LCI) will serve as an integral component for an Air Force Research Laboratory (AFRL) experiment called WPIx. The WPIx experiment will be flown on the Demonstration and Science Experiment (DSX) spacecraft, to be launched in 2009, with a nominal one year mission. The LCI will measure the local population of energetic particles, concentrating on determining their intensity within the magnetospheric loss cone. The LCI will be able to measure fluxes, energy and pitch angle of energetic electrons from 30 keV to 500 keV, and determine the intensity of major ion species over the energy range from approximately 75 keV to 60 MeV.

The LCI concept as proposed by Boston University was selected by AFRL to satisfy its requirements in August 2004, and the contract was finalized in late March 2005. Development of the LCI has been ongoing since, with manufacturing expected to begin in late 2006.

## 2. PROGRESS

The LCI instrument development has made great strides in the past year. The instrument design has evolved significantly from the concept that was presented in the initial proposal. The initial design of the LCI had the instrument placed at the end of one of the spacecraft's 25m booms. However, concern about interference from another payload's high-power transmitting antenna led to the LCI being moved, and split into three components. The initial design was a single electronics box with two rotating sensor heads (RSH) protruding from opposite ends. The current design has the electronics box placed on the spacecraft's payload module (PM), and the two RSH are also mounted on the PM on separate brackets. This redesign, and the intermediary proposed solutions, caused more effort than anticipated to be required in nearly all aspects of the LCI design. We are now committed to this design and work continues to finalize the details.

The LCI team responded to concerns by the Stanford (WIPER) team that the LCI would not be sensitive enough to low count rates, and proposed a High-Sensitivity Telescope (HST) to meet this need. This proposed HST design has been presented to the DSX team and to AFRL/Hanscom, and has been baselined as part of the DSX spacecraft. However, we await funding for this component before proceeding with long-lead item procurement. The motor vendor selection has been an issue of contention. A detailed request for quotation (RFQ) was prepared, and formally released to several vendors. Only one vendor (Starsys) chose to reply, and quoted a cost an order of magnitude higher than what had been budgeted for motors. In need of an alternative procurement route, the vendor Oriental Motors was found. Their products appeal to the LCI team because of their cost, weight, power, design, and performance. Another advantage is their availability. In fact, three of these motors have been purchased and delivered. These motors were referred to the LCI team by an unrelated project that has experience flying them in high-altitude balloon studies. The drawback of using the Oriental motors is that they will need to be

further qualified. As of this writing, two additional motor vendors have been identified that were not part of the initial RFQ process. The LCI team is engaged in discussions with these vendors to evaluate their offerings for suitability to the LCI needs. Both of these vendors have flight heritage, which would obviate the need for qualifying the Oriental motor.

The LCI data processing unit (DPU) will make use of an FPGA device, working with a microcontroller to control the instrument. Initial design efforts planned on using a Xilinx FPGA. However, after more consideration, in particular with respect to radiation tolerance, an Actel part was selected instead. This brings the LCI in line with several other DSX payloads that are using Actel FPGAs. Development has pressed forward with the Actel FPGA. A prototype DPU board layout has been completed and will be ready for interface testing with the ECS during the summer of 2006.

Along with the design effort itself, work has been performed to document the project as requested by the project management office (PMO). Specifically, an interface control document (ICD) has been developed. This document has gone through multiple iterations, each revision incorporating more content and addressing concerns identified by the PMO from the last release. Another document similarly developed is the requirements and test verification matrix (RTVM). At the PMO's urging, we continue to refine these documents to be suitable for release to the DSX team as a whole.
From the start, the LCI has made use of students, supervised by faculty members, to do the design work. The LCI team has been built up over the past year to include four graduate students, and approximately eight undergraduates. At least two graduating undergraduates will continue as graduate students at Boston University in the fall, and will continue to be a part of the LCI team.

The LCI team successfully completed a preliminary design review (PDR) on October 17th, 2005. It was approximately at this time that the PMO provided the current LCI configuration (integrated DPU/HST on the PM, the RSH units on a composite tube, later to become separate mounting brackets). Although PDR was productive in pushing documentation of the project, much of this needed to change as a result of the final decision on LCI placement on the spacecraft.

## 3. UPCOMING ACTIVITIES

The summer of 2006 will be a busy one for the LCI team. A prototype DPU board will be made ready for performing an interface test with the ECS in Melbourne, FL in late July. The ground support equipment (GSE) will also be made available for that test. A full prototype of the RSH electronics boards and detectors will be available for beam testing at NASA/GSFC. This test will subject the detectors to real electron and proton beams, and demonstrate the readout capabilities of the LCI design.

In August, the LCI team will host an intermediate design review (IDR), after which the intention is to begin procurement and fabrication of the prototype/proto-flight hardware.

In anticipation of the start of this effort, several long-lead items have been ordered. These include the thin and thick detectors.

## 4. SUPPLEMENTAL MATERIALS

As part of this report we append documents that have been generated within the BU LCI project. In Appendices A and B we has appended the supplemental proposal and design studies which have defined the High Sensitivity Telescope (HST). The purpose of the HST is to assure that the LCI is able to fulfill DSX L0/L1 requirement 1.7: "DSX shall provide a sensor platform capable of measuring the scattering effect of the VLF transmitter on the trapped electron population into the loss cone" in the event that these fluxes are only 100 electrons/cm$^2$·sec·ster.

Appendices C and D describe aspects of the LCI with have been developed as thesis projects. Appendix C describes the pulse analog electronics of the Rotating Sensor Heads which will form the basis of a PhD thesis of Mr. Qingtai Zhai. Appendix D describes the Ground Support Equipment which will form the basis of a Masters degree thesis for Mr. David Voss. Both of these degrees will be in Electrical and Computer Engineering (ECE).

Appendix E describes testing performed by BU ECE undergraduate Mr. Kurt Matarese on a candidate motor system for the RSH assemblies.

## 5. LIST OF ACRONYMS

| | |
|---|---|
| AFRL | Air Force Research Laboratory |
| BU | Boston University |
| CDR | Critical Design Review |
| DPU | Data Processing Unit |
| DSX | Demonstration and Science Experiments |
| ECS | Experiment Computer System |
| FPGA | Field-Programmable Gate Array |
| GSE | Ground Support Equipment |
| GSFC | Goddard Space Flight Center |
| HSB | Host Spacecraft Bus |
| HST | High Sensitivity Telescope |
| ICD | Interface Control Document |
| IDT | Instrument Development Team |
| LCI | Loss Cone Imager |
| PDR | Preliminary Design Review |
| PMO | Project Management Office |
| RENA | Readout Electronics for Nuclear Applications |
| VMAG | Vector Magnetometer |
| WIPER | Wave-Induced Precipitation of Electron Radiation |
| WPIx | Wave-Particle Interaction eXperiment |

# APPENDIX A: HST PROPOSAL

Proposal Title

# The High Sensitivity Telescope, HST

## Supplemental Proposal for the DSX LCI effort at Boston University

Request for funding for period:
January 1, 2006 to September 30, 2008

Submitted to:

Air Force Research Laboratory
AFRL/VSBXR
29 Randolph Rd,
Hanscom, AFB, MA 01731-3010
Telephone: 781-377-3991

Submitted by:
**The Trustees of Boston University**


**Theodore A. Fritz**
**Principal Investigator**

**Institutional Endorsement**

Institution:
Center for Space Physics
Boston University
725 Commonwealth Ave.
Boston, MA 02215
Telephone: 617-353-7446
Fax: 617-353-6463


February 6, 2006

Funding Requested: $251,987

**Background Information**

The US Air Force Demonstration and Science Experiments (DSX) project has a stated requirement documented in the L0/L1 requirements document, section 1.7: "DSX shall provide a sensor system capable of measuring the scattering effect of the VLF transmitter on the trapped electron population into the loss cone." The LCI instrument as proposed is fully capable of meeting this requirement while maintaining a non-saturated sensitivity to the overall maximum electron intensities. In the PRDA the following additional information was provided in section **2.2.4 Loss Cone Electron Detector:**

**Knowledge of the loss cone electrons (100 to 500 keV with velocity nearly parallel to the local magnetic field) is needed to understand and quantify the effects of the transmitter on the scattering of the trapped electron population into the loss cone. The field-of-view must be less than 10 degrees since the loss cone angle is about 16 degrees at the DSX altitudes. Expected loss cone fluxes are of the order of 100 to 10,000 electrons / cm^2-sec-sr at E = 300 keV, with E falling off as exp(-E/150) with E in keV.**

**Figure 1: Size of the loss cone**

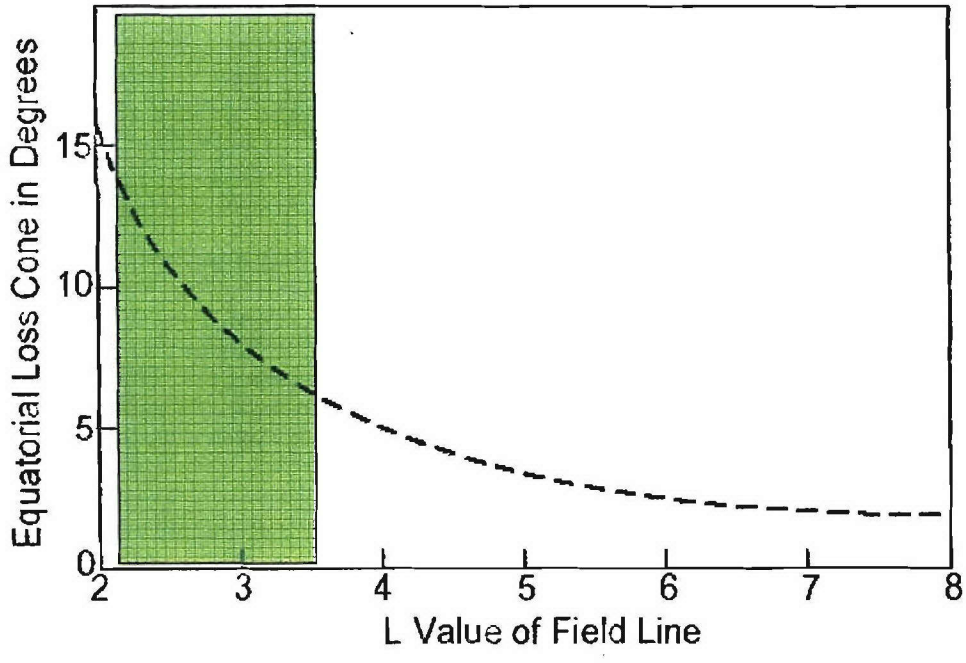


The geometric factor of the rotating head assemblies of the Loss Cone Imager (LCI) is sized to permit unsaturated operation over the full three-dimensional distribution of the energetic electron fluxes to be encounter along the trajectories of the DSX satellite. Such fluxes are anticipated to have a peak value of $4 \times 10^8$ electrons/cm$^2$ sec greater than 40 keV. The LCI rotating sensor assemblies will be operating in excess of $10^5$ counts/sec for such fluxes. It is therefore not possible to increase the geometric factor of these sensors without saturating their responses to the anticipated full distribution. In the loss cone

these sensors should be able to detect fluxes of 10,000 electrons/cm$^2$ sec ster but will only respond at rates of 0.01 to 0.1 counts/sec at lower limit value of 100 electrons/cm$^2$ sec ster. In order to be able to detect fluxes at the lower end of the range specified above it is necessary to design a separate sensor that will have an adequate geometric factor.

**The High Sensitivity Telescope**

We propose to develop a High Sensitivity Telescope (HST) with a geometric factor of 0.1 cm$^2$ ster capable of detecting fluxes at the lower limit specified above. The loss cone is defined to be that range of particle pitch angles whose mirror point will occur at 100 km or lower and therefore will be lost to the atmosphere. The edge of the loss cone is defined to be the equatorial pitch angle corresponding to a particle mirroring at 100 km. Figure 1 presents the range of such pitch angles corresponding to edge of the loss cone as a function of radial distance with the interval in green being that range covered by the DSX satellite. In order to only detect fluxes of particles in the loss cone over the range of projected DSX altitudes, the field of view of the proposed telescope needs to be of 7 degrees opening half angle if it can be oriented to view only along the geomagnetic field vector direction. Increasing the geometric factor has the additional feature that it also increases the sensor sensitivity to penetrating radiation that produces a background response that could easily mask the foreground loss cone fluxes that must be measured. This requires that the sensor must have adequate shielding.

Prof. James D. Sullivan has conducted a series of studies using a particle energy loss code known as GEANT3 and these are described in his memos that are included here in the Appendix. In summary the response of such a High Sensitivity Telescope (HST) to omni-directional fluxes has been computed by placing the active detectors, a 35mm diameter, 1500 μm silicon detector in front of a 40mm diameter, 1000 μm anticoincidence detector, in two closed shielding boxes with an outer shell of aluminum (Al) and an inner shell of tungsten (W), with sufficient thickness to stop an 80 MeV proton. The flux is assumed isotropic over the outer surface of the box. The memos in the Appendix describe the shielding thickness and the evaluation of the background response of this configuration to penetrating radiation. The conclusion of this evaluation is that it should be possible under almost all circumstances to measure a minimum flux in the loss cone of 100 electrons/cm$^2$ sec ster. The proposed design concept is given in Figure 2 and the nominal orientation on the HST on the DSX satellite is shown in Figure 3. We are projecting that this sensor will have a mass of not-to-exceed 7.6 kg which includes presently a contingency of approximately 2 kg.

In discussions with the PMO and the WIPER team it was decided to sample the loss cone fluxes with the HST in six energy channels over an energy range of 20 keV to about 700 keV. These channels are given in Figure 5 below. The integral response above the lowest energy threshold can be provided directly to a possible particle correlator for high time resolution sampling. An additional request by Dr. Martin Walt of the WIPER team to provide higher energy resolution than that provided by the six discrete channels was made as well. An eight-bit analog-to-digital (ADC) converter was incorporated into the

**Figure 2: Dimensional schematic of the proposed HST**

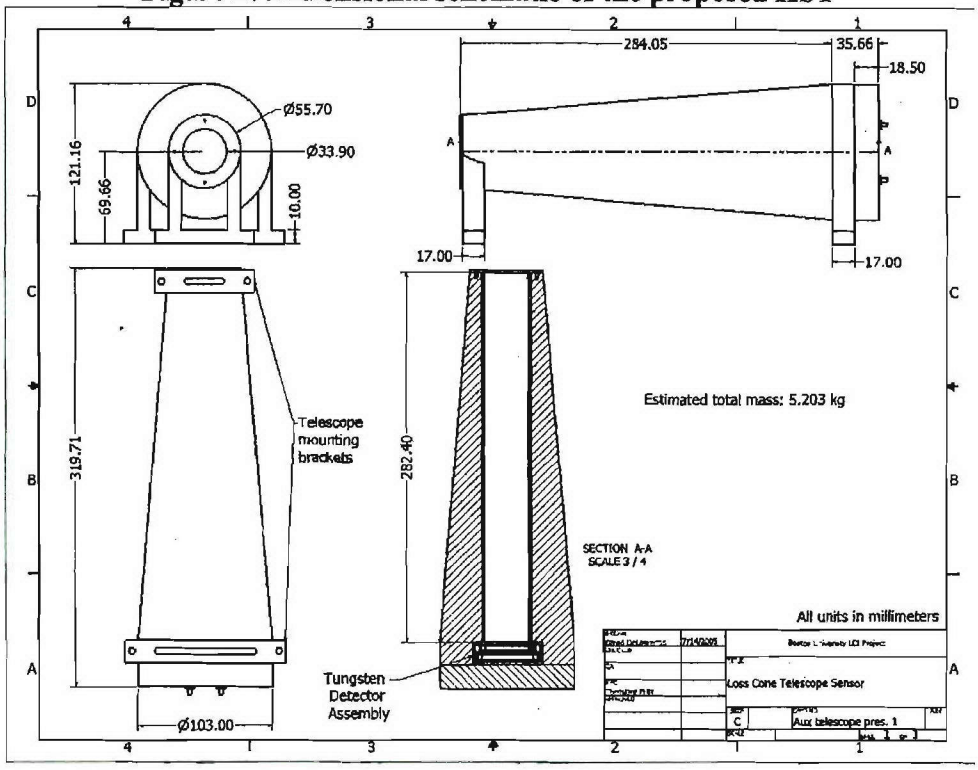


**Figure 3: HST orientation with respect to DSX s/c coordinate axes**

**DSX s/c coordinates**

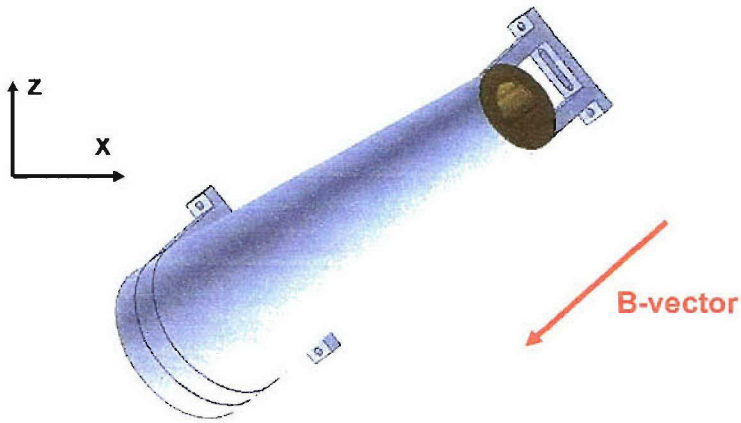

**Figure 4: HST Energy Channels and Boolean Logic**

| Energy Range | Logic |
|---|---|
| 20~40keV | A0•A1•B |
| 40~80keV | A1•A2•B |
| 80~160keV | A2•A3•B |
| 160~320keV | A3•A4•B |
| 320keV~700keV | A4•B |

**Figure 5: the HST Sensor Electronics Block and Timing Diagram**

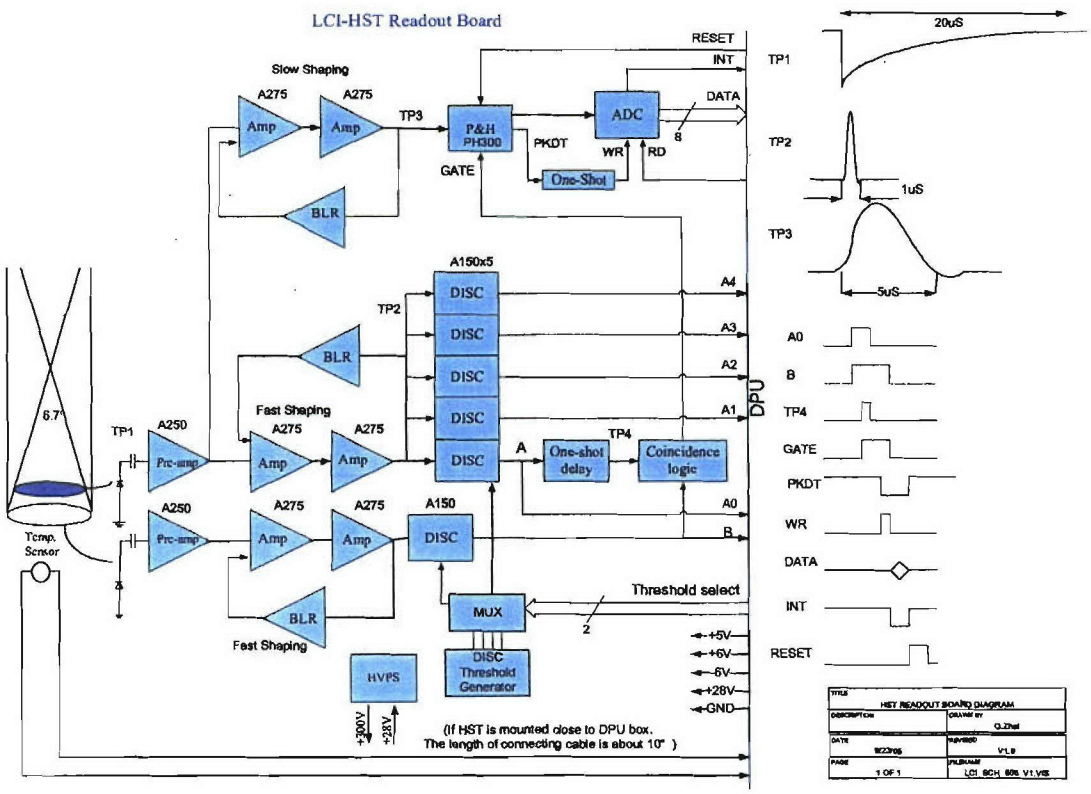

design and will permit the energy spectrum of the loss cone fluxes to be sampled at an energy resolution of a few keV with a flexible sampling rate. The block diagram of the electronics of the proposed sensor is presented in Figure 6. The design of the HST electronics utilizes hybrid packaged devices manufactured by AMPTEK, Inc. to provide charge-sensitive pre-amps, amplifiers, discriminators, and baseline restorers as shown. The components shown form the basis of the requested funding given in the spreadsheet at the end of this proposal for supplemental funding.

**Appendix: Working Memos of James Sullivan**

Working Memo #8: Remarks on required shielding thickness (32 pages)

Working Memo #10: LCI Auxiliary Telescope Response (11 pages)

## Remarks on required shielding thickness

The shielding thickness necessary to reduce the omni-directional counting rate to a given value is given in Table 1.

| Rate, $s^{-1}$ | Flux, $cm^{-2}\,s^{-1}$ | AE8MAX, Emin, MeV $F(> E_{min})$ <Flux | Al thickness mm | AP8MAX, Emin, MeV $F(> E_{min})$ <Flux | Al thickness mm |
|---|---|---|---|---|---|
| $2 \times 10^5$ | $1.2 \times 10^4$ | 3.7 | 2.7 | 25 | 3.2 |
| $1 \times 10^5$ | $5.9 \times 10^3$ | 4.1 | 3.0 | 30 | 4.4 |
| $5 \times 10^4$ | $3.0 \times 10^3$ | 4.5 | 3.3 | 40 | 7.3 |
| $2 \times 10^4$ | $1.2 \times 10^3$ | 5.1 | 3.8 | 60 | 15.1 |
| $1 \times 10^4$ | $5.9 \times 10^2$ | 5.5 | 4.1 | 80 | 25 |
| $5 \times 10^3$ | $3.0 \times 10^2$ | 6.0 | 4.3 | | |

Table 1: Shielding thickness: $L \in [2.0, 3.0]$; $B/B_0 \in [1, 2.7]$; 5% transmission range for electrons; detector $1.64$ cm in radius and $26.7$ cm high, total (two-sided) $G_{\text{omni}} \approx 53.1\,\text{cm}^2\,\text{sr}$

The equatorial integral flux of electrons and protons from the AE8MAX and AP8MAX models are given in Table 2.

| L | Electron flux, $cm^{-2}\,s^{-1}$ | Proton flux, $cm^{-2}\,s^{-1}$ |
|---|---|---|
| 2.0 | $3.6 \times 10^8$ | $9.5 \times 10^6$ |
| 2.2 | $2.9 \times 10^8$ | $2.0 \times 10^7$ |
| 2.4 | $2.3 \times 10^8$ | $3.3 \times 10^7$ |
| 2.6 | $1.5 \times 10^8$ | $4.8 \times 10^7$ |
| 2.8 | $8.4 \times 10^7$ | $5.9 \times 10^7$ |
| 3.0 | $4.2 \times 10^7$ | $6.1 \times 10^7$ |

Table 2: Electron and proton integral fluxes for $L \in [2, 3]$ and $B/B_0 = 1$; electrons $> 40$ keV and protons $> 0.8$ MeV

The directional geometrical factor is $0.1\,\text{cm}^2\,\text{sr}$ which, assuming isotropy, implies electron ($> 40$ keV) and proton ($> 0.8$ MeV) counting rates of $\sim 1.1 \times 10^7/\text{s}$ and $\sim 2 \times 10^6/\text{s}$, respectively.

**Remark:**

$$C = \mathcal{G}\mathcal{I} = \mathcal{A}\mathcal{F} \quad \textit{and} \quad \mathcal{G} = \pi\mathcal{A} \qquad \textit{so that} \qquad C = \frac{\mathcal{G}}{\pi}\mathcal{F}$$

If the proton threshold is raised to $\sim 2$ MeV then the (peak) flux is only reduced to $\sim 7.7 \times 10^6\,\text{cm}^{-2}\,\text{s}^{-1}$; this corresponds to a minimum range of $\sim 42\,\mu$m which passes 5% of 87 keV electrons. Thus, if the loss cone is even partially filled by protons, then any electron signal in the detector is swamped by *direct* protons.

## Response to collimated signal

The response of the HST detector to a collimated beam is computed by considering normal and oblique (**7°**) rays incident on the telescope approximated by parallel planes of **1000** Å of aluminum on a **0.5** mil mylar foil in front of a **1000** $\mu$m (or **1500** $\mu$m) silicon detector, detector A, followed by a **1000** $\mu$m silicon detector for anti coincidence, detector B. The nominal thresholds are **40** keV of deposited energy (although other levels are presented when defining response windows for A. For the figures presented below, five hundred thousand events were generated using GEANT3 for each histogram so that there are one thousand primary events per (energy) bin.

Shown in Figures 1 and 2 is the probability that an electron at normal incidence will be counted in one of the desired energy bands for a **1000** $\mu$m A. For electrons incident at **7°** the corresponding results are shown in Figures 3 and 4. For a results for a thicker detector, **1500** $\mu$m A, are shown in Figures 5 and 6.

Shown in Figures 7 and 8 (blown up in Figures 9 and 10) is the probability that a proton will be counted in one of the desired energy bands for a **1000** $\mu$m A. The blown up figures are statistics limited. For protons incident at **7°** the corresponding results are shown in Figures 13 and 14. For a results for a thicker detector, **1500** $\mu$m A, are shown in Figures 11 and 12.

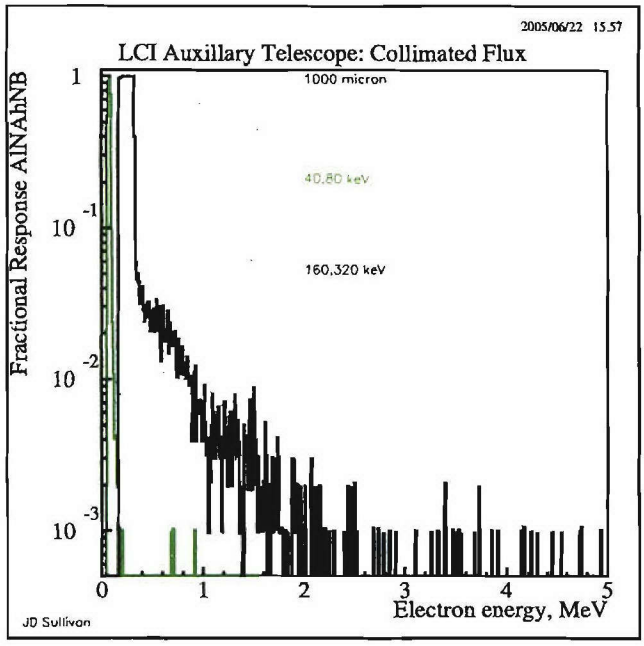


Figure 1: Probability that an electron of given energy will not trigger B while depositing either 40–80 keV or 160–320 keV in A

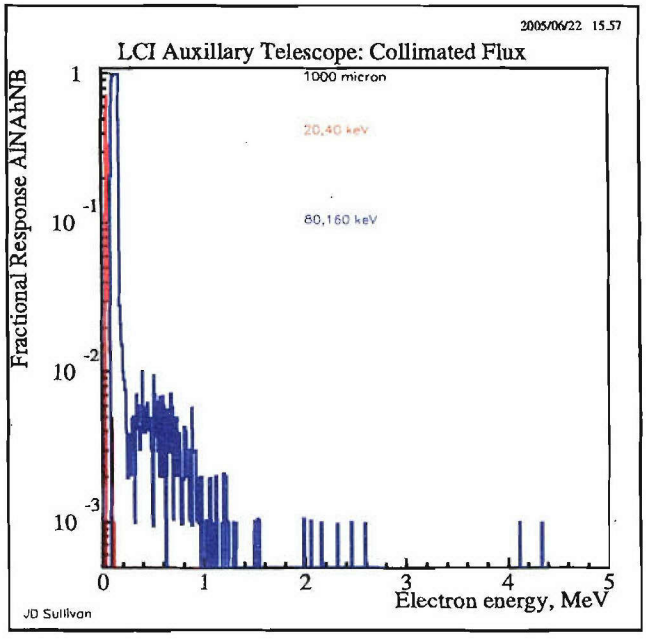


Figure 2: Probability that an electron of given energy will not trigger B while depositing either 20–40 keV or 80–160 keV in A

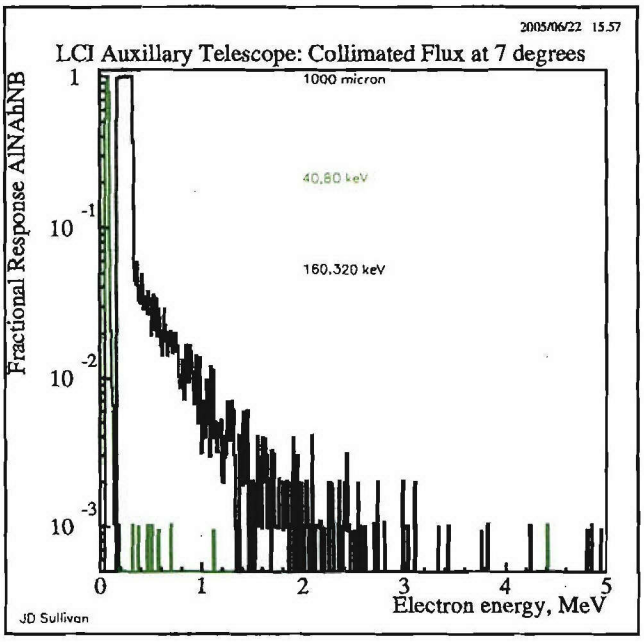


Figure 3: Probability that an oblique electron of given energy will not trigger B while depositing either 40–80 keV or 160–320 keV in A

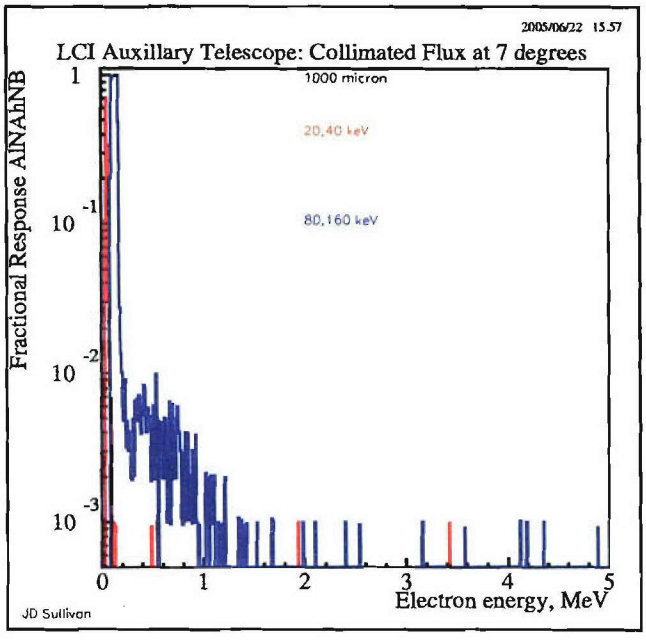


Figure 4: Probability that an oblique electron of given energy will not trigger B while depositing either 20–40 keV or 80–160 keV in A

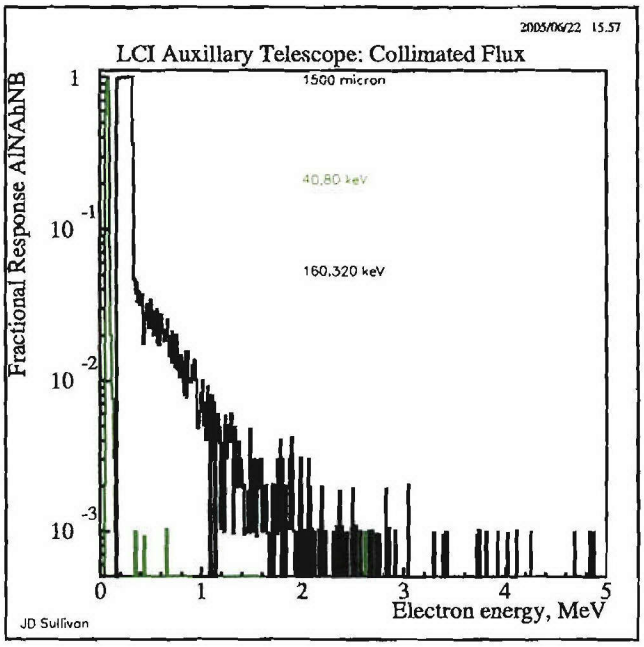


Figure 5: Probability that an electron of given energy will not trigger B while depositing either 40–80 keV or 160–320 keV in **1500** $\mu$m A

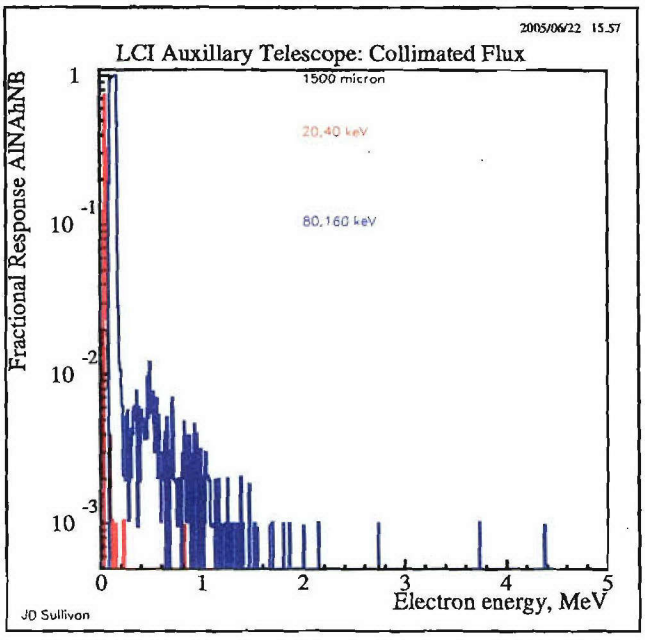


Figure 6: Probability that an electron of given energy will not trigger B while depositing either 20–40 keV or 80–160 keV in **1500** $\mu$m A

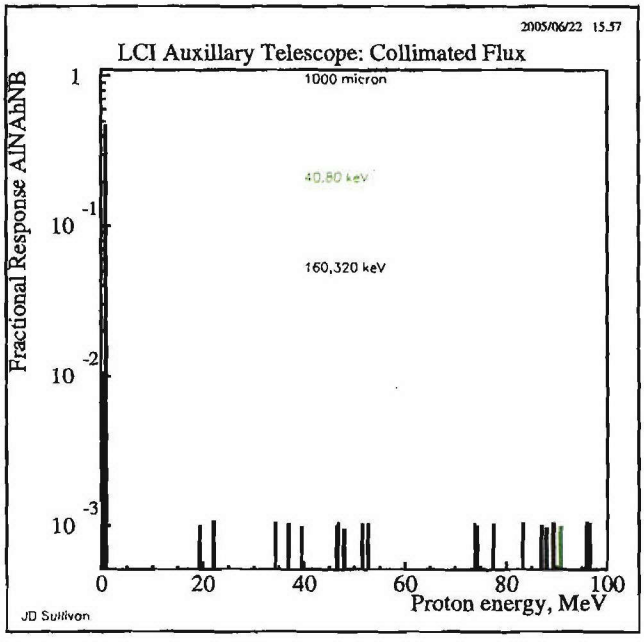


Figure 7: Probability that a proton of given energy will not trigger B while depositing either 40–80 keV or 160–320 keV in A

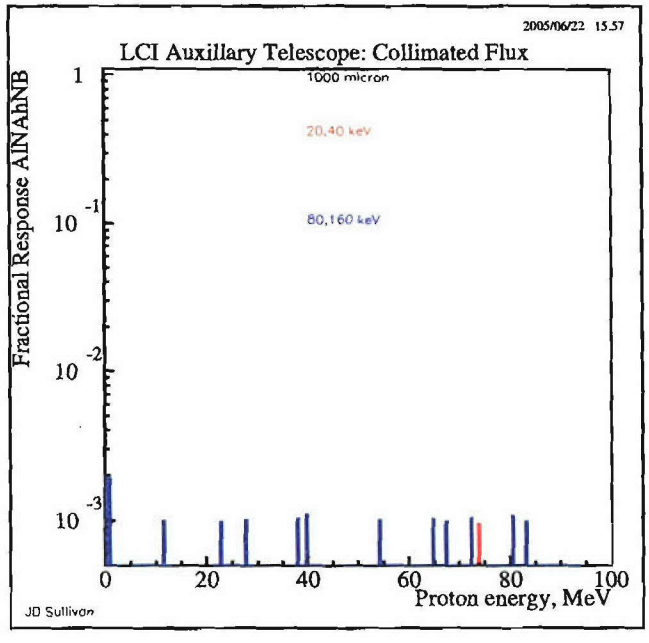


Figure 8: Probability that a proton of given energy will not trigger B while depositing either 20–40 keV or 80–160 keV in A

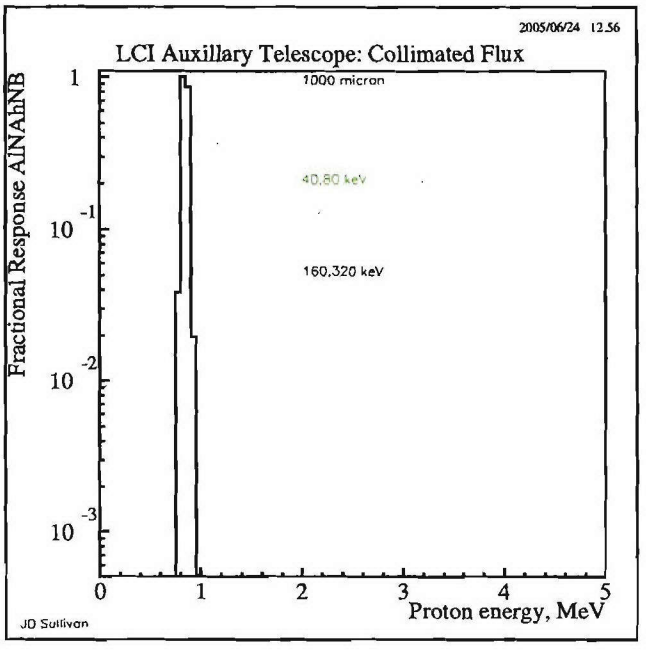


Figure 9: Probability that a proton of given energy will not trigger B while depositing either 40–80 keV or 160–320 keV in A

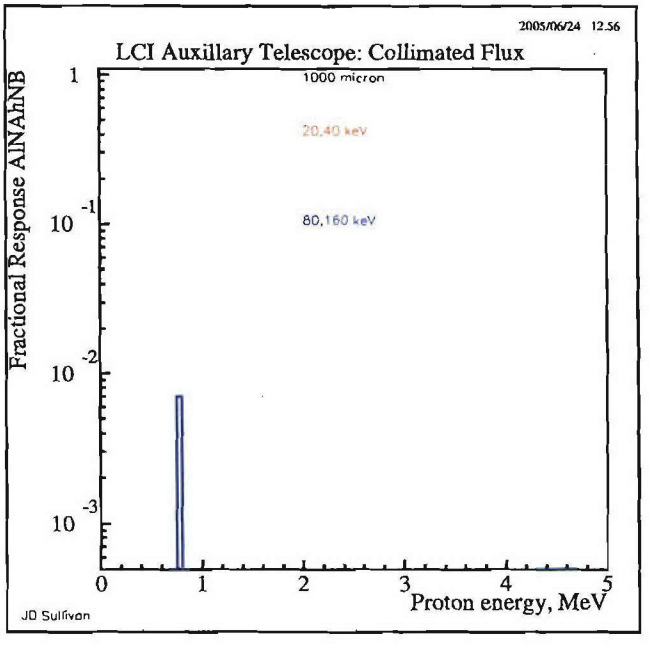


Figure 10: Probability that a proton of given energy will not trigger B while depositing either 20–40 keV or 80–160 keV in A

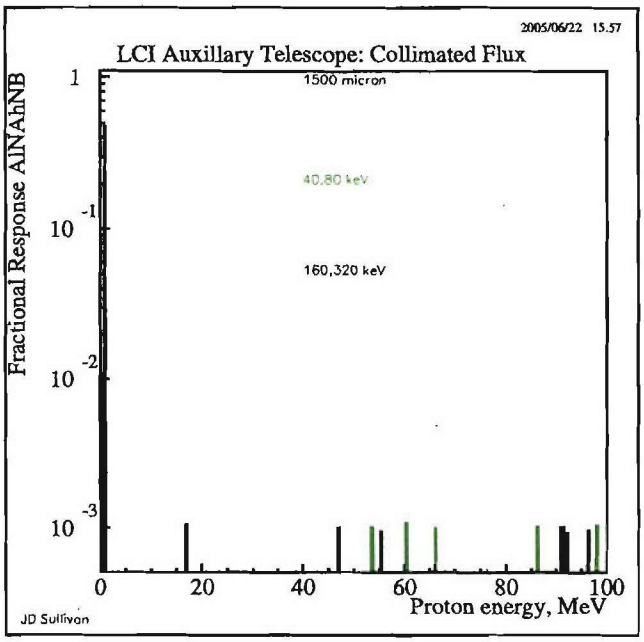


Figure 11: Probability that a proton of given energy will not trigger B while depositing either 40–80 keV or 160–320 keV in A

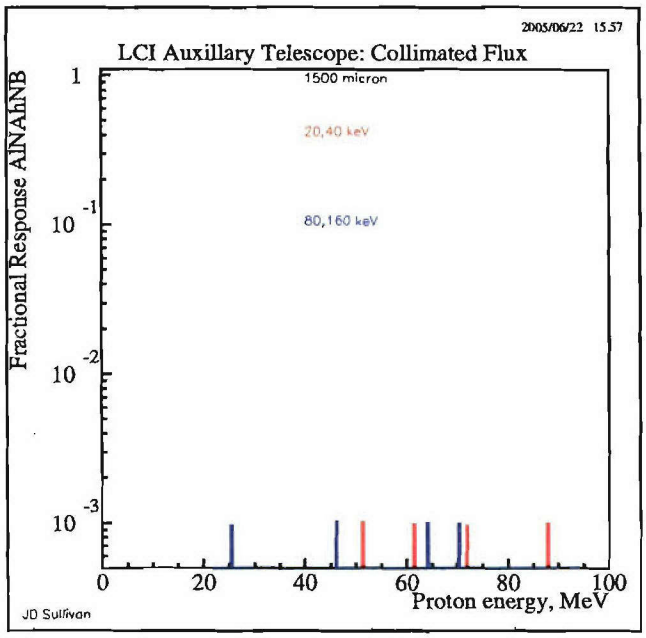


Figure 12: Probability that a proton of given energy will not trigger B while depositing either 20–40 keV or 80–160 keV in A

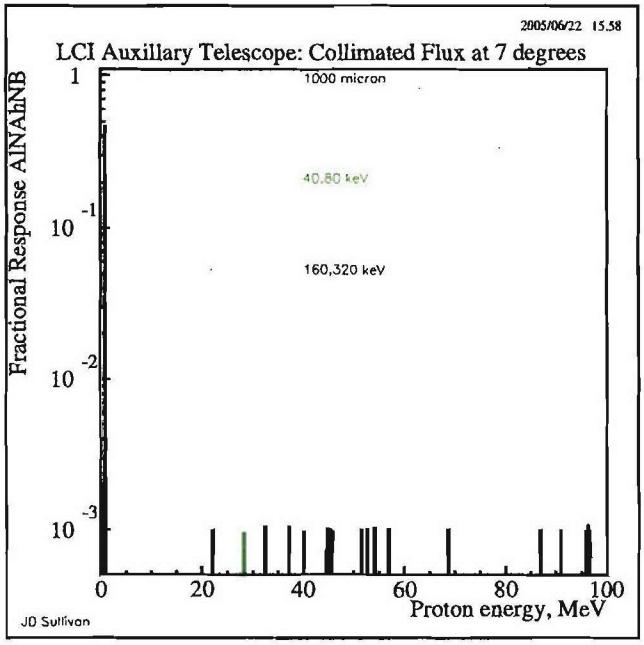


Figure 13: Probability that a proton of given energy will not trigger B while depositing either 40–80 keV or 160–320 keV in A

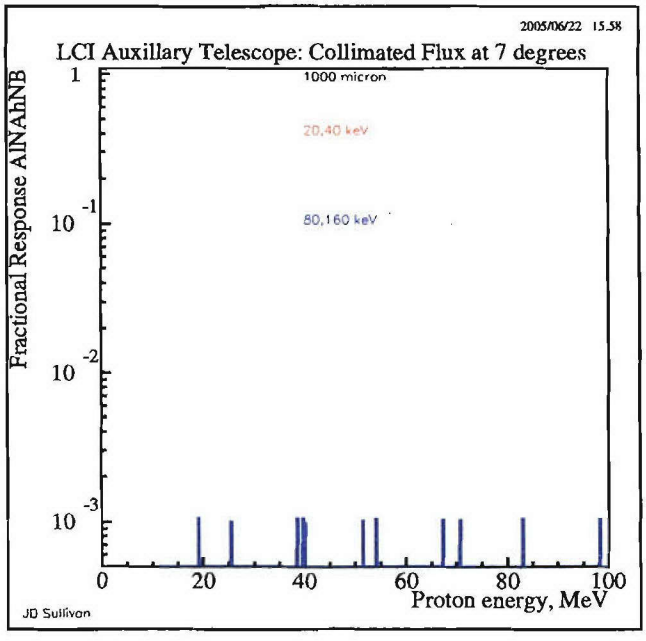


Figure 14: Probability that a proton of given energy will not trigger B while depositing either 20–40 keV or 80–160 keV in A

The difference between **1000** $\mu$m and **1500** $\mu$m detectors is most apparent in the scatter plot shown in Figure 15 where it is clear that a $\sim$ **320** keV discriminator level is problematic for the thinner detector. Figures 16 and 17 are the corresponding scatter plots for not triggering the B detector.

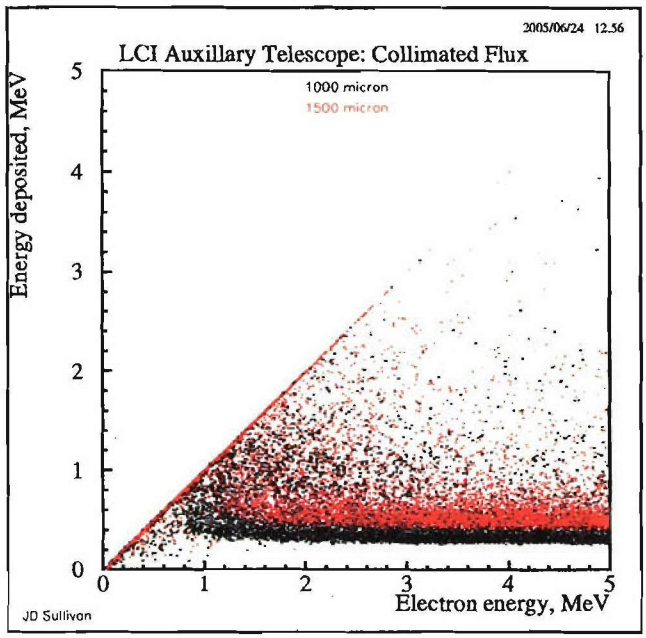


Figure 15: Scatter plot of the energy deposited in the A detector versus the primary electron energy.

## Background response to omnidirectional fluxes: plane shielding

The response of the HST detector to omnidirectional fluxes is computed by considering normal rays incident on the shielding (of the telescope) approximated by parallel planes of *Al* and *W*, sufficient to stop an **80** MeV proton, in front of a **1000** $\mu$m silicon detector, detector A, followed by a **1000** $\mu$m silicon detector for anti coincidence, detector B. The nominal thresholds are **40** keV of deposited energy. For the figures presented below, five hundred thousand events were generated using GEANT3 for each histogram.

**Remark:**

***Some possible shielding configurations are listed in Table 3 along with an estimate of the mass (excluding the base). While Al stops protons more ef-***

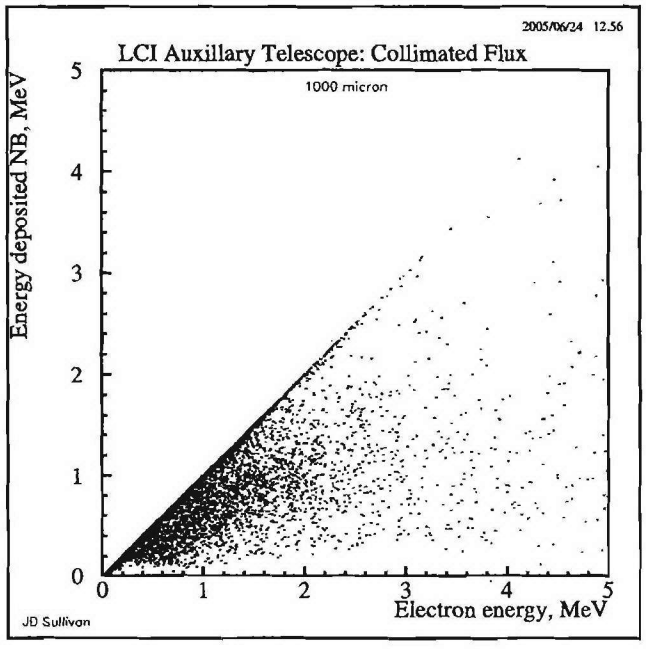


Figure 16: Scatter plot of the energy deposited in the A detector when the B detector is not triggered versus the primary electron energy.

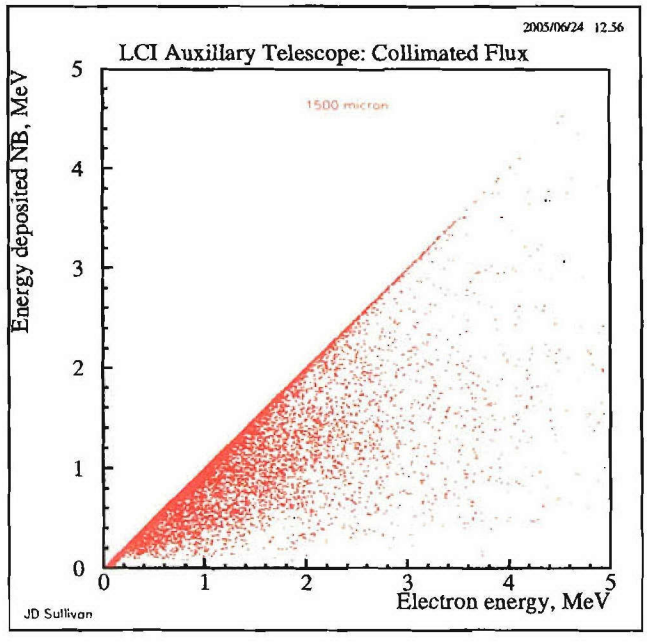


Figure 17: Scatter plot of the energy deposited in the A detector when the B detector is not triggered versus the primary electron energy.

***ficiently than $W$, the latter stops electrons/photons more efficiently. Hence the advantage of a graded (multi layered with different materials) shield. Note that while 5 $g/cm^2$ of $Al$ stops a 67.4 MeV proton, an 80 MeV proton only loses 42.2 MeV when traversing 5 $g/cm^2$ of $Al$. This effect, maximum $\frac{dE}{dx}$ near end of range, is usually represented by a* Bragg *curve.***

| $Al$, g/cm$^2$ | Residual energy, MeV | $W$, g/cm$^2$ | Shielding mass, kg |
|---|---|---|---|
| 7 | | 0 | 4.02 |
| 6.8 | 0.0 | 0 | 3.86 |
| 5 | 37.8 | 3.1 | 3.74 |
| 2 | 65.7 | 8 | 3.91 |
| 0 | 80 | 11.2 | 4.31 |

Table 3: Shielding sufficient to stop an **80** MeV proton assuming the $Al$ is on the outside; the rough mass of shielding assumes a **30** cm chimney and a **3.5** cm diameter bore (detector).

For **5** g/cm$^2$ of $Al$ followed by **3.1** g/cm$^2$ of $W$ shielding, the probability that an electron of given energy will be counted (background) in one of the desired energy bands is shown in Figures 18, 19, and 20. For the same geometry, the corresponding data for protons are shown in Figures 21, 22, and 23. The corresponding curves for **1500** $\mu$m A detector are given in Figures 24, 25, 26, 27, 28, and 29.

The probability of detection for protons that just penetrate the shielding is apparent as is the increasing likelihood that high energy electrons can masquerade as their low energy brethren.

For **2** g/cm$^2$ of $Al$ followed by **8** g/cm$^2$ of $W$ shielding, the probability that an electron of given energy will be counted (background) in one of the desired energy bands is shown in Figures 30, 31, and 32. For the same geometry, the corresponding data for protons are shown in Figures 33, 34, and 35.

For **7** g/cm$^2$ of $Al$ shielding, the probability that an electron of given energy will be counted (background) in one of the desired energy bands is shown in Figures 36, 37, and 38. For the same geometry, the corresponding data for protons are shown in Figures 39, 40, and 41.

For **11.2** g/cm$^2$ of $W$ shielding, the probability that an electron of given energy will be counted (background) in one of the desired energy bands is shown in Figures 42, 43, and 44. For the same geometry, the corresponding data for protons are shown in Figures 45, 46, and 47.

For **4** g/cm$^2$ of $W$ shielding outside **7.2** g/cm$^2$ of $Al$ shielding, the estimated shielding mass is **7.6** kg. The probability that an electron of given energy

will be counted (background) in one of the desired energy bands is shown in Figures 48, 49, and 50. For the same geometry, the corresponding data for protons are shown in Figures 51, 52, and 53.

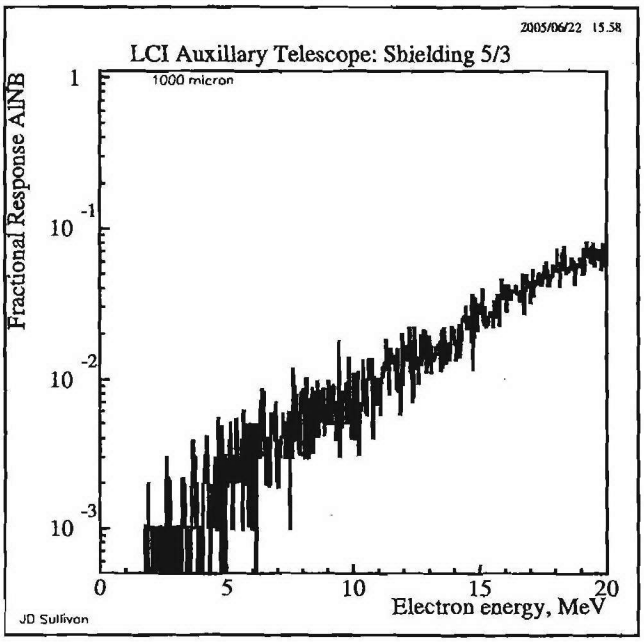


Figure 18: Probability that an electron of given energy will trigger A but not trigger B.

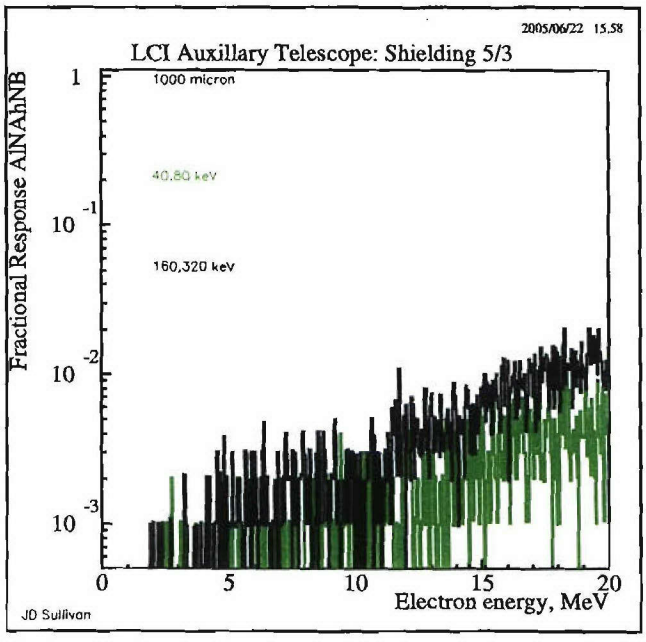


Figure 19: Probability that an electron of given energy will not trigger B while depositing either 40–80 keV or 160–320 keV in A

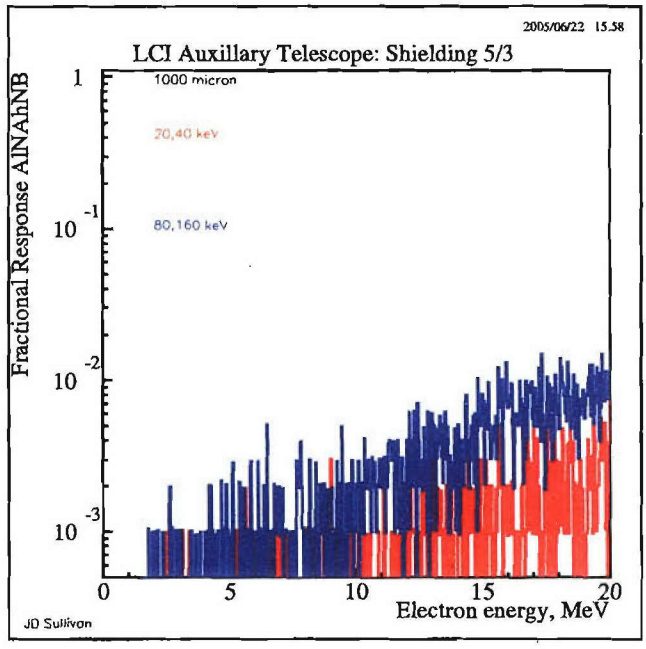


Figure 20: Probability that an electron of given energy will not trigger B while depositing either 20–40 keV or 80–160 keV in A

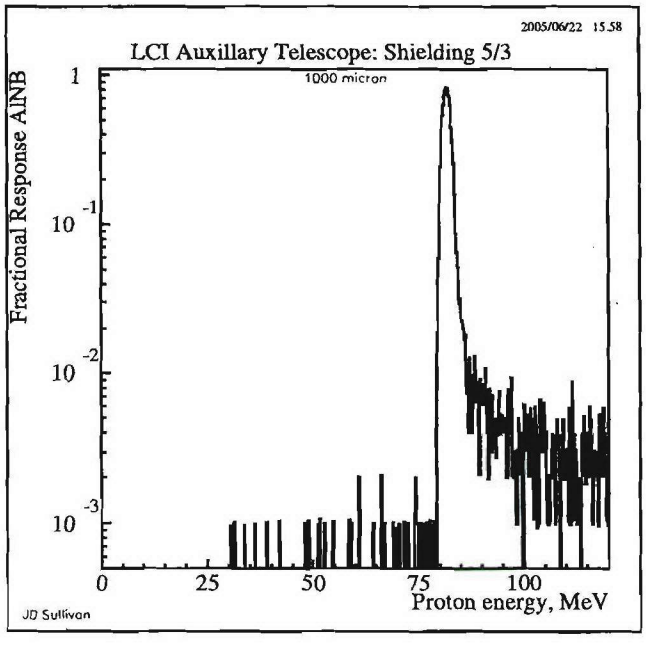


Figure 21: Probability that a proton of given energy will trigger A but not trigger B.

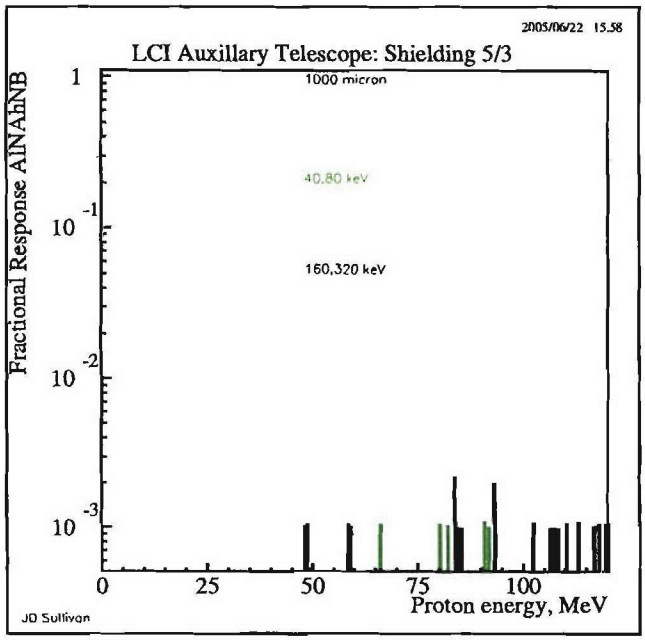


Figure 22: Probability that a proton of given energy will not trigger B while depositing either 40–80 keV or 160–320 keV in A

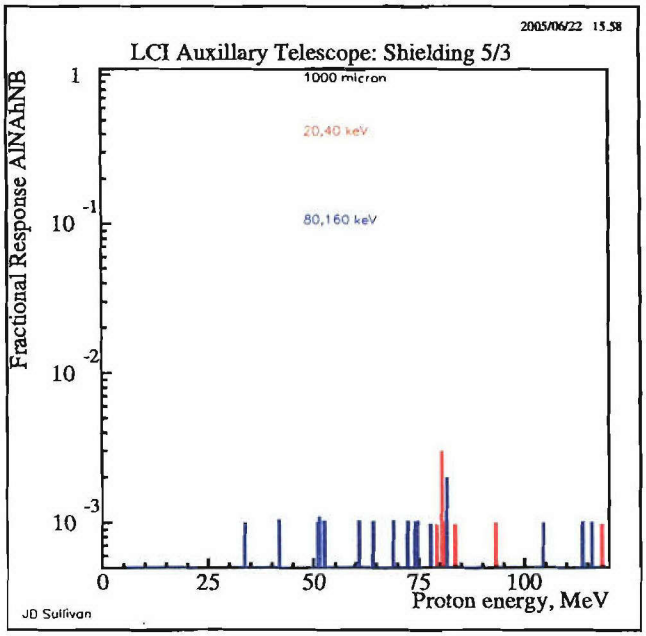


Figure 23: Probability that a proton of given energy will not trigger B while depositing either 20–40 keV or 80–160 keV in A

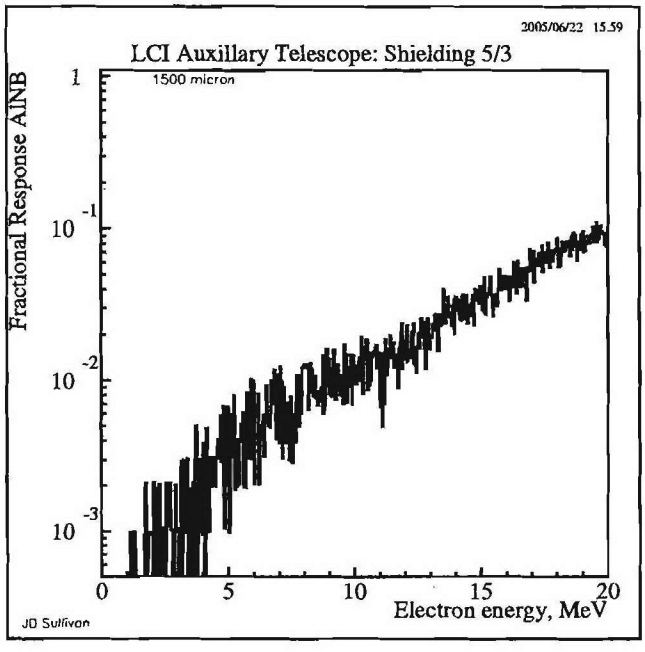


Figure 24: Probability that an electron of given energy will trigger A but not trigger B.

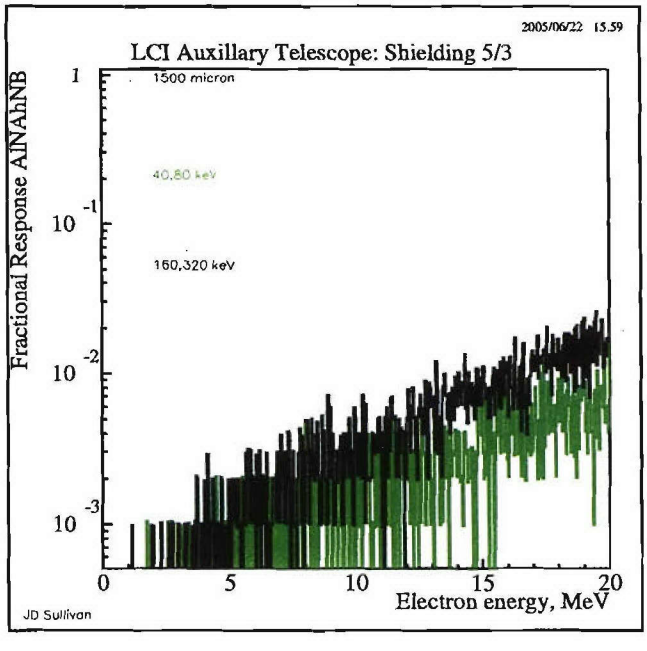


Figure 25: Probability that an electron of given energy will not trigger B while depositing either 40–80 keV or 160–320 keV in A

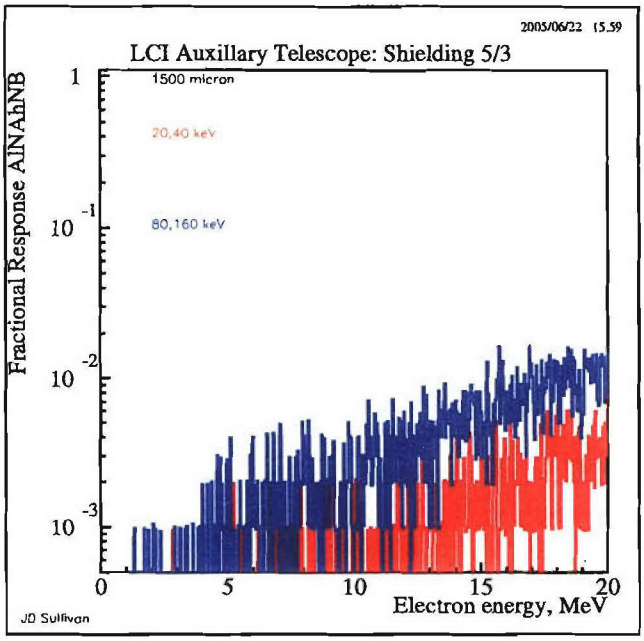


Figure 26: Probability that an electron of given energy will not trigger B while depositing either 20–40 keV or 80–160 keV in A

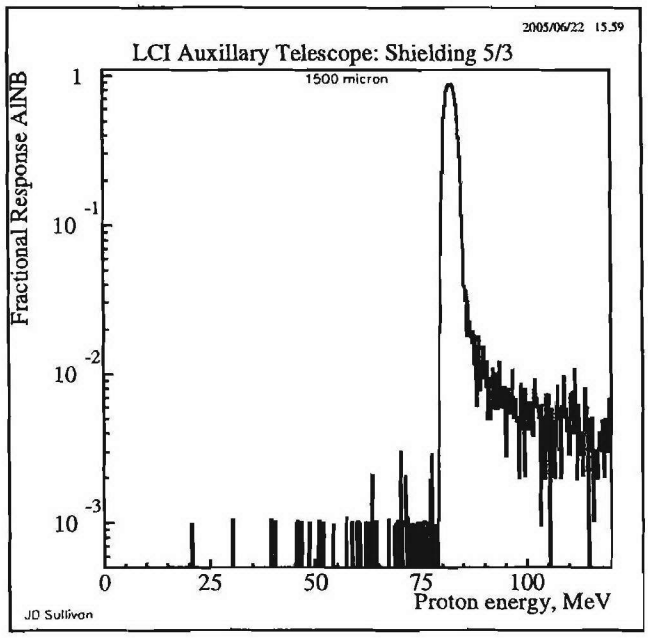


Figure 27: Probability that a proton of given energy will trigger A but not trigger B.

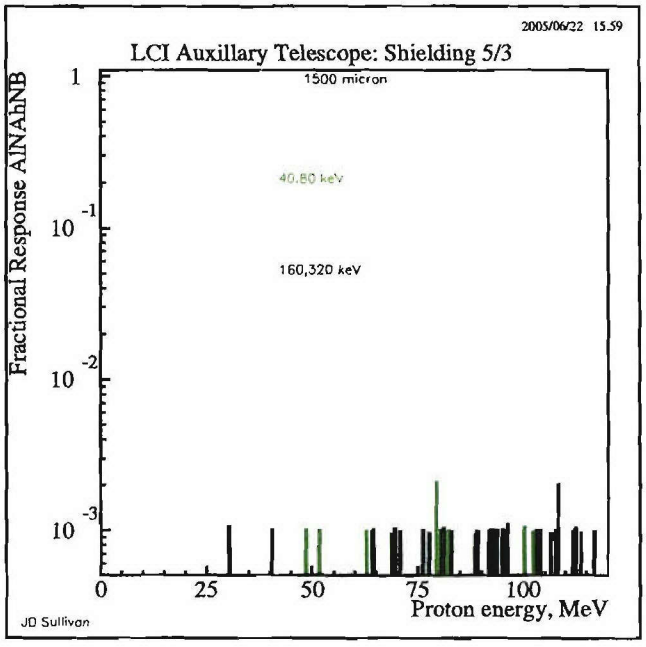


Figure 28: Probability that a proton of given energy will not trigger B while depositing either 40–80 keV or 160–320 keV in A

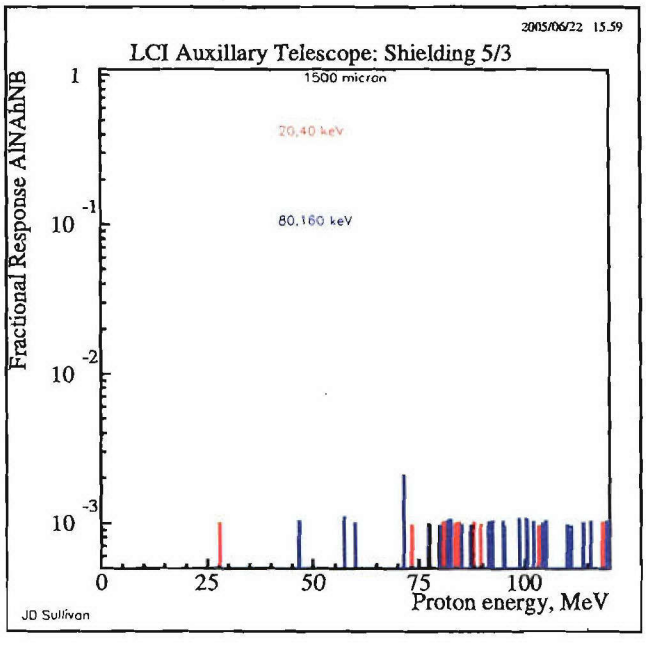


Figure 29: Probability that a proton of given energy will not trigger B while depositing either 20–40 keV or 80–160 keV in A

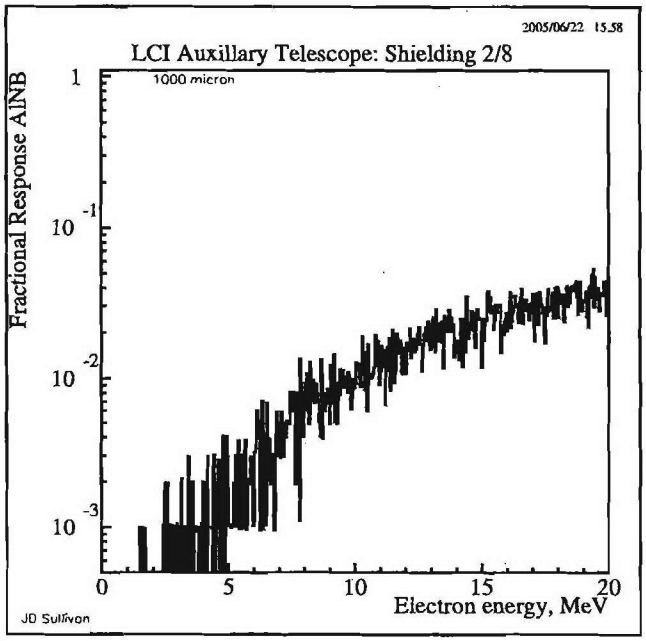


Figure 30: Probability that an electron of given energy will trigger A but not trigger B.

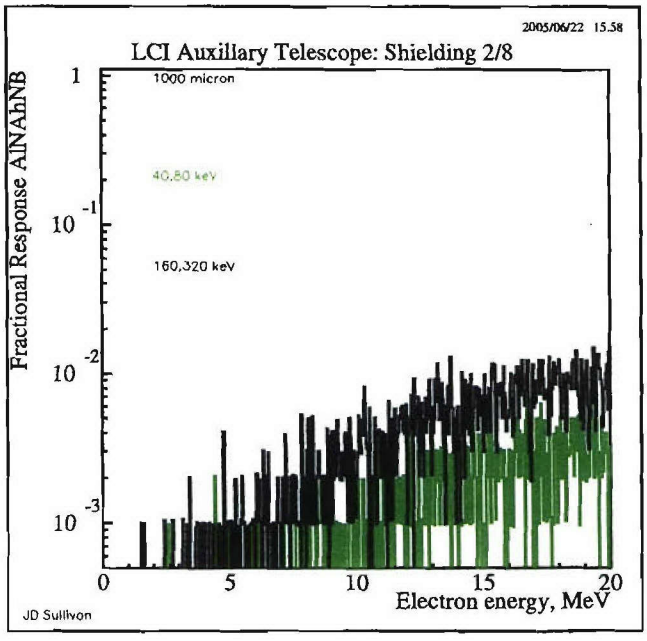


Figure 31: Probability that an electron of given energy will not trigger B while depositing either 40–80 keV or 160–320 keV in A

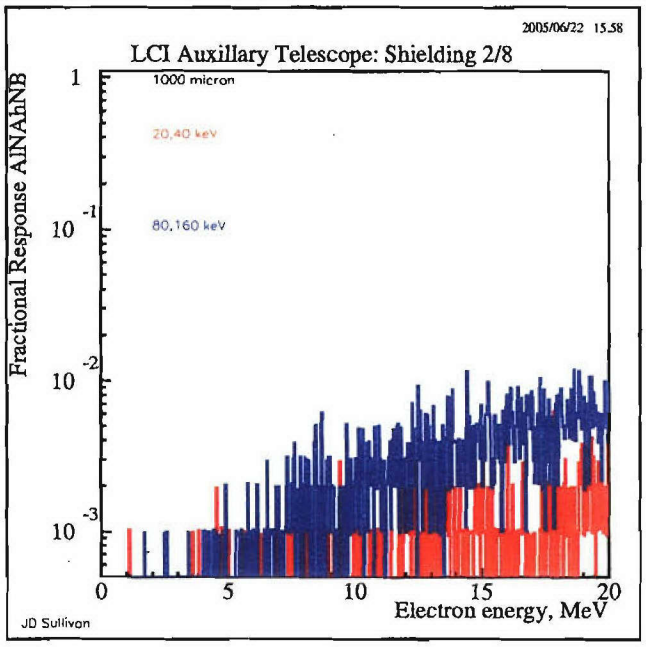


Figure 32: Probability that an electron of given energy will not trigger B while depositing either 20–40 keV or 80–160 keV in A

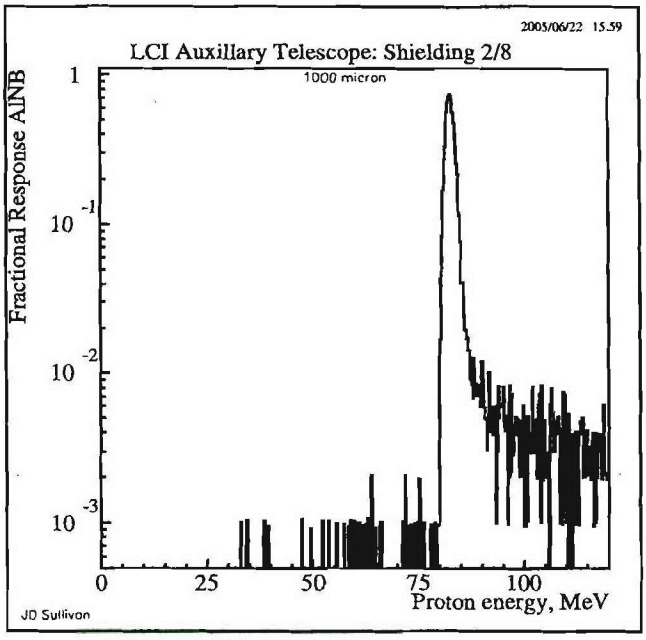


Figure 33: Probability that a proton of given energy will trigger A but not trigger B.

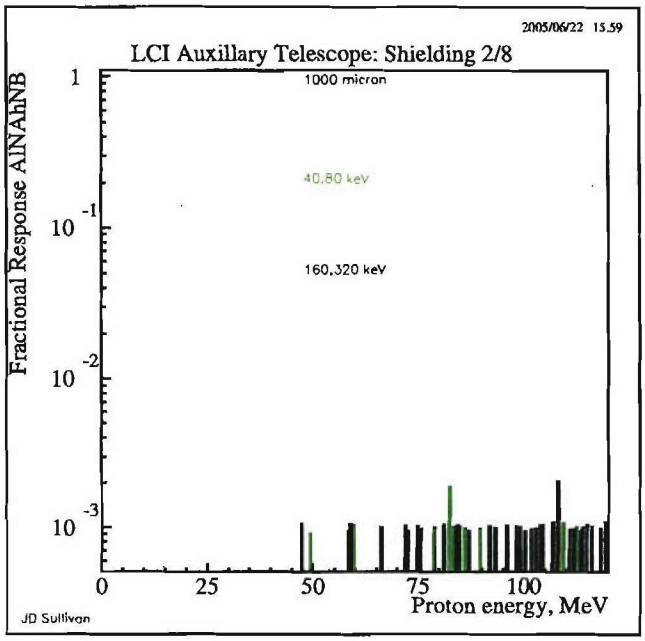


Figure 34: Probability that a proton of given energy will not trigger B while depositing either 40–80 keV or 160–320 keV in A

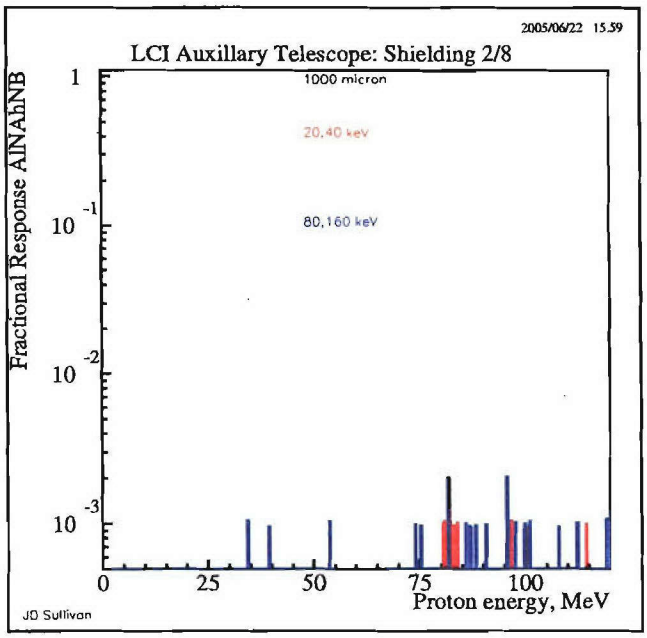


Figure 35: Probability that a proton of given energy will not trigger B while depositing either 20–40 keV or 80–160 keV in A

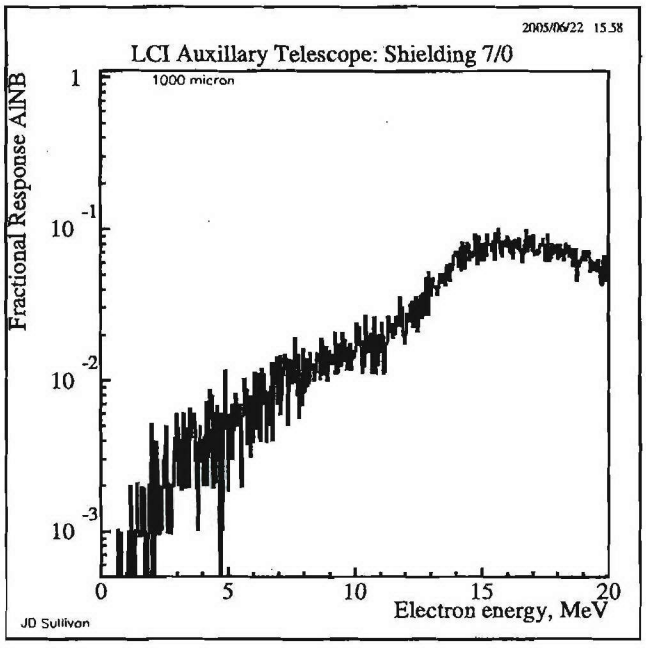


Figure 36: Probability that an electron of given energy will trigger A but not trigger B.

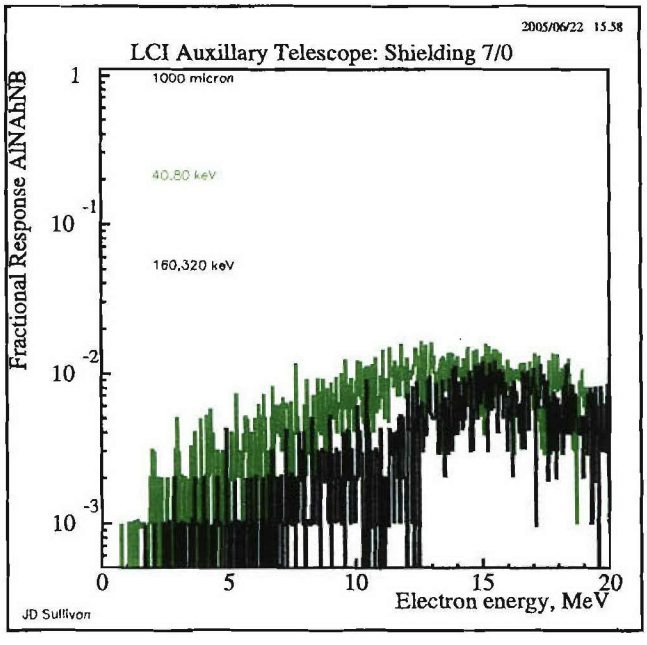


Figure 37: Probability that an electron of given energy will not trigger B while depositing either 40–80 keV or 160–320 keV in A

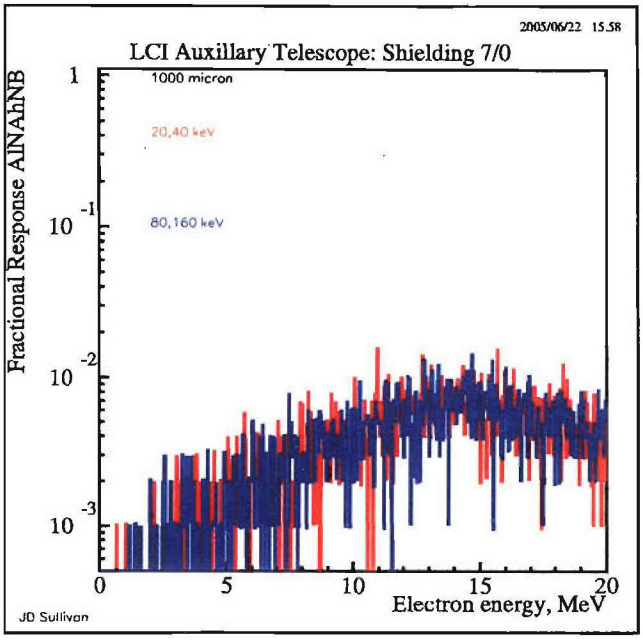


Figure 38: Probability that an electron of given energy will not trigger B while depositing either 20–40 keV or 80–160 keV in A

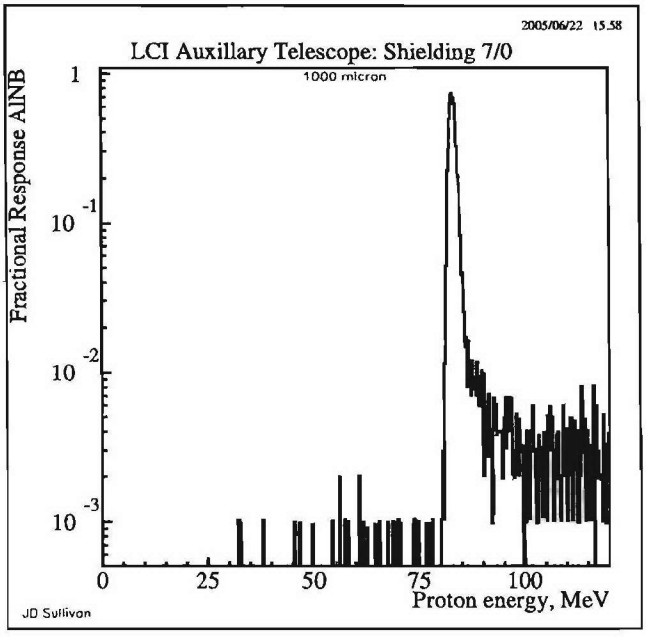


Figure 39: Probability that a proton of given energy will trigger A but not trigger B.

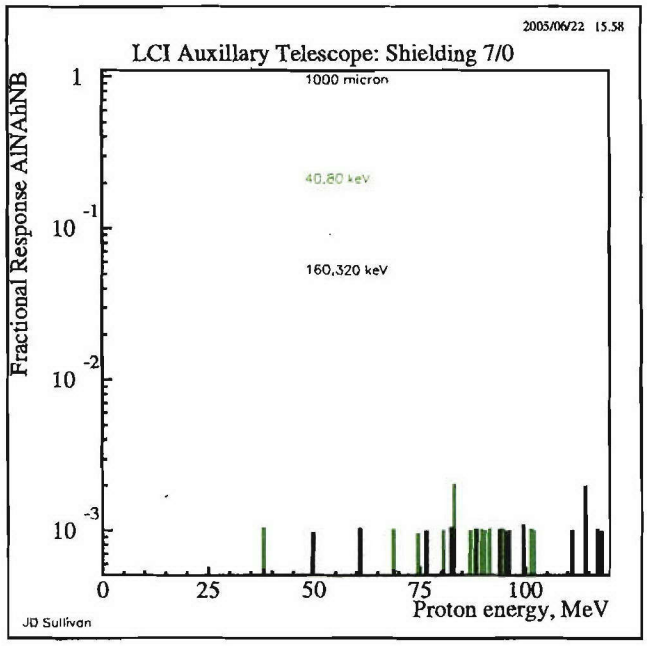


Figure 40: Probability that a proton of given energy will not trigger B while depositing either 40–80 keV or 160–320 keV in A

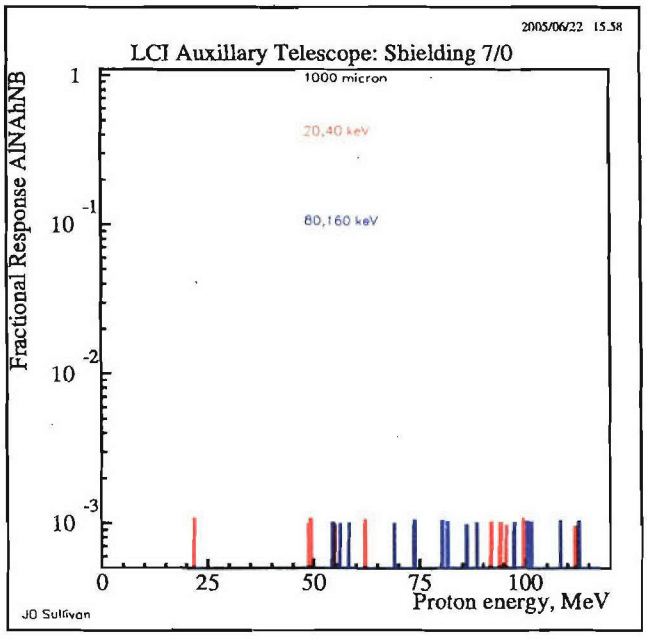


Figure 41: Probability that a proton of given energy will not trigger B while depositing either 20–40 keV or 80–160 keV in A

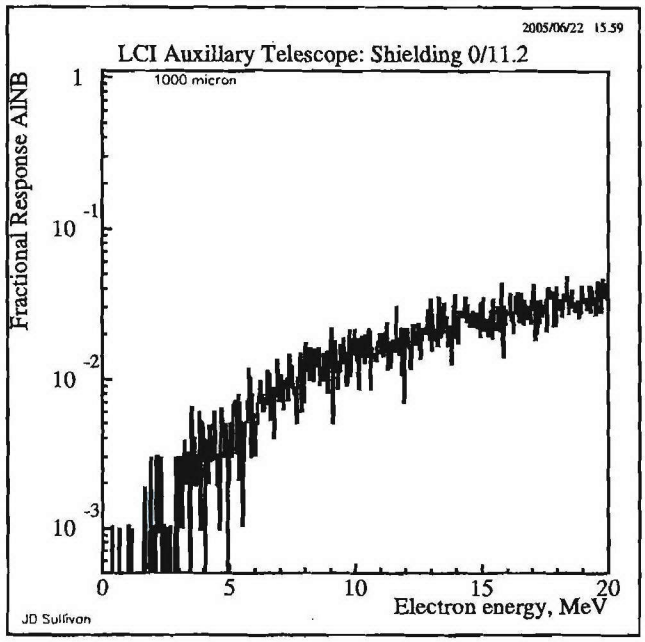


Figure 42: Probability that an electron of given energy will trigger A but not trigger B.

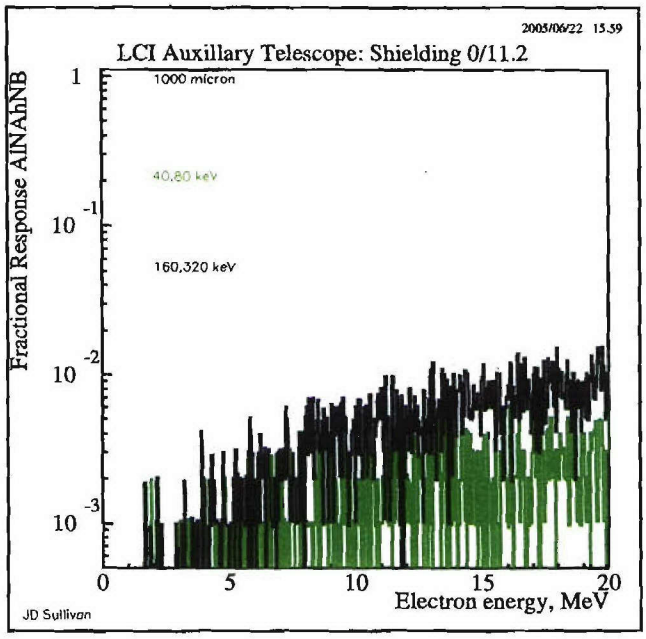


Figure 43: Probability that an electron of given energy will not trigger B while depositing either 40–80 keV or 160–320 keV in A

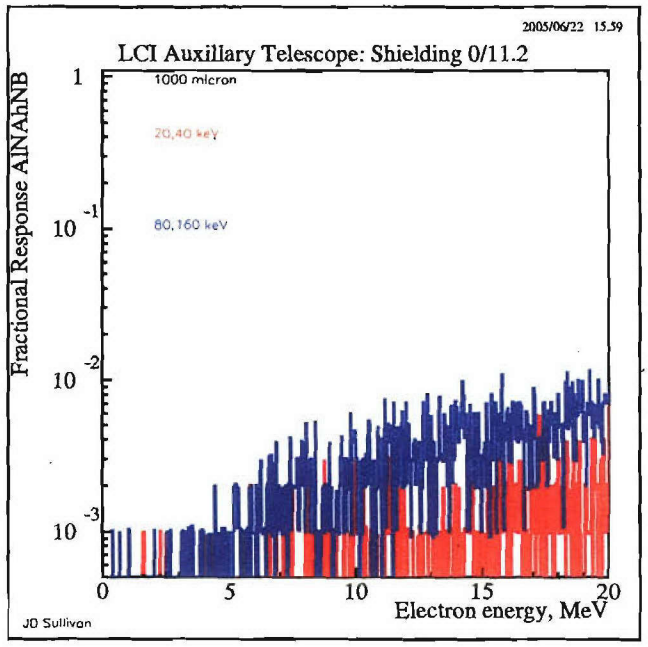


Figure 44: Probability that an electron of given energy will not trigger B while depositing either 20–40 keV or 80–160 keV in A

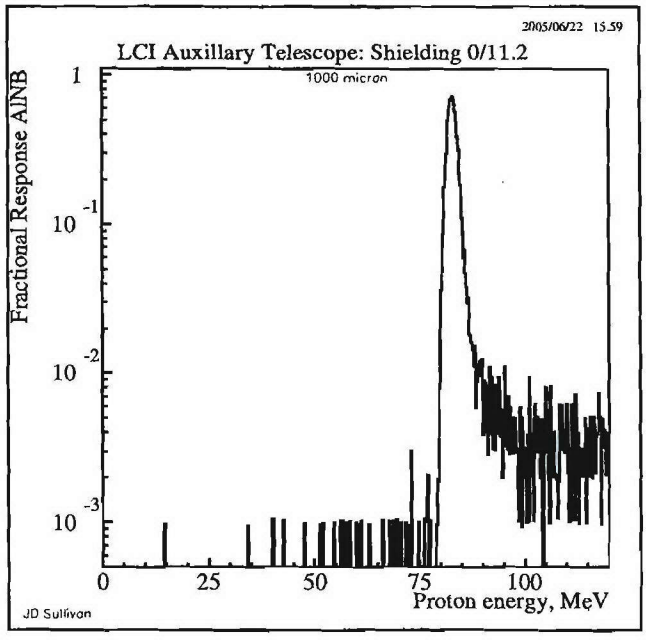


Figure 45: Probability that a proton of given energy will trigger A but not trigger B.

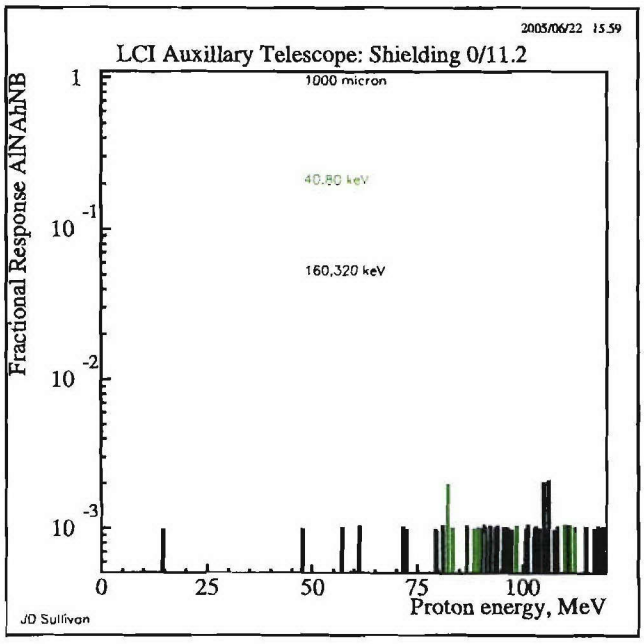


Figure 46: Probability that a proton of given energy will not trigger B while depositing either 40–80 keV or 160–320 keV in A

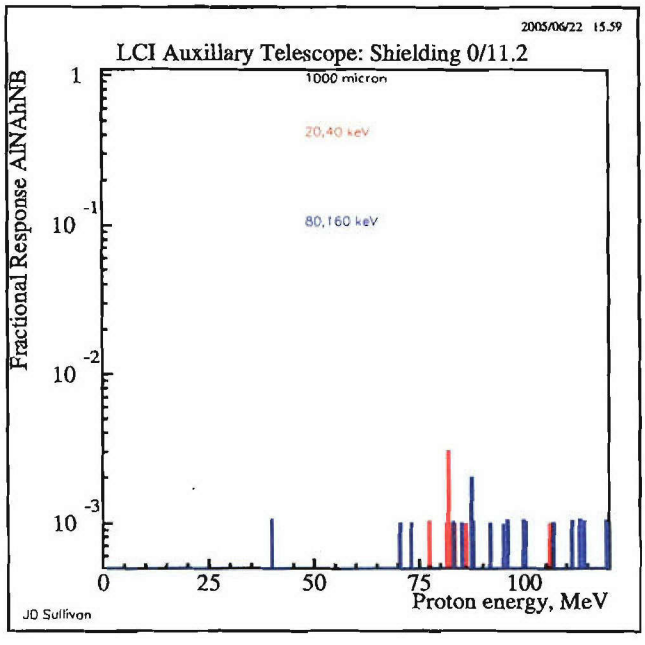


Figure 47: Probability that a proton of given energy will not trigger B while depositing either 20–40 keV or 80–160 keV in A

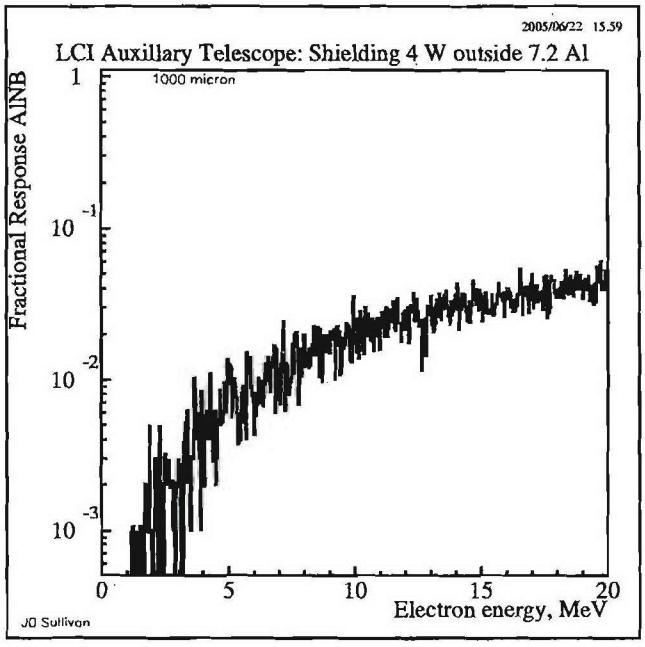


Figure 48: Probability that an electron of given energy will trigger A but not trigger B.

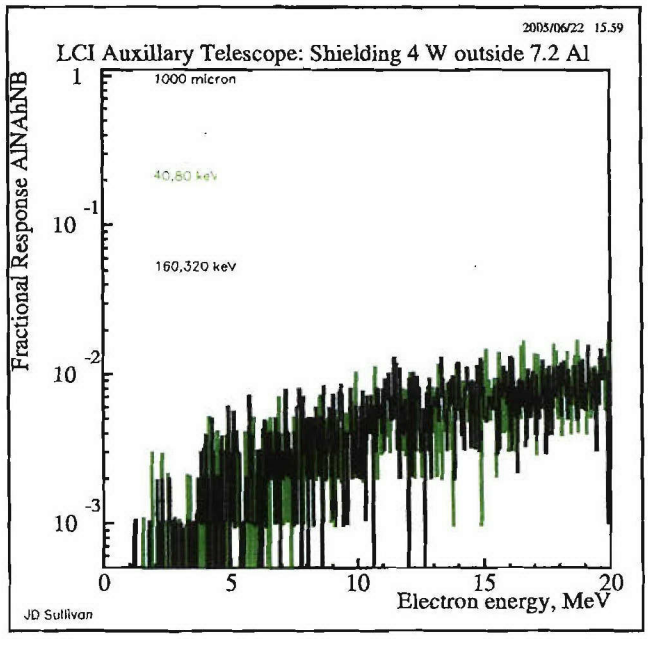


Figure 49: Probability that an electron of given energy will not trigger B while depositing either 40–80 keV or 160–320 keV in A

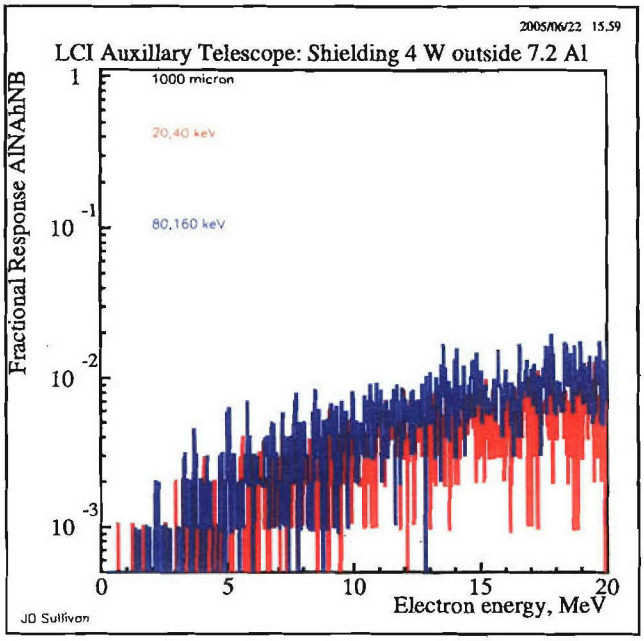


Figure 50: Probability that an electron of given energy will not trigger B while depositing either 20–40 keV or 80–160 keV in A

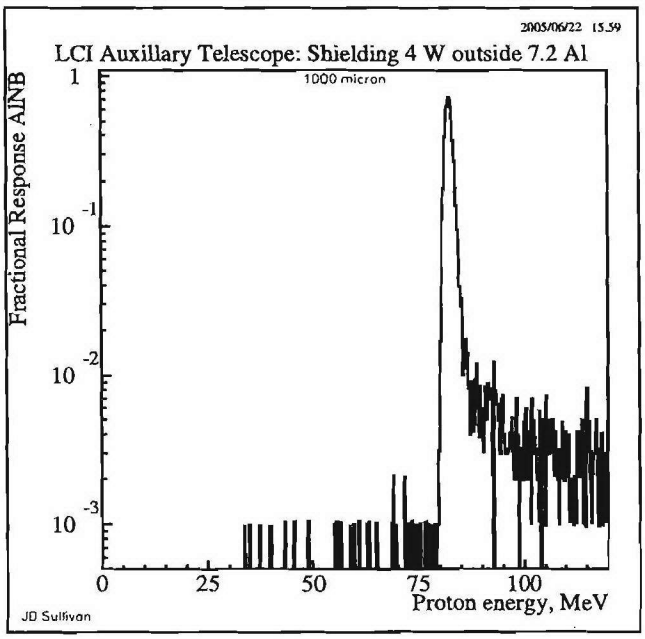


Figure 51: Probability that a proton of given energy will trigger A but not trigger B.

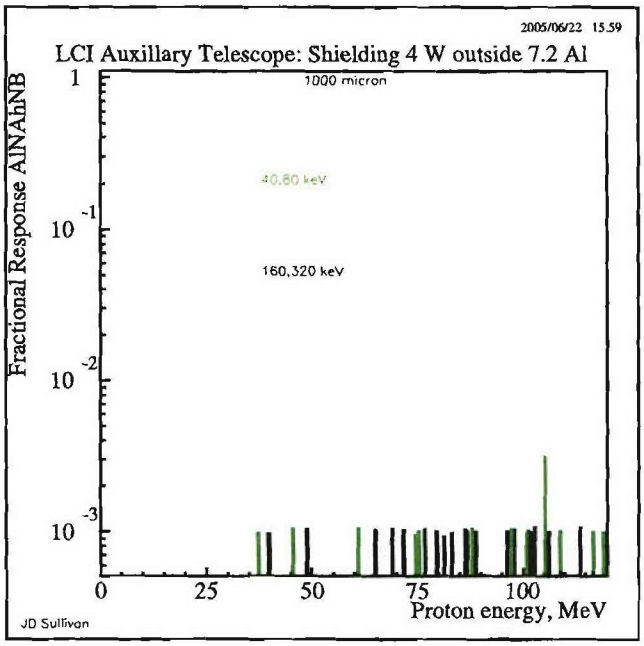


Figure 52: Probability that a proton of given energy will not trigger B while depositing either 40–80 keV or 160–320 keV in A

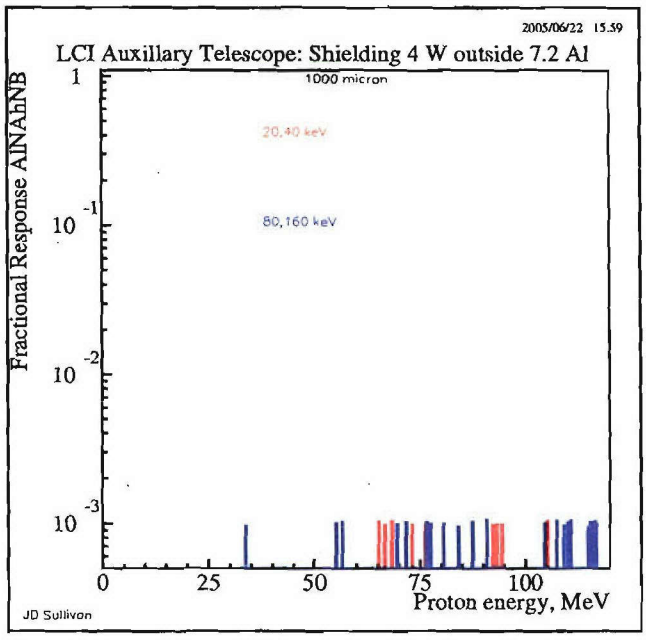


Figure 53: Probability that a proton of given energy will not trigger B while depositing either 20–40 keV or 80–160 keV in A

## Background response to omnidirectional fluxes: box shielding

The response of the HST detector to omnidirectional fluxes is computed by placing the active detectors, a **35** mm diameter **1000** $\mu$m silicon detector before a **40** mm diameter **1000** $\mu$m anti coincidence detector, in two closed shielding boxes, the outer of $Al$ and the inner of $W$, with sufficient thickness to stop an **80** MeV proton. The flux is assumed isotropic over the outer surface of the box. The nominal thresholds are **40** keV of deposited energy. For the figures presented below, two million events were generated for each histogram using GEANT3.

## LCI HST Response

What is the expected background counting rate of the LCI High Sensitivity Telescope if the shielding is sufficient to stop **80** MeV protons[1]? Clearly, there are two aspects to this question

1. what is the rate in the defined coincidence ranges? this is essentially the background rate
2. at what rate are the detectors counting? this can affect pileup and was the basis for the **80** MeV threshold.

Answers to these questions are given in Tables 1 and 2 where the expected counting rates from omni-directional protons and electrons are tabulated. These background rates are worst case as $\boldsymbol{B/B0 = 1}$ is assumed.

Table 1: LCI HST: anticipated (peak) background counting rates, cts/s, due to protons ($\leq$ **400** MeV), AP8MAX $\boldsymbol{B/B0 = 1}$, as a function of L-value. Approximately twenty-five million events were used in this analysis. The background rates are rounded to the nearest count.

| | L-value | | | | | | | |
|---|---|---|---|---|---|---|---|---|
| Coincidence ranges, keV | 1.8 | 2.0 | 2.2 | 2.4 | 2.6 | 2.8 | 3.0 | 3.2 |
| $\boldsymbol{20 < A}$ | 43059 | 8911 | 1701 | 272 | 39 | 10 | 5 | 2 |
| $\boldsymbol{40 < A, B < 40}$ | 11457 | 2373 | 454 | 73 | 11 | 3 | 1 | 1 |
| $\boldsymbol{20 < A < 40, B < 40}$ | 18 | 4 | 1 | 0 | 0 | 0 | 0 | 0 |
| $\boldsymbol{40 < A < 80, B < 40}$ | 88 | 22 | 6 | 1 | 0 | 0 | 0 | 0 |
| $\boldsymbol{80 < A < 160, B < 40}$ | 250 | 44 | 7 | 1 | 0 | 0 | 0 | 0 |
| $\boldsymbol{160 < A < 320, B < 40}$ | 978 | 160 | 18 | 3 | 1 | 0 | 0 | 0 |

For example at $\boldsymbol{L = 2}$, the expected net background in the $\boldsymbol{20 < E < 160}$ keV band from the three proton, Table 1, and three electron, Table 2, coincidence ranges is $\boldsymbol{(4 + 22 + 44) + (3 + 7 + 16) = 96}$ cts/s with a sigma of $\boldsymbol{\pm 10}$.

Normally, two signals differing by $\boldsymbol{1.5\,\sigma}$ are considered resolvable. Thus at $\boldsymbol{L = 2}$ where the background is $\boldsymbol{96 \pm 10}$ cts/s, a signal of $\sim$ **15** cts/s is detectable. At $\boldsymbol{L = 2.8}$, the net background becomes $\boldsymbol{431 \pm 21}$ cts/s so that a signal of $\sim$ **30** cts/s is detectable. Finally at $\boldsymbol{L = 3}$,the background becomes $\boldsymbol{958 \pm 31}$ cts/s so that a signal of $\sim$ **45** cts/s is detectable.

[1] **80** MeV was chosen to keep the peak detector rates below $\sim$ **10 000** cts/s (cf. JDS WM#8)

Table 2: LCI HST: anticipated (peak) background counting rates, cts/s, due to electrons ($\leq$ 7 MeV), AE8MAX $B/B0 = 1$, as a function of L-value. Approximately twenty-five million events were used in this analysis. The background rates are rounded to the nearest count.

| | L-value | | | | | | | |
|---|---|---|---|---|---|---|---|---|
| Coincidence ranges, keV | 1.8 | 2.0 | 2.2 | 2.4 | 2.6 | 2.8 | 3.0 | 3.2 |
| $20 < A$ | 245 | 42 | 18 | 25 | 293 | 896 | 2017 | 3108 |
| $40 < A, B < 40$ | 160 | 29 | 13 | 18 | 185 | 570 | 1277 | 1962 |
| $20 < A < 40, B < 40$ | 14 | 3 | 1 | 2 | 13 | 42 | 93 | 140 |
| $40 < A < 80, B < 40$ | 40 | 7 | 3 | 5 | 46 | 144 | 327 | 505 |
| $80 < A < 160, B < 40$ | 78 | 16 | 7 | 10 | 81 | 245 | 533 | 805 |
| $160 < A < 320, B < 40$ | 54 | 10 | 4 | 6 | 63 | 190 | 419 | 642 |

Outside $L = 2$, the A detector will have a (peak) background rate $<$ **10 000** cts/s while inside the rate approaches **50 000** cts/s. The B detector rate will be some **30%** higher and the AB coincidence rate $<$ **50%** of the A singles rate. These rates are within the time resolution, **3**$\mu$s, of the electronics so that mis-identification and pile up should be not be important.

## Details of modeling and simulation

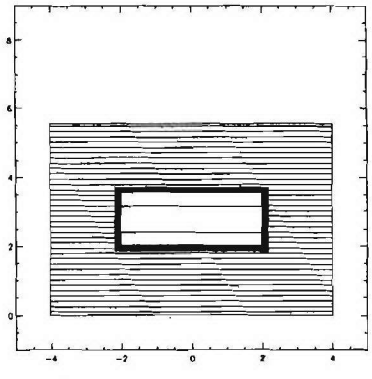

Figure 1: Sketch of the shield box used for radiation modeling in GEANT3. This cylindrically-symmetric graded-shield box comprises an outer shell of **5** g/cm$^2$ of aluminum, to stop protons, and an inner shell of **3.1** g/cm$^2$ of tungsten, to convert photons surrounding a two element detector stack with a **1500** $\mu$m-thick, **3.5** cm-diameter Si-detector and a **1000** $\mu$m-thick, **4** cm-diameter Si-detector. The box is **8.06** cm in diameter and **5.56** cm in height.

For radiation response, the HST may be modeled as a cylindrical box comprising **5** g/cm$^2$ of aluminum, to stop protons, and **3.1** g/cm$^2$ of tungsten, to convert photons, surrounding a two element detector stack with a **1500** $\mu$m-thick, **3.5** cm-diameter Si-detector, detector A, and a **1000** $\mu$m-thick, **4** cm-diameter Si-detector, detector B as shown in Figure 1. Also, for modeling, a guard ring, detector C, surrounds detector A, presumably on the same wafer; this annular detector has an inner diameter of **3.51** cm and an outer diameter of **4** cm.

The omni-directional geometrical factor[2] for the box is $\approx$ **763** cm$^2$ $\cdot$ sr and that for detector A $\approx$ **60.8** cm$^2$ $\cdot$ sr; thus the geometrical factor for detector A is about **7.9%** that of the box.

The response is computed using a Monte Carlo approach.[3] An isotropic angular distribution uniform in energy is incident on the outer surface of the box. Each ray is propagated and its history, e.g., energy deposited in detector A, recorded — this is done using GEANT3. Then the results are tallied and normalized subject to certain logic constraints and displayed — using PAW. This gives the effective geometrical factor as a function of energy. Finally, the expected counting rate is computed by folding in an assumed energy spectrum, e.g, AE8MAX.

### Proton response

The probability that a proton of given energy will trigger detector A is shown in Figure 2 based on five million Beroulli trials. Several features are immediately apparent:

- the **80** MeV cutoff
- the flattening at higher energies with a limit of $\sim$ **0.08** corresponding to slightly less than the omni-directional ratio, as expected.

The probability that a proton of given energy will trigger detector A, $>$ **40** keV, and not trigger detector B, $<$ **40** keV, is shown in Figure 3 based on five million Bernoulli trials. The probability for detecting protons which

[2] $G = \pi A$

[3] See *Monte Carlo Simulation*, J.D.Sullivan, Department of Physics, Boston University, 1996, 38 pages, privately distributed.

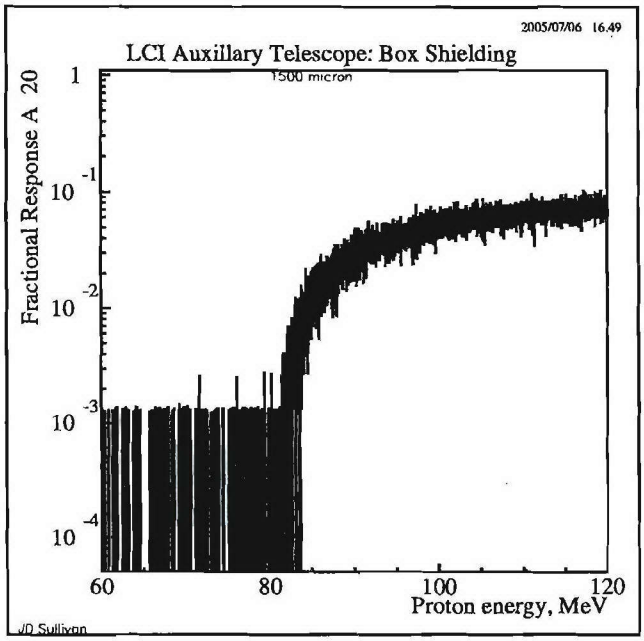


Figure 2: Probability that a proton of given energy will deposit $>$ **20** keV in A

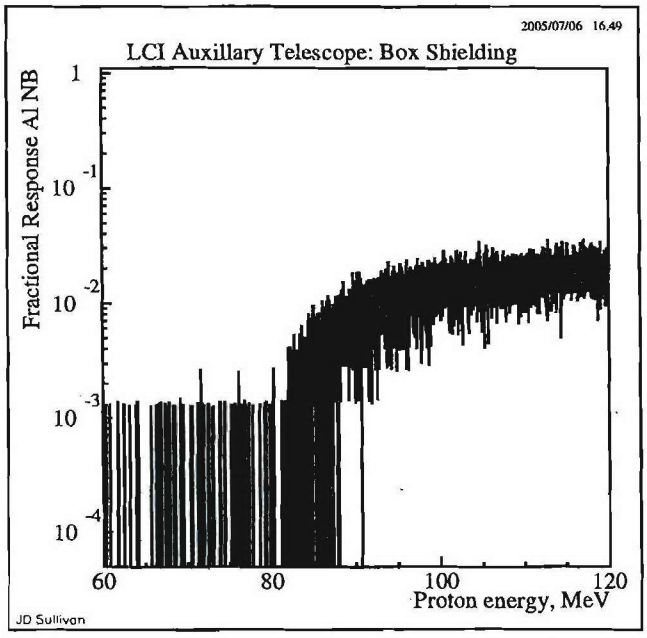


Figure 3: Probability that a proton of given energy will trigger A but not trigger B.

just penetrate the shielding is apparent in the sharp turn on above **80** MeV as is the reduction because particles from the back trigger B. Also there is a suggestion that the response, although finite, decreases as the energy decreases below the **80** MeV cutoff; this response is due to neutron and gamma production from nuclear interactions at $\sim$ 1% level.

The question that remains is, what is the differential response in detector A. This is shown in Figures 4 and 5. Finally, these results are given, with greater statistical accuracy, as effective geometrical factor as a function of incident energy in Figures 6, 7, and 8.

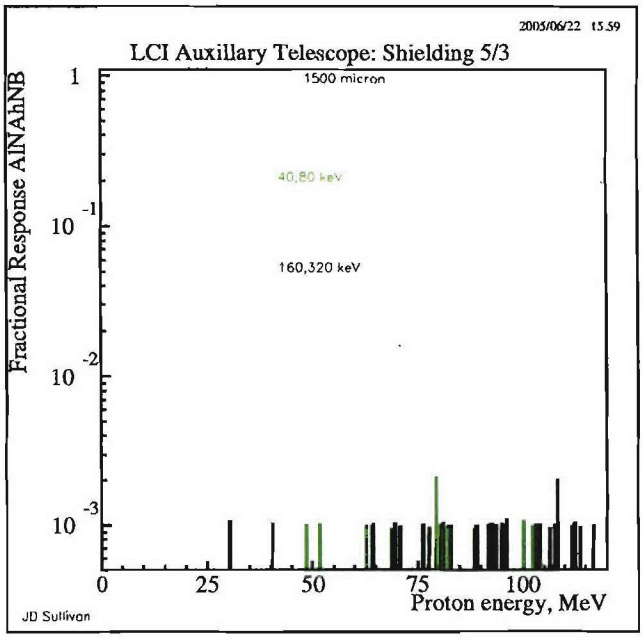


Figure 4: Probability that a proton of given energy will not trigger B while depositing either 40–80 keV or 160–320 keV in A

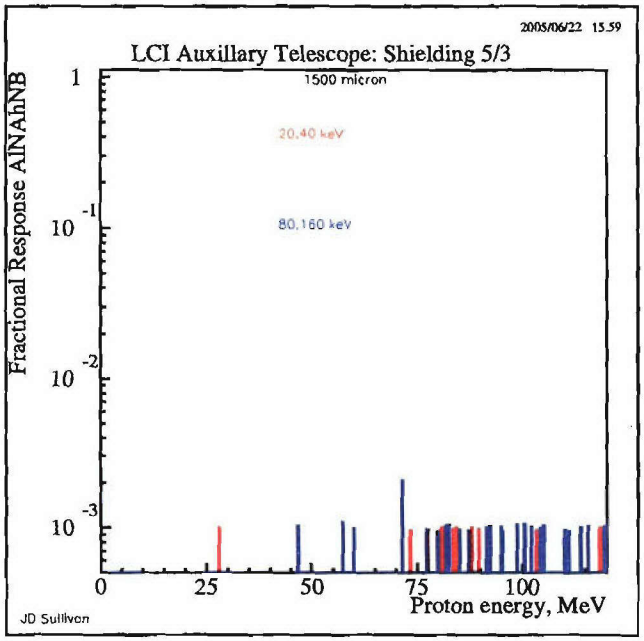


Figure 5: Probability that a proton of given energy will not trigger B while depositing either 20–40 keV or 80–160 keV in A

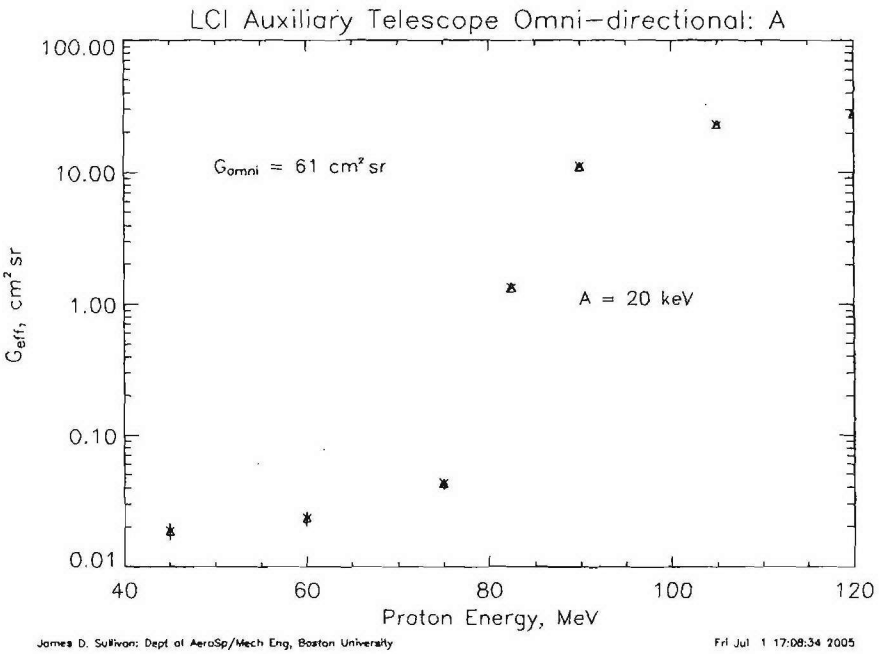


Figure 6: The effective geometrical factor of omni-directional protons penetrating a closed cylindrical box comprising **5** g/cm$^2$ of AL followed by **3.1** g/cm$^2$ of W and depositing **20** keV in detector A

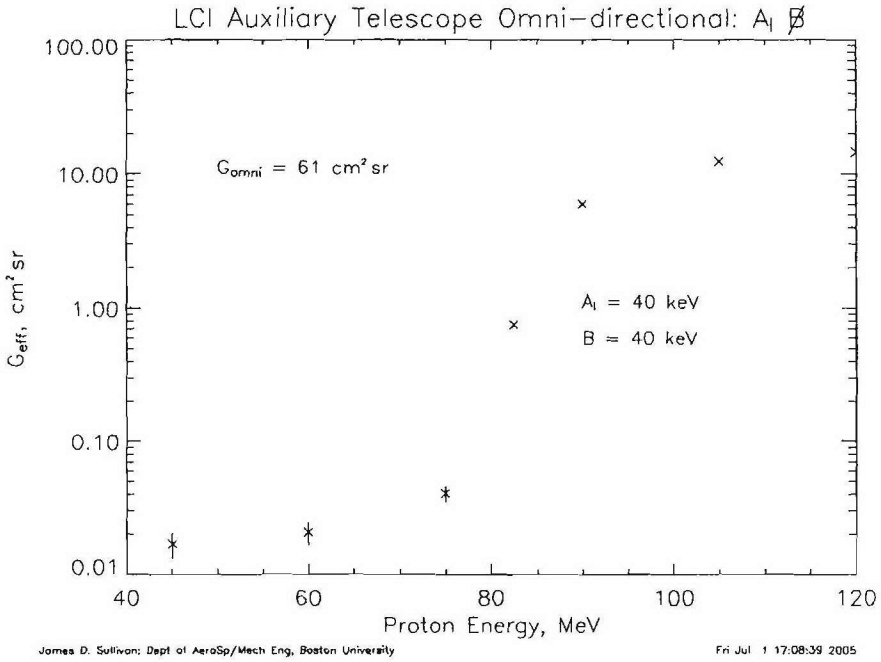


Figure 7: The effective geometrical factor of omni-directional protons penetrating a closed cylindrical box comprising **5** g/cm$^2$ of AL followed by **3.1** g/cm$^2$ of W and depositing **40** keV in detector A but less than **40** keV in detector B

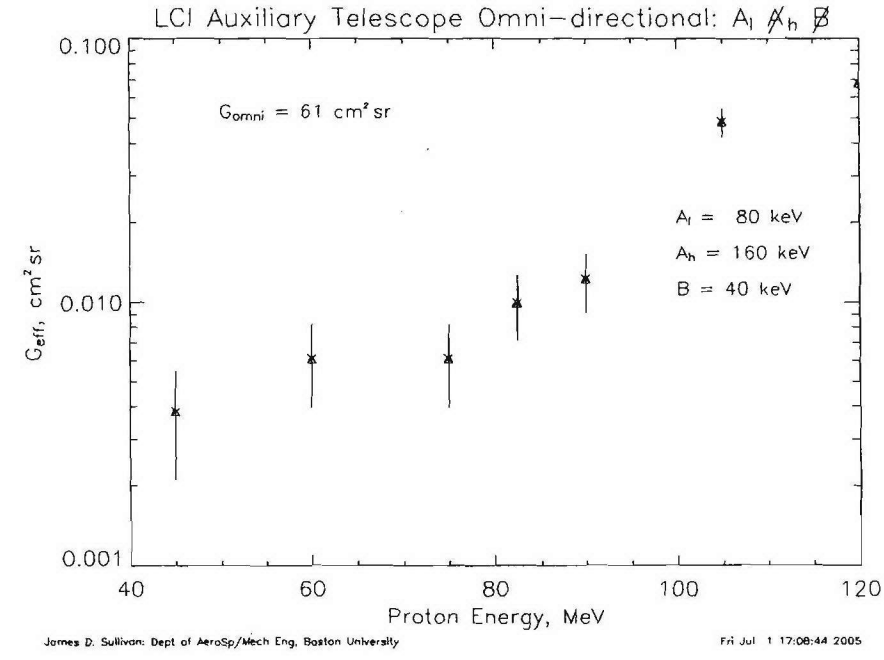


Figure 8: The effective geometrical factor of omni-directional protons penetrating a closed cylindrical box comprising **5** g/cm$^2$ of AL followed by **3.1** g/cm$^2$ of W and depositing between **80** keV and **160** keV in detector A but less than **40** keV in detector B

### Electron response

The probability that an electron of given energy will trigger detector A is shown in Figure 9 based on five million Bernoulli trials. It is apparent that

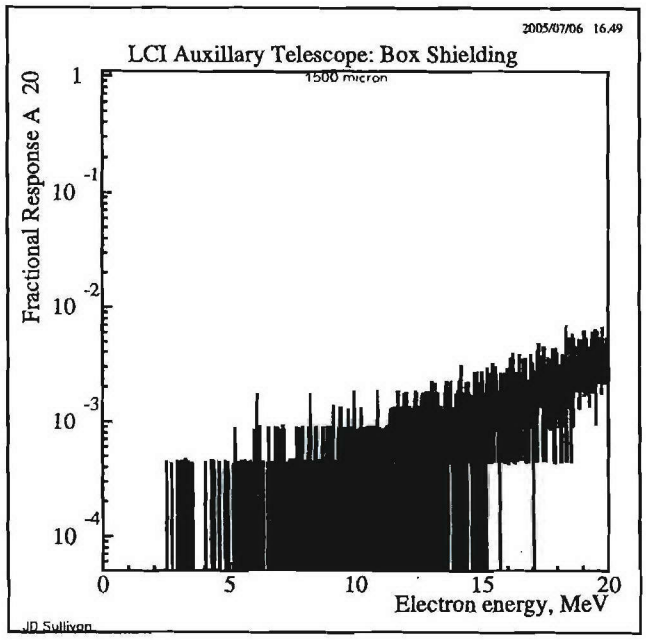


Figure 9: Probability that an electron of given energy will deposit $>$ **20** keV in A

electrons behave differently from protons; a **5** MeV electron has a $\gamma \approx$ **10** so that instead of a range there is an absorption length. The probability that an electron of given energy will trigger detector A, $>$ **40** keV, and not trigger detector B, $<$ **40** keV, is shown in Figure 10 based on five million Bernoulli trials.

The reduction in probability for detecting electrons because particles from the back trigger B is apparent. Also, it should be noted that the response, although finite, decreases sharply as $\gamma$ decreases below two — pair production is no longer kinematically possible.

The question that remains is, what is the differential response in detector A. This is shown in Figures 11 and 12. Finally, these results are given, with greater statistical accuracy, as effective geometrical as a function of incident energy Figures 13, 14, and 15.

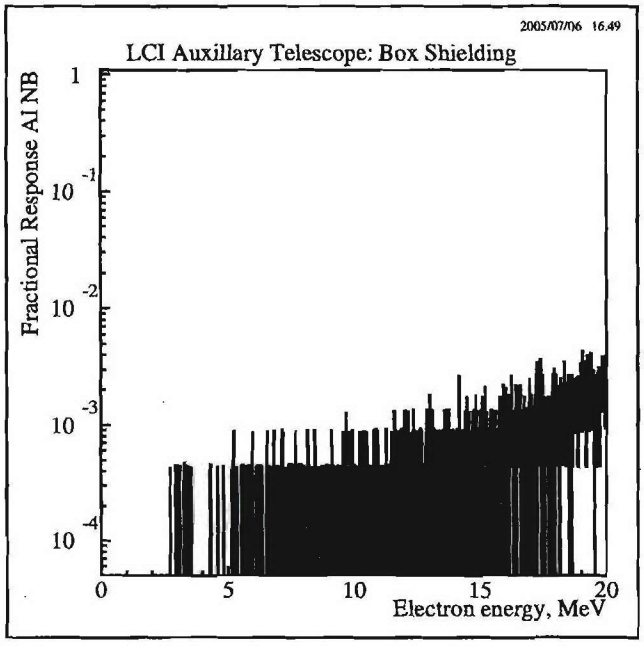


Figure 10: Probability that an electron of given energy will trigger A but not trigger B.

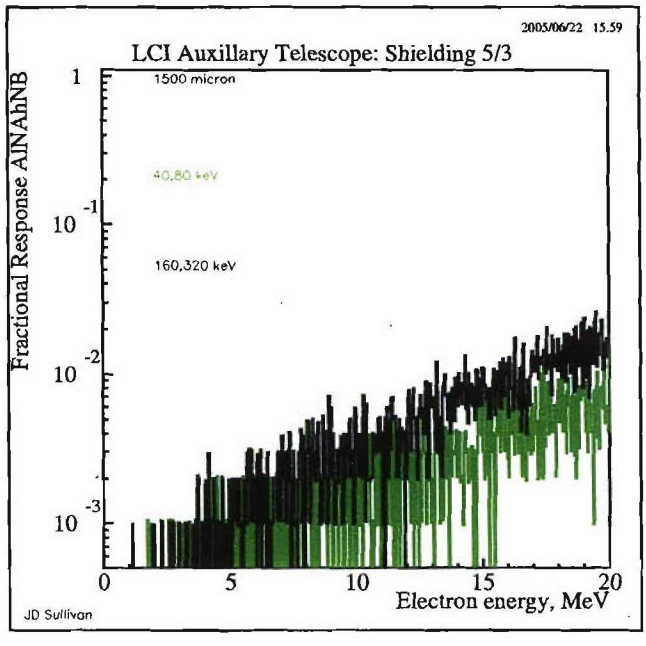


Figure 11: Probability that an electron of given energy will not trigger B while depositing either 40–80 keV or 160–320 keV in A

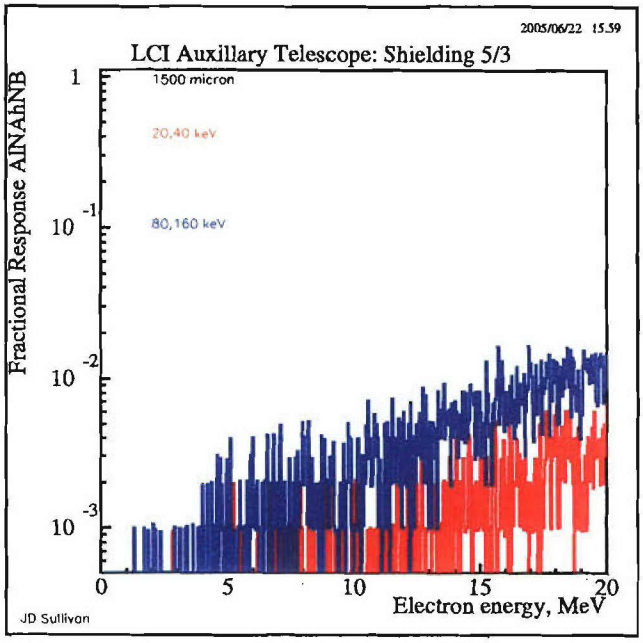


Figure 12: Probability that an electron of given energy will not trigger B while depositing either 20–40 keV or 80–160 keV in A

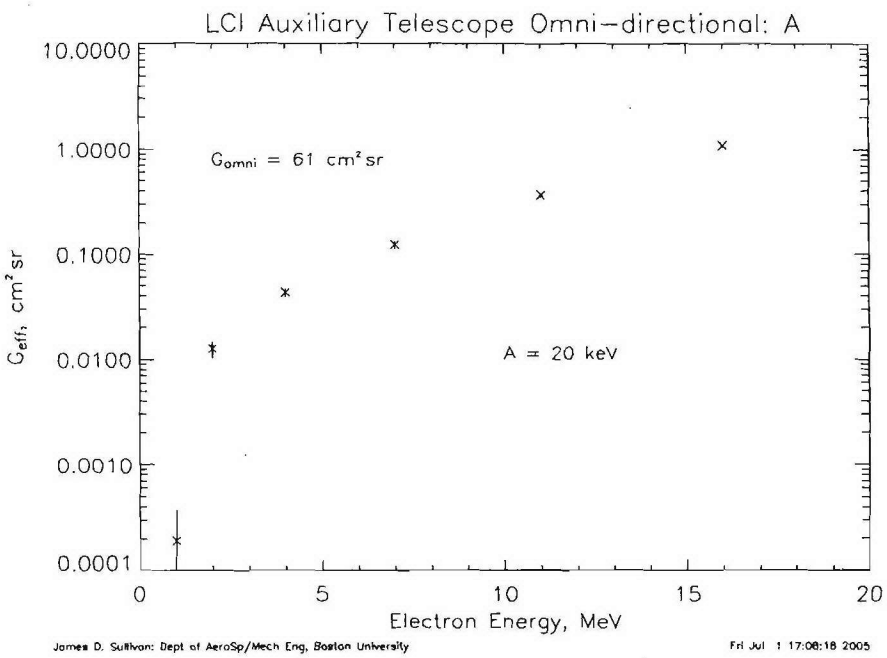


Figure 13: The effective geometrical factor of omni-directional electrons penetrating a closed cylindrical box comprising **5** g/cm$^2$ of AL followed by **3.1** g/cm$^2$ of W and depositing **20** keV in detector A

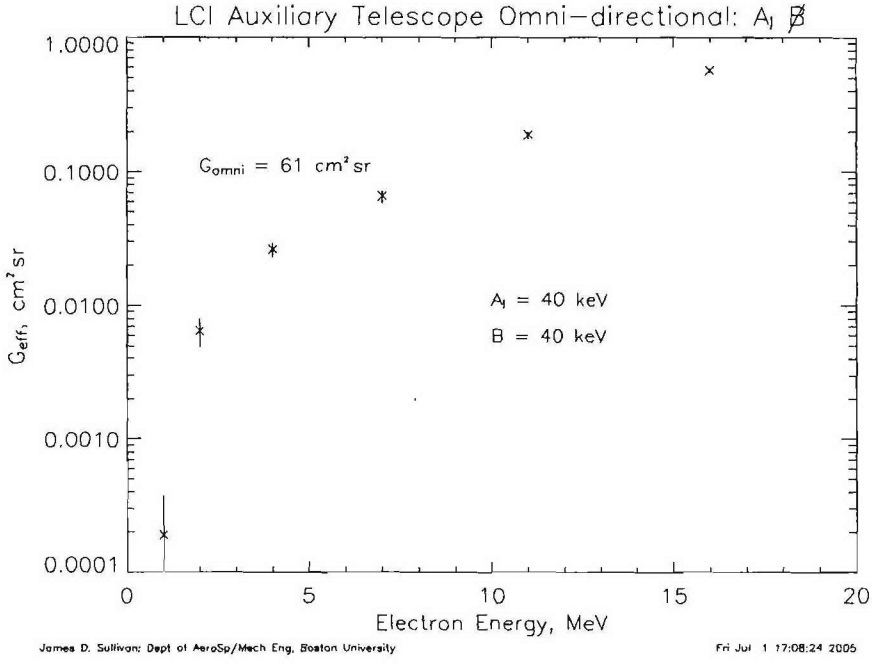


Figure 14: The effective geometrical factor of omni-directional electrons penetrating a closed cylindrical box comprising **5** g/cm$^2$ of AL followed by **3.1** g/cm$^2$ of W and depositing **40** keV in detector A but less than **40** keV in detector B

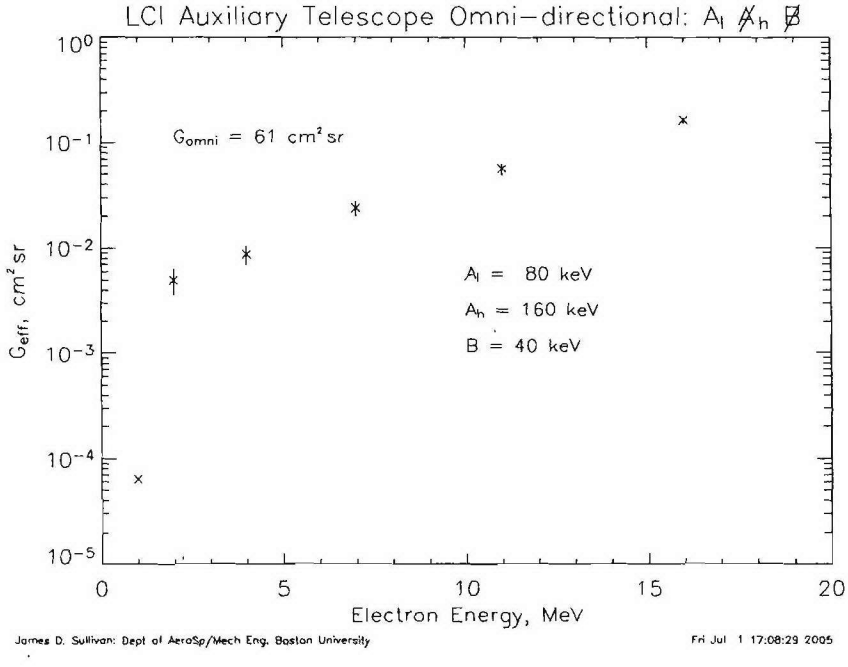


Figure 15: The effective geometrical factor of omni-directional electrons penetrating a closed cylindrical box comprising **5** g/cm$^2$ of AL followed by **3.1** g/cm$^2$ of W and depositing between **80** keV and **160** keV in detector A but less than **40** keV in detector B

# APPENDIX B: HST DESIGN STUDY (J. Sullivan)

# Material Considerations for the Radiation Shield in the HST Collimator

**Charles Parker**
Boston University
Center for Space Physics
2006-05-25

## Material Requirements

The purpose of the high sensitivity telescope (HST) is to collect electron radiation from a narrow field of view. As such the geometry and materials comprising the housing for the telescope must be able to reject sources of radiation that are not in this field of view. Geometrically, a long column will be used to limit the field of view. However, this will only work if the material comprising the column is able to reject radiation from all other directions. A materials ability to reject radiation increases with both its thickness and its density.

Since this is a space application, weight is a concern. Therefore, the entire radiation shield cannot be comprised of a dense metal because such a shield would not meet the weight restrictions of the instrument. Therefore a combination of a thin dense material and a thicker, lighter material may be used to achieve the desired level of shielding. The shield should be able to stop an incoming proton with an energy of up to 80 MeV.

Additionally, the material must be non-magnetic so that the magnetometers on board are not influenced by its presence.

## Materials Considered

Many of the other components of the spacecraft will be using aluminum parts because aluminum is both lightweight and easy to work with from a machining standpoint. For consistency the lighter material used in the shielding may be aluminum.

The dense material being considered is tungsten. Tungsten has a density of 19.25 g/cm$^3$ near room temperature, making it one of the densest available metals. In its pure form it is non-magnetic. However, in its pure form it is also a very brittle material and therefore difficult to machine. There do exists tungsten alloys, having the desired density, that are considerably easier to work with. Examples of such metals are shown below in Table 1 which is a sample of available alloys from Mi-Tech Metals Inc.. Some of these alloys include iron which increases the density of the material but also adds a slight magnetism to the material making them unacceptable for this application.

Various alloys of tungsten and copper are available with percentages of tungsten ranging from 55% to 80%. These alloys have densities ranging from 12.5 g/cm$^3$ to (55% W) to 15.56 g/cm$^3$ (80% W). These alloys are all non-magnetic, but have densities that are lower then those shown in Table 1.

Additionally, alloys of tungsten and rhenium were considered. However, rhenium is a magnetic material, therefore these alloys are not acceptable for this application.

| | HD17<br>90% W<br>6% Ni<br>4% Cu | HD17BB<br>90% W<br>6% Ni<br>4% Cu/Fe | HD18<br>95% W<br>3.5 % Ni<br>1.5% Cu | HD18D<br>95% W<br>3.5% Ni<br>1.5% Fe | HD18.5<br>97% W<br>2.1% Ni<br>0.9% Fe |
|---|---|---|---|---|---|
| AMS-T-21014 | Class 1 | | Class 3 | Class 3 | Class 4 |
| SAE Aero, Material Spec. (AMS 7725C) | 7725C | | -- | -- | -- |
| ASTM-B-777-99 | Class 1 | | Class 3 | Class 3 | Class 4 |
| Density (g/cm$^3$) | 17 | | 18 | 18 | 18.5 |
| Hardness Rockwell C | 24 | | 27 | 27 | 28 |
| Ultimate Tensile Strength (psi) | 110,000 | | 115,000 | 125,000 | 128,000 |
| Coefficient of Thermal Expansion x $10^{-6}$ / °C (20-400 °C) | 5.4 | | 4.4 | 4.6 | 4.5 |
| Thermal Conductivity (CGS Units) | 0.23 | | 0.33 | 0.26 | 0.30 |
| Magnetic Properties | Nil | Slightly Magnetic | Nil | Slightly Magnetic | Slightly Magnetic |

*Table 1: Sample of available tungsten alloys from Mi-Tech Metals Inc. and some of their physical properties. Data taken from Mi-Tech Metals Inc. material documents.*

## Material Availability

The following companies were contacted regarding the availability and cost of the HD17 and HD18 alloys from Table 1:

- Mi-Tech Metals Inc
- Ed Fagan Inc.
- Eagle Alloys Corp.
- B&S Aircraft Parts Inc.
- Aviation Metals Inc.
- Marketech International Inc.
- Rhenium Alloys Inc.

These alloys are more complex then the W-Cu alloys and therefore the cost should be greater then that of the W-Cu alloys. The quotes coming back from these companies should therefore establish an upper bound on the cost of the materials.

All of the above materials are available in rod, bar, and sheet form. None of the above manufacturers form these alloys in tube form. In order to produce a tube, a rod would be formed and then a hold bored through the center. Some of the above manufactures would be willing to do this, depending on the required length of the tube.

Since a tube would be formed in this fashion, just about any wall thickness can be obtained, although producing a thinner wall is more difficult from a machinist's point of view. These rods are typically available in lengths of 12" with diameters up to 6", although larger diameters are available from some of the manufacturers.

Sheets are available in almost any thickness required.

## Material Cost

The only company willing to give a ballpark cost estimate over the phone was Mi-Tech Metals Inc. They estimated that 2" diameter rods of the HD17BB alloy would cost ~$925 / ft. Based on the initial estimates of the length and diameter requirements made by David DeLaurentis, a single 2" dia. x 12" long rod would be sufficient for the tubing of this part.

The current collimator design, a rough sketch of which is attached as Appendix A, also requires the fabrication of a flange that can be used to attach the part to the aluminum housing of the HST. Since the dimensions of this flange have not yet been determined, a large dimension was assumed to provide an upper estimate of the material cost. A 3.5"x3.5"x0.5" slab of the HD18D alloy is estimated to cost ~$400.

The material estimates above are purposefully over-estimated to provide an upper bound on the material cost. Given the high cost of this material, only just enough material to make the part should be ordered. When the exact dimensions of the parts are determined, a more precise estimate of the material cost can be determined.

It should be noted that other parts will also need to be fabricated out of this material, i.e. the components that make the detector housing. It is not meaningful to estimate the cost of these since the dimensions have not yet been determined and only a small amount of material will be used in their fabrication.

Some of the above companies also offer machining services. Once the dimensions of the parts have been determined, estimates for the cost of machining can be made to determine if it is more cost effective to have the suppliers machine the parts, or to have the BU Scientific Instruments Facility machine the raw materials.

## Material Recommendation

The HD18 material is the recommended material for this application. Of all the machine workable non-magnetic materials, it has the highest density, and therefore the greatest radiation stopping ability. Additionally, tungsten and nickel are both thermally compatible with aluminum, while the use of copper will produce a thermal differential across the interface with the aluminum. Such a differential may be useful as a method of removing heat from the detector cavity, however, the current design does not incorporate this effect.

# Summary of Working Memo #1: Proposed Detector Sizes for the High Sensitivity Telescope

Charles W. Parker

June 16, 2006

The current dimensions for the charged particle detectors in the High Sensitivity Telescope (HST) are adequate to make the measurements specified of the telescope. Option 1 in Table 1, however, is better because of a decreased cutoff angle, and a rear detector that doesn't overfill the acceptance cone.

Table 1 presents four sets of design options:

- **Option 1:** The collimator is lengthed while the sensitive diameter of the front detector is increased and the sensitive diameter of the rear detector is reduced.
- **Option 2:** The collimator is lengthed while the sensitive diameter of the front detector is increased and the rear detector does not change.
- **Option 3:** The collimator length does not change and the rear detector's active diameter is reduced.
- **Option 4:** The current configuration. No changes are made.

The rear detector is larger then it needs to be and overfills the acceptance cone in the current detector stack configuration. Reducing the size of the rear detector will decrease the detected omni-directional background radiation, resulting in an improved signal-to-noise ratio. This reduction is present in options 1 and 3.

Options 1 and 2 reduce the cutoff angle of the instrument from **6.8°** to **6.3°** by lengthening the collimator slightly. This lengthening demands an increase in the sensitive diameter of the front detector in order to maintain a geometrical factor of factor: **0.1** $\text{cm}^2 \cdot \text{sr}$. This lengthening, however, also slightly increases the mass.

Figure 1 shows the tradeoffs among the collimator parameters, the geometrical factor, and the cutoff angle.

Option 1 is appears to be superior to the others because of the reduced cutoff angle and decreased omni-directional background. Option 3 is also preferable to option 4 because of the decreased omni-directional background radiation.

Additional details can be found in the forthcoming memo CWP/LCI WM1.

| Parameter | Option 1 | Option 2 | Option 3 | Option 4 |
|---|---|---|---|---|
| Cutoff Angle (deg): | **6.3** | **6.3** | **6.8** | **6.8** |
| Front Detector Sensitive Diameter (cm): | **3.750** | **3.750** | **3.500** | **3.500** |
| Rear Detector Sensitive Diameter (cm): | **3.898** | **4.000** | **3.898** | **4.000** |
| Collimator ID (cm): | **3.645** | **3.645** | **3.387** | **3.387** |
| Collimator Length (cm): | **33.017** | **33.017** | **28.402** | **28.402** |
| Approx. Mass Increase (kg): | **0.42** | **0.42** | **0** | **0** |

Table 1: Additional parameters: geometrical factor: **0.1** $\text{cm}^2 \cdot \text{sr}$; detector/collimator spacing: **0.475** cm; detector/detector spacing: **0.669** cm

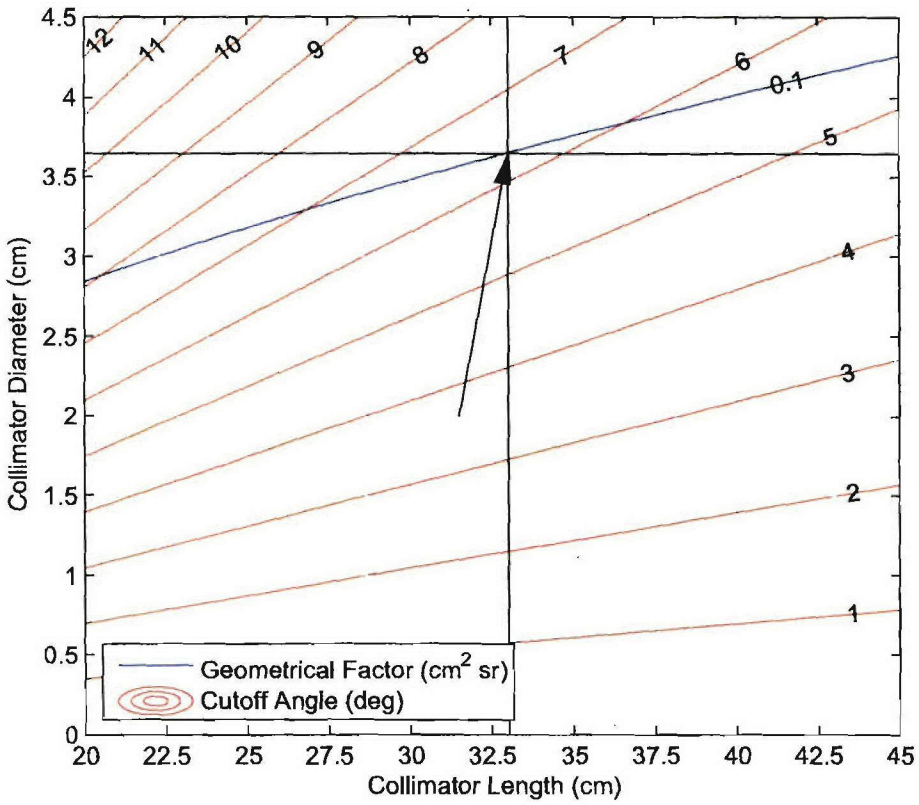


Figure 1: An illustration of the tradeoffs that can be made between the collimator parameters. The recommended point is indicated and represents the following parameters: detector diameter: **3.75** cm; collimator diameter: **3.65** cm; collimator length: **33.02** cm; geometrical factor: **0.1** $\text{cm}^2 \cdot \text{sr}$ cutoff angle: **6.30°**

# APPENDIX C: READOUT ELECTRONICS DEVELOPMENT (Q. Zhai)

Boston University

College of Engineering

Department of Electrical and Computer Engineering

Prospectus Dissertation

# DEVELOPMENT OF THE ΔE-E PARTICLE IDENTIFICATION TELESCOPE READOUT SYSTEM

by

QINGTAI ZHAI.

Submitted in partial fulfillment of the
Requirements for the degree of
Doctor of Philosophy
[2006]

Advisory Committee:

Professor Theodore A. Fritz
Professor Anton Mavretic, chair
Professor Ronald Knepper
Professor Michael Ruane
Professor Enrico Bellotti

# Table of Contents

# List of Figures

# List of Tables

# Chapter 1: Introduction

Energetic particles, most notably electrons and ions with energy from 30keV to 500keV, are very important in the Earth's magnetosphere. Understanding the energy and flux of energetic particles inside and outside of radiation belt is more useful for spacecraft and satellite safety around that area.

The SOPA instrument is flown on a series of LANL satellites beginning in 1989. It is designed to provide high spatial, high-resolution energetic particle measurements at geo-synchronous orbit. It is also the first instrument using dE/dx to monitor electrons, protons, helium and heavier ions. The instrument consists of three solid state detector telescopes that accept particles from three different directions. Each telescope consists of a thin 4μm front detector followed by a thick, 3000μm back detector. A collimator, with 11 degree field of view fronts the detector stack. The energy range covers from 50keV to a few MeVs.

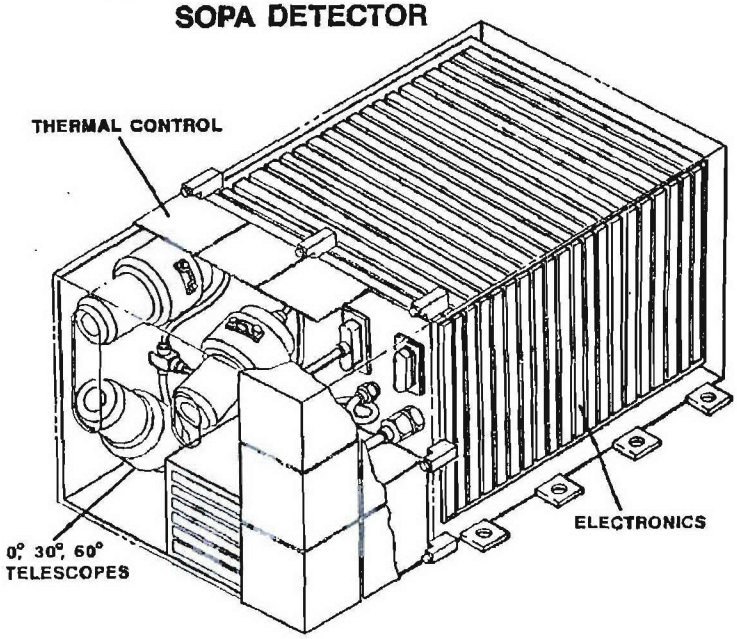


Fig. 1.1 SOPA detector

In 1987/88 ESA selected RAPID( Research with Adaptive Particle Imaging Detectors) as a payload for its multi-spacecraft mission CLUSTER. There are two instrument integrated in RAPID: IIMS and IES. For ions the IIMS (Imaging Ion Mass Spectrometer) returns information on the particle's atomic mass A, and the velocity vector V. IES (Imaging Electron Spectrometer) gives energy and velocity of electrons. The two sensor systems share an analog and digital electronic box shown in Fig. 1.2. IIMS covers the energy range 30keV to 1.5MeV for ions and 30 to 450keV for electrons, it returns information on the particle's direction of incidence with 12 angular intervals over 180 degree field-of-view. IES is dedicated to electrons between

30 to 450keV. IES, based on pin-hole camera, has 20 degree angular resolution over 180 degree field-of-view. The total weight of the complete instrument is 5.5kg.

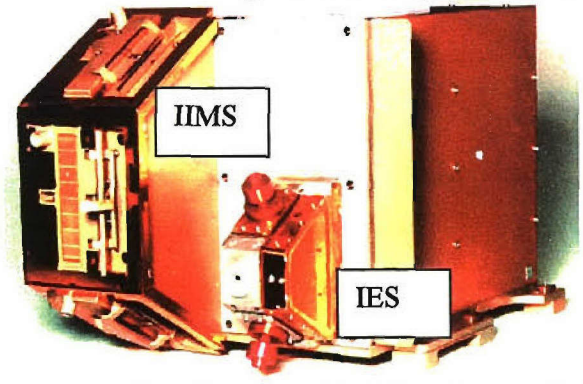


Fig. 1.2 RAPID instrument onboard NASA-ESA joint Cluster mission.

In the thesis we'll describe a new design concept of particle identification telescope. It will inherit dE/dx from SOPA and pin-hole camera from IES. A multi-channel amplifier will be used for signal processing to make it low weight, low cost, high reliability and reproducibility. The new instrument will have higher angular resolution over 180 degree field-of-view.

# Chapter 2: Background

## 2.1 Magnetosphere

Interplanetary space seems dark, still, and empty. However, discoveries made since the beginning of the space program in 1958 reveal that the Earth's near-space environment is not empty. It is filled with charged particles, magnetic fields, electric fields, and activity invisible to the naked eye but readily apparent to more sensitive scientific instruments. In space, a region close to Earth, just above the ionosphere, is called the magnetosphere. Sketched in Fig. 2.1, Earth's magnetic field extends far above atmosphere and is similar in overall structure to the field of a gigantic bar magnet. The Earth's magnetic field extends far out into space for fews of Earth Radii (1 Re = 6378 km).

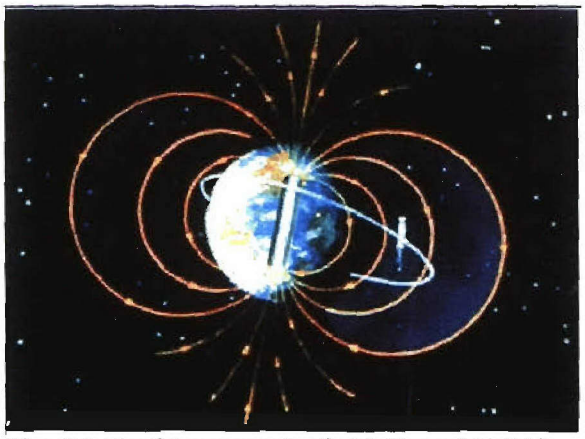

Fig. 2.1 Earth's magnetic field (from NASA)

The solar wind travels from the Sun at around speed of 450km/s towards the earth. When the solar wind encounters with the earth's magnetosphere, the Earth's magnetosphere will be compressed at the dayside into a distance of 6-10 Earth radii, and it drags out at the night-side (so called magnetotail) to perhaps 1000 Earth radii. An overall shape of the magnetosphere is illustrated in Figure 2.2. The magnetosphere forms a buffer zone between the Earth and the charged particles of the solar wind. The magnetopause is the border between the Earth's environment and the solar wind charged particles. The Earth's magnetic field dominates the inside the magnetopause and the interplanetary magnetic field dominates the outside the magnetopause.

## 2.2 Radiation Belt

In 1958 a Geiger counter mounted onboard the US first satellite, Explorer 1, provided surprising evidence that the Earth is surrounded by intense particle radiation. Subsequent missions and experiments collected data on this particle population and found that two huge zones of trapped electrons and protons encircle the Earth like donuts, Fig. 2.3, one located about 3000 km and the other 20,000 km above Earth's surface. These belts bear the name of the discoverer, the Van Allen radiation Belt. The two Van Allen radiation belts contain particles trapped by the Earth's magnetic

field. The main constituent of the inner belt is high-energy protons, produced when cosmic rays blast particles out of the upper atmosphere. The outer belt is populated chiefly with high-energy electrons produced by cosmic rays and magnetospheric acceleration processes.

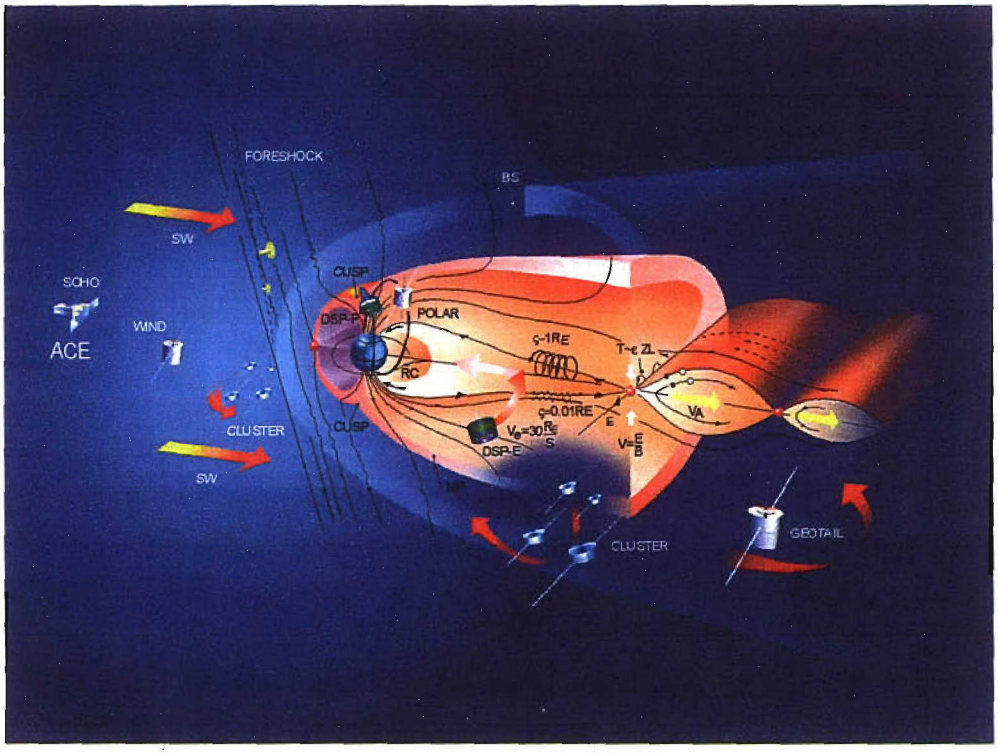


Fig.2.2 Three dimensional view of the Earth's magnetosphere with ISTP satellites Geotail, Polar, SOHO and Cluster.

Charged particles, mainly electrons and protons from the solar wind can become trapped by Earth's magnetospheric dynamic process. Earth's magnetic field exerts electromagnetic control over these particles, herding them into the Van Allen belts. During geomagnetic quiet conditions in the magnetosphere, particles neither enter nor escape these trapped orbits. However, when the geomagnetic field is disturbed, the high energy particles in the magnetospheric region may be loss via the loss cone into the Earth's atmosphere to produce Aurora.

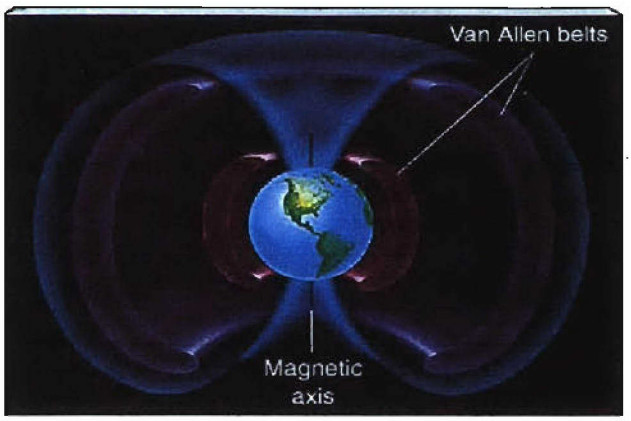


Fig 2.3 Van Allen Belts (E. Chaisson, S.McMillan Astronomy)

## 2.3 Loss Cone

Charged particles moving in the Earth's magnetic field travel in spiral paths around the geomagnetic field lines. Their helical trajectories result from the fact that their motion is both parallel and perpendicular to the magnetic field, which exerts a force on the perpendicular component of their velocity that causes them to move around the field lines ("cyclotron" motion) as well as along them. The angle between the direction of the magnetic field and a particle's spiral trajectory is referred to as the "pitch angle" of the charged particle. In a non-uniform magnetic field, the pitch angle changes as the ratio between the perpendicular and parallel components of the particle velocity changes. Pitch angle is important because it is a key factor in determining whether a charged particle will be lost to the Earth's atmosphere or not.

As particles spiraling along geomagnetic field lines get closer to the Earth, the strength of the magnetic field increases, which causes the parallel component of the particles' velocity to decrease (with a corresponding increase in the perpendicular component since the particle energy is conserved). As the parallel component goes to zero, the pitch angle increases to 90 degrees. If this happens at an altitude where the atmosphere is sufficiently tenuous (above ~100 km) that the particles are unlikely to interact with atmospheric neutrals and ions, they reverse direction and travel back up the field lines. They continue spiraling along the field lines until they reach a point in the opposite hemisphere where the magnetic field strength is sufficient to cause them to reverse direction again. The points at which the pitch angle goes to 90 degrees and the particles reverse direction are known as "mirror points." Charged particles that are reflected back and forth along geomagnetic field lines between mirror points--such as those that constitute the ring current and the radiation belts--are considered "trapped" and their repeated reflection between mirror points is known as their "bounce" motion.

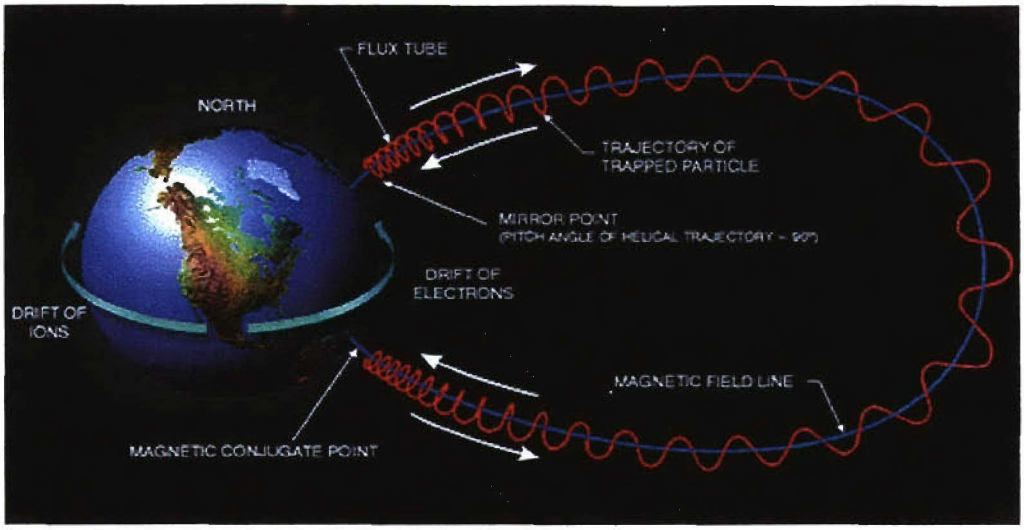


Fig. 2.4 The three basic motions of charged particles in a magnetic field: gyro, bounce between mirror points, and drift. (Based on Figure 5-10 in the "Handbook of Geophysics and the Space Environment," edited by A. S. Jursa and published by the United States Air Force, 1985.)

Not all charged particles gyrating along geomagnetic field lines become or remain trapped, however. If the mirror point occurs at an altitude where the atmosphere is dense enough for a charged particle to collide with atmospheric neutral particles (that is, below ~100 km), the particle will soon be absorbed by the atmosphere instead of being continuously reflected by the magnetic mirror force. Particles lost in this way must have pitch angles (in the equatorial plane, where the magnetic field is weakest) that fall within a solid angle known as the atmospheric *"loss cone."* The size of the loss cone varies with the radial distance of the field line from the Earth: the greater the distance, the smaller the angle of the loss cone. At L = 8, for example, the loss cone angle is about 2 degrees, see Figure 2.5. Thus charged particles with equatorial pitch angles of 2 degrees or less will, after a few bounces, be lost to the atmosphere as result of collisions with atmospheric neutrals and ions. Those with pitch angles greater than the loss cone angle will continue to bounce between mirror points until an interaction with a plasma wave reduces their pitch angle and "scatters" them into the loss cone. "Pitch angle scattering" (also known as "pitch angle diffusion") is one of the two main processes by which magnetospheric charged particles (both ions and electrons) are lost to the atmosphere.

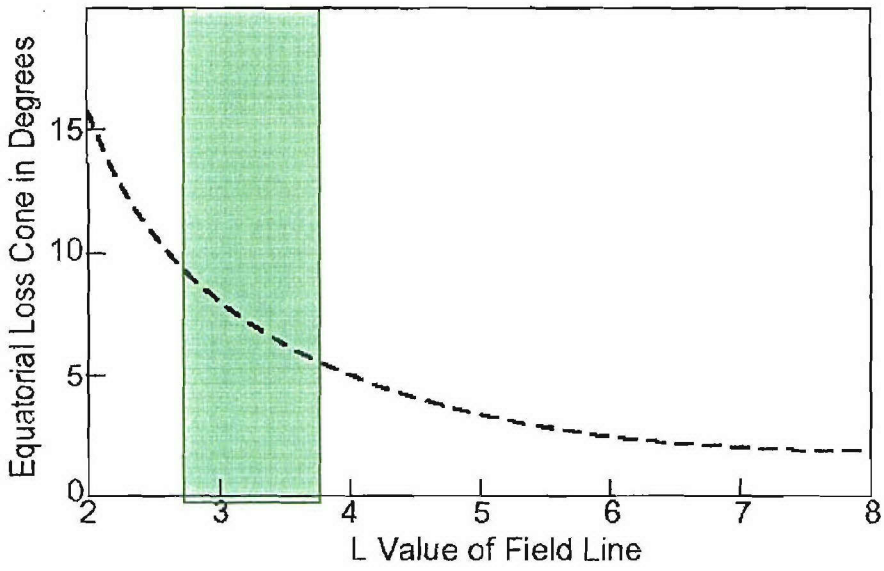


Figure 2.5: Equatorial loss cone as a function of L value (The distance to the center of the Earth, in Re).

## 2.4 Radiation Detection

### 2.3.1 Solid state semiconductor detector

Semiconductor detector has been used as particle sensor practically in early 1960s. Now, it became to be widespread because of it many desirable features. Among these are good energy resolution, its compact size, relatively fast timing characteristics, and an effective thickness which can be made to match different applications [1]

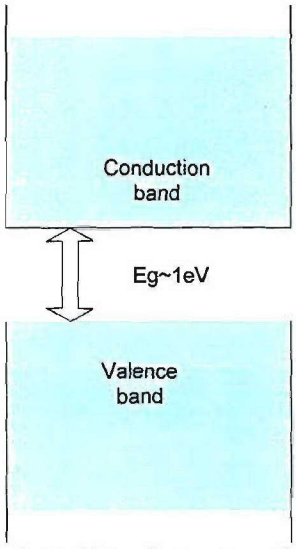

Fig.2.6 Band structure for electron energies in semiconductor

The periodic lattice of crystalline materials establishes allowed energy bands for electrons that exist within that solid. The energy of any electrons within the pure material must be confines to one of these energy bands which may be separated by gaps of forbidden energies. Fig.2.6 shows the band structure of semiconductor. The lower band, called the valence band, corresponds to those electrons that are bound to specific lattice sites within the crystal. The next higher-lying band is called the conduction band and represents electrons that are free to move through the lattice. Electrons in this band contribute to the electrical conductivity of the material. The two bands are separated by the band gap, the size of which determines whether the material is classified as a semiconductor or an insulator. The number of electrons within the crystal is just adequate to completely fill all available sites within the valence band. Without thermal excitation both insulators and semiconductors have a configuration in which valence band is completely full, and conduction band is completely empty. Neither would theoretically show any electrical conductivity. In a metal, the highest occupied energy band is not completely full. Therefore, electrons can easily migrate throughout the material because they need achieve only small energy to be above the occupied states. Metal, therefore, are always characterized by very high electrical conductivity. In insulators or semiconductors, the electrons must first across the band gap in order to reach the conduction band and conductivity is therefore much lower. For insulators, the band gap is usually 5eV or more, whereas for semiconductors, the gap is considerably less.

**2.4.1.1 The Action of ionizing radiation in semiconductor**

When a charged particle passes through a semiconductor with a band structure in Fig. 1, the overall significant effect is the production of electron-hole pairs along the track of the particle. This may be either direct or indirect, in that the particle produces high-energy electrons which subsequently lose their energy in producing more electron-hole pairs. The quantity of practical interest for detector applications is the average energy expended by the primary charged particle to produce on electron-hole pair. This quantity is called "ionization energy"—'$w$'. The average amount of energy spent when an electron-hole pair is created is given by[2]

$$w=E_i+rE_R+2E_f \qquad (1.1.1.1)$$

1) The production of an electron-hole pair, which absorbs an amount of energy Ei.
2) For every pair generated there is, on average, an energy rER transferred to the lattice (in the form of photons) by carriers having a kinetic energy greater Ei.

3) At the end of the ionization process every carrier has a kinetic energy less than Ei, so that it can no longer ionize. $E_f$ is the mean value of this "final" energy, which is transferred to lattice vibrations.

According to Shockley model, carriers with kinetic energies greater than Ei are scattered by phonons of this frequency only. The numerical values of $E_R$, deduced from neutron diffraction measurements, are $E_R$ =0.063±0.003eV for Si [3], and $E_R$ =0.037eV for Ge. [4] The parameter r, which relates the ionization and Raman scattering probabilities, allows Shockley to foresee the behavior of the quantum yield for energies greater than the threshold. rER is obtained by fitting the theory to the experimental points.

As far as $E_f$ is concerned, Shockley assumes that the carriers, as finally produced, are equally likely to be found anywhere in the Brillouin zone with an energy less that $E_i$. Therefore, for parabolic energy surfaces, the results is

$$E_f = 0.6E_i \qquad (1.1.1.2)$$

and

$$w = 2.2E_i + rE_R \qquad (1.1.1.3)$$

The calculation of $w$ requires the knowledge of $E_i$ and $E_R$. These values are derived from a suitable interpretation of quantum yield experiments. From the results done by Vavilov [5], The minimum energy required Ei to produce one pair is forbidden gap energy Eg. At 300K, for Si: r = 54, By inserting the values, one obtains, $w$= 3.5eV (Si).

**TABLE 2-1 Properties of Intrinsic Silicon and Germanium**

| | Si | Ge |
|---|---|---|
| Atomic number | 14 | 32 |
| Atomic weight | 28.09 | 72.60 |
| Stable isotope mass numbers | 28-29-30 | 70-72-73-74-76 |
| Density (300K); $gcm^{-3}$ | 2.33 | 5.33 |
| Atoms $cm^{-3}$ | 4.96E22 | 4.41E22 |
| Dielectric constant | 12 | 16 |
| Forbidden energy gap (300K); eV | 1.115 | 0.665 |
| Forbidden energy gap (0K); eV | 1.165 | 0.746 |
| Intrinsic carrier density (300K); $cm^{-3}$ | 1.5E10 | 2.4E13 |
| Intrinsic resistivity (300K); Ωcm | 2.3E5 | 47 |
| Electron mobility (300K); $cm^2/V\text{-}s$ | 1350 | 3900 |
| Hole mobility (300K); $cm^2/V\text{-}s$ | 480 | 1900 |
| Energy per electron-hole pair (300K); eV | 3.62 | |
| Energy per electron-hole pair (77K); eV | 3.76 | 2.96 |

From G.Bertolini and A.Coche, Eds., "Semiconductor Detectors," Elsevier-North Holland Amsterdam (1968)

### 2.4.1.2. Surface-Barrier Detector

Surface-barrier diodes can be used as radiation detectors. They are essentially make of a single crystal slice of silicon which has been suitably treated, and on

which a metal has been deposited. This metal is gold in general. Fig.2.7 shows the N-type Silicon surface-barrier detector.

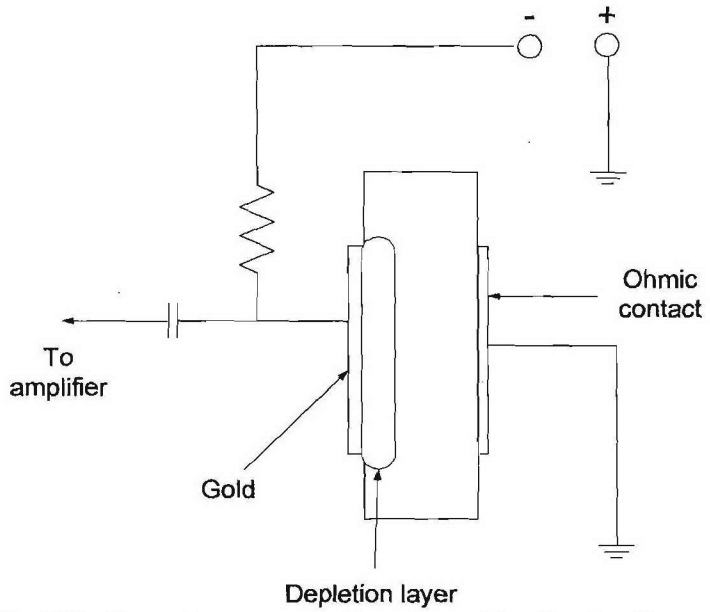


Fig. 2.7 schematic representation of a surface-barrier detector (gold-N-type silicon

In 1939, Schottky[6] published a theory concerning the rectification occurring at the contact between a metal and a semiconductor. His theory can explain the main electrical characteristics (depletion layer, capacitance, current, etc.). According to Schottky, when a metal and a semiconductor are brought into contact, a contact emf appears between the two materials which lower the semiconductor energy levels. This contact emf therefore depends only on the Fermi levels involved, or in other words, on the energy required to liberated electrons in the two materials. In analogy to P-N junction, a depletion layer without free carriers is formed, but it is rather obvious that this layer is only within the semiconductor. The thickness of this depletion layer, X0, may be calculated by an application of Poisson's equation, and may be expressed by N-P junction equation.[7]

$$X_0 = \left( \frac{2\varepsilon V_0}{qN_D} \right)^{\frac{1}{2}} \qquad (1.1.1.4)$$

where $V_0, N_D$ , $\varepsilon$ and $q$ denote, respectively, the N-P junction potential, the concentrations of donors, dielectric constant and charge.

If an external bias V is applied, the expression may be written as

$$X = \left( \frac{2\varepsilon (V_0 + V)}{qN_D} \right)^{\frac{1}{2}} \qquad (1.1.1.5)$$

which reduces to

$$X \approx \left(\frac{2\varepsilon V}{qN_D}\right)^{\frac{1}{2}} = (2\varepsilon\mu_n\rho_N V)^{\frac{1}{2}}, \text{ if } V >> V_0 \qquad (1.1.1.6)$$

In order to detect electrons, thicker depletion layer is preferred. Using higher resistivity materials 40kΩcm are able to support reverse bias voltage of up to 1000volts. Under this conditions, the thickness of the depletion layer can be a few mm.

A detector with depletion layer having an area $A$ and capacitance $C$. The capacity of surface-barrier detectors is proportional to $V^{-1/2}$ and is given by [7]

$$C = A\left(\frac{\varepsilon}{2\rho_N\mu_n V}\right)^{\frac{1}{2}} \qquad (1.1.1.7)$$

### 2.4.2 Particle identification

In many nuclear physics experiments or space mission experiments, one does not only want to know the energy of particles but also its mass and/or charge. There are several ideas can be used for this purpose.

I. **The ΔE-E detector system**
The energy loss of a particle while it passes through matter is described by Bethe-Bloch equation []. In general, a heavier ion will deposit more energy per unit distance than light ion, which can be understood from the simplified equation $dE/dx \sim MZ^2/E$. If a particle passed through a thin detector (a few micrometers) and stopped in another thick detector, the energy loss in thin detector and the total energy can be obtained. The charge and mass of the incident particle can then be reconstructed. This method is used in the LCI sensor system.

II. **Time-of-Flight detector**
There is another way to determine the mass of a particle by measuring both velocity and energy of this particle. The mass M of a traveling particle can be determined unambiguously if the energy E and velocity V are known. A frequently used method is to utilize a pulsed beam, providing a start time for the particle, and the timing signal from the energy detector. Sometimes the start and stop are derived from two timing detectors, which can measure the flight time T a particle needs to travel for a known distance S. The energy signal comes from silicon detector or scintillation detector.

III. **Pulse shape analysis**
Semiconductor and scintillation detectors both deliver pulses of which the shapes are slightly dependent on the type and mass of the particles. There are several ways to electronically analyze this shape of which the prompt-delayed signal and the zero-crossing technique are the best know.[knoll] DSP technique is widely used in this pulse shape analysis.

## 2.5 DSX and Onboard Instrument

*Demonstration and Science Experiment (DSX)* is a satellite program from Air Force. The satellite will be launched in MEO orbit where the radiation belts sit in. One of the most important onboard experiments is *Radiation Belt Remediation*. They

are going to use VLF (Very Low Frequency) transmitter to populate the electrons in the radiation belt to Loss Cone. That will reduce the electron density inside the radiation belt. Boston University will provide a payload to measure the in-situ loss cone variance in orbit. The payload includes *Loss Cone Imager* (LCI) and *High Sensitive Telescope* (HST).

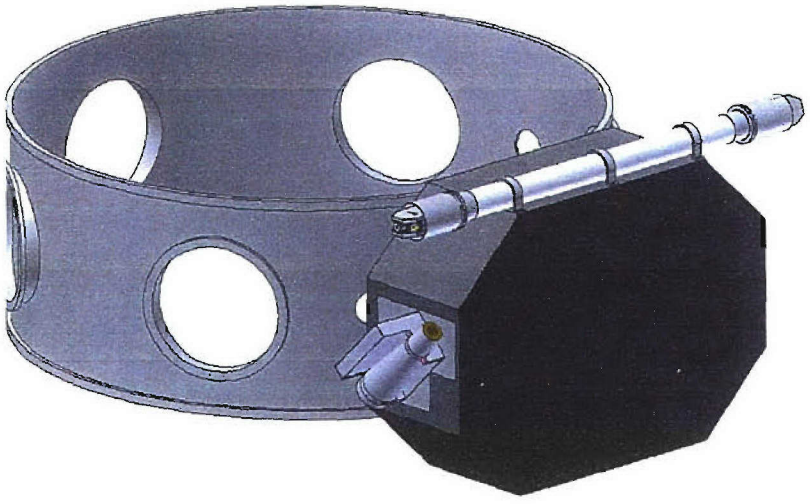

Fig. 2.8 Loss Cone Imager and High Sensitive Telescope mount on DSX

### ***2.5.1 Loss Cone Imager (LCI)***

LCI uses the pin-hole camera concept. Fig. 2.9 shows the concept of the telescope. Multiple look directions are achieved using a single detector with multiple

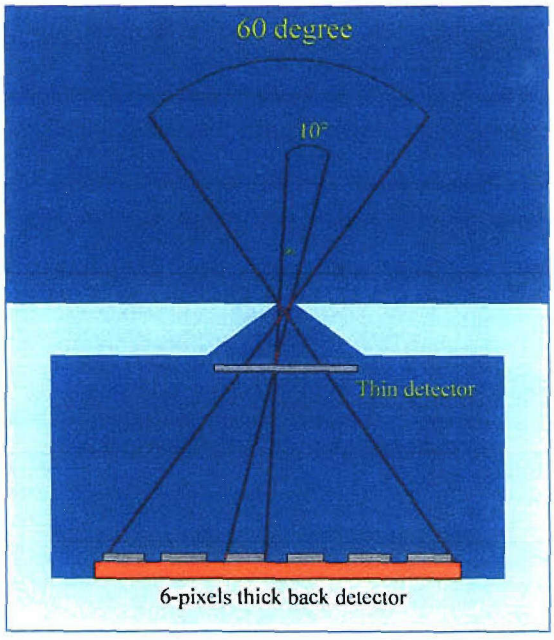


Fig. 2.9 LCI telescope concept using multiple pixels detector

pixels placed behind a pin slit. Each pixel has a 10 degree view angle and one detector covers 60 degree field of view. There are 3 identical telescopes on one LCI sensor head (Fig.2.10). The sensor head will be mounted on a scan platform sitting at the end of a composite tube. The energetic electron distribution measurement over the complete half unit sphere ($2\pi$) can be achieved. A thin detector telescope design will be incorporated into the pin-hole camera technique along with electronic circuitry to form a highly capable sensor system with very small dimensions. Using the $\Delta$E-E particle identification concept, the sensor system has capability of detecting energetic electrons over energy from 30 to 500 keV and 75 keV to 10 MeV for ions. By use of two such units mounted at opposing locations (e.g., two ends of composite tube), the complete unit sphere can be sampled. Further, the incoming and away particles can be measured simultaneously from opposite directions along the field line. This design allows understanding and quantification of the effects of the transmitter on the scattering of the trapped electron population into the loss cone.

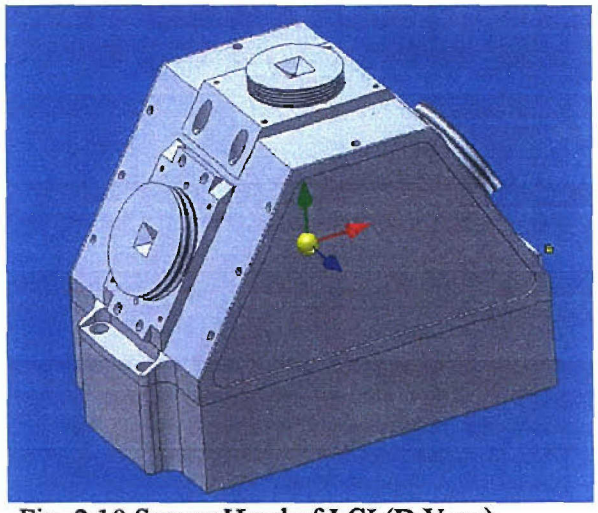

Fig. 2.10 Sensor Head of LCI (D.Voss)

***2.5.2 High Sensitive Telescope (HST)***

A separate two element Solid State Detector telescope called the High Sensitivity Telescope (HST) will be mounted on the DSX in order to obtain fluxes of energetic electrons along the geomagnetic field vector direction. This telescope is designed to have a geometric factor of 0.1 $cm^2$ ster with sufficient shielding to permit the detection of 100 particles/$cm^2$ sec ster in the loss cone. The HST will be mounted fixed to the DSX spacecraft such that it has an unobstructed view within +/- 20 degrees of the geomagnetic field vector when the satellite is being operated in a magnetic tracking mode.

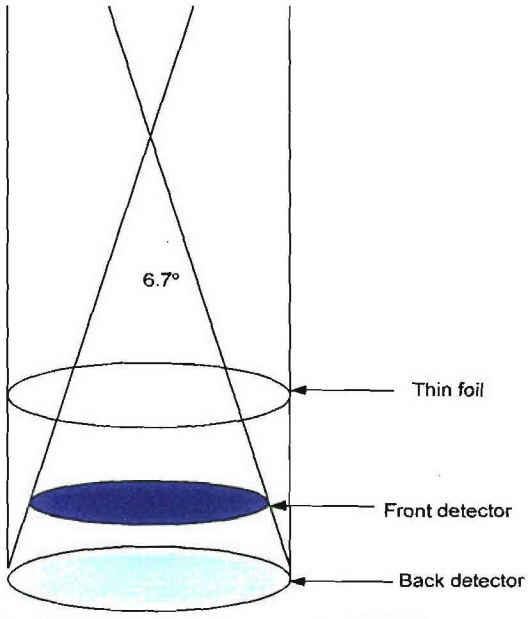

Fig. 2.11 detector placement of HST

# Chapter 3: Charge Sensitive Preamplifier

## *3.1 Voltage Sensitive vs. Charge Sensitive Amplifier*

The primary function of a preamplifier is to extract the signal from the detector without significantly degrading the intrinsic signal-to-noise ratio. Therefore, the preamplifier is located as close as possible to the detector, and the input circuits are designed to match the characteristics of the detector. Different pulse processing techniques are typically employed, depending on whether the arrival time or the amplitude (energy) of the detected event must be measured. Pulse shaping for either application is normally implemented in a subsequent module. Fig. 3.1 shows a typical voltage sensitive amplifier.

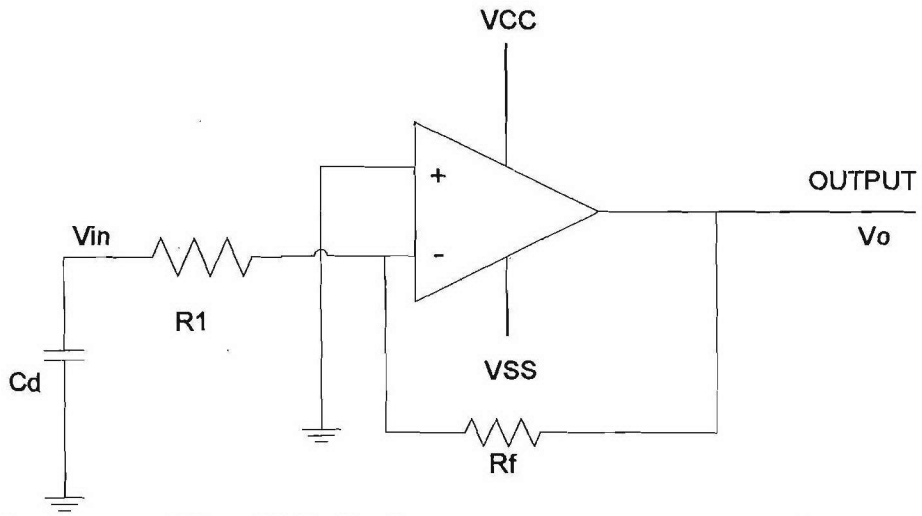


Fig. 3.1 voltage amplifier with feedback

The gain of the amplifier is given by

$$\frac{V_o}{V_{in}} = -\frac{R_f}{R_1} \tag{3.1}$$

$C_d$ is the capacitance of detector. The input voltage Vin is dependent on the charge Q on the detector

$$V_{in} = \frac{Q}{C_d} \tag{3.2}$$

When take 3.2 into account in 3.1, it is modified to

$$\frac{V_o}{Q/C_d} = -\frac{R_f}{R_1} \Rightarrow V_o = -\frac{R_f}{R_1} \cdot \frac{Q}{C_d} \tag{3.2}$$

We can see the output signal amplitude is depending on the capacitance of detector $C_d$. This capacitance dependence is a drawback, since from equation (1.1.1.7); we know the capacitance of detector can be dependent on detector bias voltage.

For a charge sensitive amplifier, the output voltage is independent on detector capacitance as shown in Fig.3.2

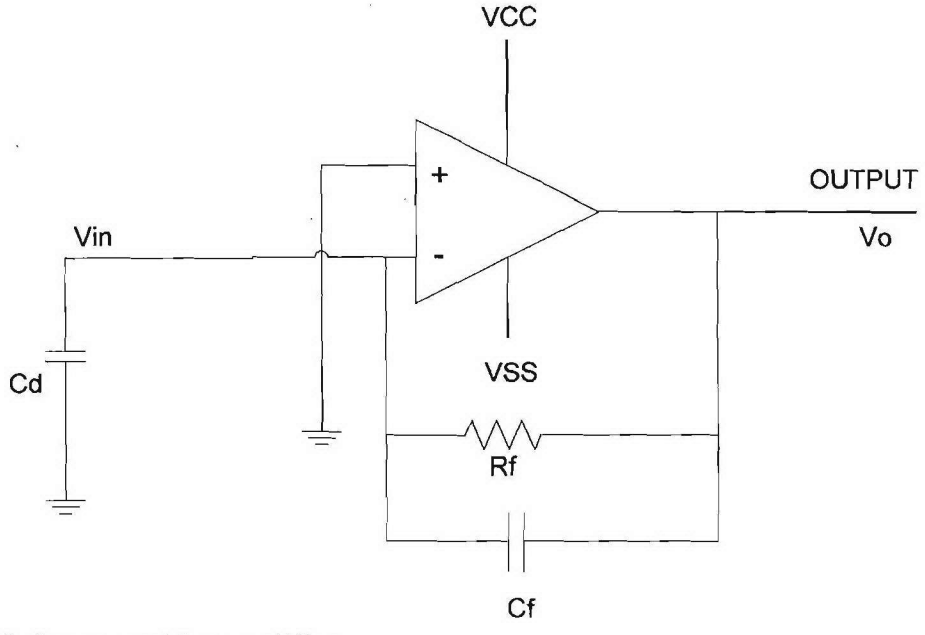


Fig. 3.2 charge sensitive amplifier

The capacitance at the negative input node of amplifier *Cin= Cd+(A+1)*Cf* where the miller effect cause the $C_f$ virtually increased by factor of (1+A), where A is the open loop gain of the amplifier. We assume the feedback resistor is very high and can be negligible. Then the input voltage

$$V_{in} = \frac{Q}{C_d + (A+1)C_f} \tag{3.3}$$

and the output voltage is

$$V_{out} = A \cdot V_{in} = \frac{A \cdot Q}{C_d + (A+1)C_f} = \frac{A \cdot Q}{(C_d + C_f) + A \cdot C_f} \tag{3.4}$$

if we assume $C_f + C_d << A \cdot C_f$, the 3.4 can be simplified to

$$V_{out} = \frac{Q}{C_f} \tag{3.5}$$

and the output is impendent on capacitance of detector. The output voltage is an exponentially decaying pulse with time constant $\tau = R_f \cdot C_f$ .

## *3.2 noise analysis of Charge Sensitive Amplifier*

### 3.2.1 Basic noise model

There are three main fundamental noise mechanisms in electronic circuit: thermal, shot and flicker noise. First we will describe these noise phenomena.

Thermal noise is due to the thermal excitation of charge carriers in a conductor. The random motion of electrons produces noise that has a white spectral density and is proportional to absolute temperature. J.B. Johnson first observed this kind of noise; and it is also called Johnson noise. The thermal noise of a resistor R may be modeled as a current source in parallel with the resistor or a voltage source in serial with a resistor. The mean square value of the current noise source $\overline{i_{th}^2}$ and voltage source $\overline{v_{th}^2}$ is given by,

$$\overline{i_{th}^2} = \frac{4kTdf}{R} \tag{3.6}$$

$$\overline{v_{th}^2} = 4kTRdf \tag{3.7}$$

where k is Boltzmann's constant and T is temperature in Kelvin

Shot noise was first studied by W. Schottky in connection with current fluctuations in thermionic diodes but it also occurs for minority carriers in P-N junctions. This noise occurs because the DC bias current is not smooth and the fluctuation of individual flow of carriers makes the noise. Shot noise can be model by,

$$\overline{i_s^2} = 2qI_b df \tag{3.8}$$

$q$ is electron charge, $I_b$ is the DC current.

Flicker noise is found in all active devices where a DC current is flowing. Flicker noise usually arises due to traps in the semiconductor where carriers that would normally constitute DC current are held for some time period and then released. The noise spectrum is commonly referred to as 1/f. For a JFET, flicker noise is modeled as a voltage noise source $\overline{v_f^2}$ in series with the gate,

$$\overline{v_f^2} = \frac{K_f}{C_g f} df \tag{3.9}$$

where $C_g$ is the gate capacitance and $K_f$ is the constant depends on device

### 3.2.2 Pre-amplifier noise model

Considering the radiation hardness, we use Amptek A250 and a front in JFET in the pre-amplifier. In order to optimize the noise performance, the detector noise model should be included. The model in Fig. 3.3 considers the primary noise sources as the bias resistor $R_b$ thermal noise; feedback resistor $R_f$ thermal noise; detector bias current $I_b$ shot noise; thermal noise for JFET channel resistance and flicker noise of JFET.

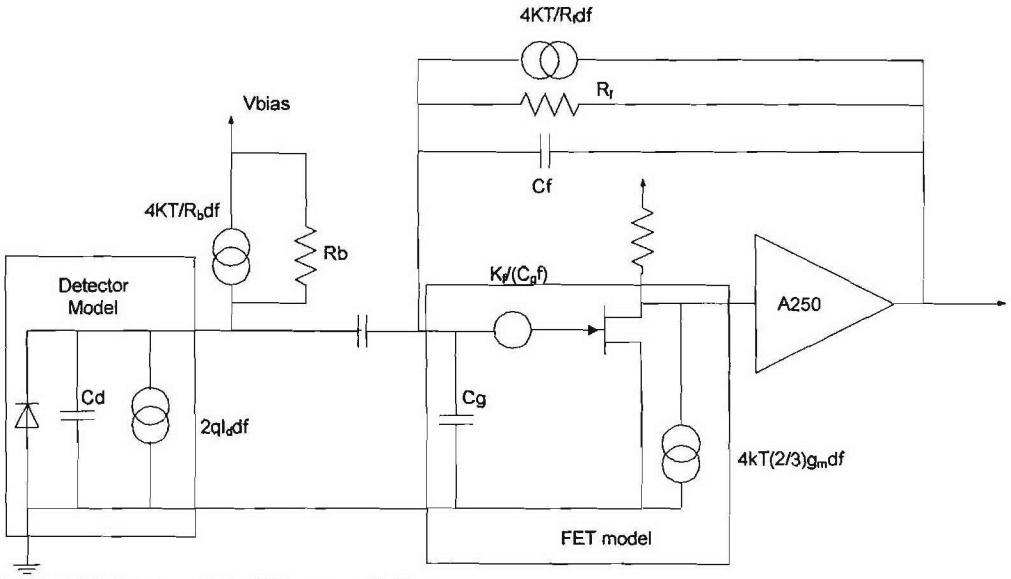

Fig. 3.3 Noise model of Pre-amplifier

Assume the open loop gain of A250 is large, for the FET gate noise source, the equivalent noise at the output of the amplifier is given by,

$$V_{out} = V_{FET}(\frac{Z_{in} + Z_f}{Z_{in}}) \tag{3.10}$$

$Z_{in}$ is the impedance looking back to the detector from the gate and $Z_f$ is the feedback impedance. At the frequencies respective of the pulse of the detector (> few of kHz), The detector capacitance Cd and feedback capacitance $C_f$ dominate the effective impedance. i.e. $Z_{in} = 1/j\omega C_d$, $Z_f = 1/j\omega C_f$.

For the current source at the input node, they charge up the feedback capacitor Cf. The transfer function from the current at input of the gate to the output is found by using nodal analysis [8],

$$V_{out} = Z_f(\frac{A_v}{1+A_v})\frac{1}{1+s(\frac{R_f C_T}{1+A_v})}I_{in} \tag{3.11}$$

Av is the total gain of the FET and opamp A250. Usually Av >>1, $C_T$ = Cd+Cg+Cf. and also $R_f C_T$ is much less that (Av+1), than 3.11 can be simplified to,

$$V_{out} = Z_f I_{in} = \frac{I_{in}}{j\omega C_f}$$

$$|V_{out}| = \frac{I_{in}}{\omega C_f} \tag{3.12}$$

using the transconductance definition in FET, $Vg = I_{ch}/g_m$, the thermal channel noise current source of the FET can be reflected to a voltage noise source at the gate,

$$\overline{V_{ch}^2} = \frac{4kT(2/3)}{g_m}df \tag{3.13}$$

Using previous equations (3.6) to (3.13), the total noise at the output is given by,

$$\overline{V_{total}^2} = (\frac{4kT}{R_b} + \frac{4kT}{R_f} + 2qI_d)(\frac{1}{\omega C_f})^2 df + \left[\frac{4kT(2/3)}{g_m} + \frac{K_f}{C_g f}\right]\left(\frac{C_g + C_d + C_f}{C_f}\right)^2 df$$

(3.14)

in most cases, the feedback capacitor $C_f$ is much smaller that $C_g$+$C_d$ than,

$$\overline{V_{total}^2} = (\frac{4kT}{R_b} + \frac{4kT}{R_f} + 2qI_d)(\frac{1}{\omega C_f})^2 df + \left[\frac{4kT(2/3)}{g_m} + \frac{K_f}{C_g f}\right]\left(\frac{C_g + C_d}{C_f}\right)^2 df$$

$$= (\frac{4kT}{R_b} + \frac{4kT}{R_f} + 2qI_d)(\frac{1}{\omega C_f})^2 df + \frac{K_f}{C_g f}\left(\frac{C_g + C_d}{C_f}\right)^2 df + \frac{8kT}{3C_f^2}\frac{(C_g + C_d)^2}{g_m} df \quad (3.15)$$

In order to minimize the noise, the last two terms should be minimized. The middle term is minimized by the choice of $C_g$=$C_d$. The minimization of the last term is depended on the ratio of $C_g/g_m$ of the JFET.

For a given CMOS technology, the transconductance and input capacitance are given by,

$$g_m = \mu_n c_{ox} \frac{W}{L} V_{eff} \quad (3.16)$$

$$C_g = \frac{2}{3} C_{ox} WL \quad (3.17)$$

then (3.15) can be simplified to,

$$\overline{V_{total}^2} = (\frac{4kT}{R_b} + \frac{4kT}{R_f} + 2qI_d)(\frac{1}{\omega C_f})^2 df + \frac{1}{C_f^2}\left[\frac{16kTL^2}{9\mu_n V_{eff}} + \frac{K_f}{f}\right]\frac{(C_g + C_d)^2}{C_g} df \quad (3.18)$$

$\overline{V_{total}^2}$ is minimized when $C_g$=$C_d$.

The signal bandwidth from the detector is limited. The signal from a detector whose charge collection time is about a microsecond can never contain useful information on a time scale of nanoseconds. Low-pass filtering of the output of the detector can eliminate the high frequency noise. Similarly, low-frequency noise pick-up (power line) can also degrade the signal-noise ratio. So pulse shaping is usually used to remove as much broad spectrum noise as possible without severely attenuating the useful signal from the detector. The pulse shaping is normally carried out through a combination of differential and integrating circuits, which are regarded as high-pass and low-pass filtering, respectively.

The effect of pulse shaping on signal-noise ratios was theoretically studied by E. Kowalski [9] and P.W. Nicholson [10]. The best possible signal-to-noise ratio is achieved if the signal pulses are shaped to the form of an infinite cusp. But in practical world, the pulse shape must have finite width; other shaping methods should be used. Table 3.1 lists some pulse shaping and the noise-to-signal ratio F relative to Infinite Cusp Pulse Shaping.[1]

| Shaping method | Infinite cusp | Triangular | DL-RC | CR-RC | CR-$(RC)^4$ |
|---|---|---|---|---|---|
| S/N ratio Factor | 1 | 1.075 | 1.098 | 1.359 | 1.165 |

Table 3.1 Various pulse shapes and their S/N ratio factor relative to the infinite cusp

The basic CR-RC network is mostly widely used because it is easy to implement using operational amplifier. The amplifier frequency response is modeled by a CR-RC filter as follows,

$$A(\omega)=\frac{A_0\omega\tau}{1+\omega^2\tau^2} \tag{3.19}$$

where $\omega$ is the frequency, $\tau$ is the time constant of CR or RC network(as when the time constant of RC equals to the time constant of CR, the best S/N is achieved, usually the same time constant $\tau$ for CR and RC is chosen). $A_0$ is a constant relative to the gain of the network.

Using previous equations (3.15) and (3.19), when CR-RC shaping network is applied to the total noise output of pre-amplifier, the noise output of the shaping network is given by:

$$\overline{V_{shaping}^2}=\int_0^\infty A^2(\omega)\overline{V_{total}^2}d\omega=A_0^2\left[\left(\frac{kT}{2R_b}+\frac{kT}{2R_f}+\frac{qI_d}{4}\right)\frac{\tau}{C_f^2}+\frac{K_f}{2C_g}\left(\frac{C_g+C_d}{C_f}\right)^2+\frac{kT}{3g_m\tau}\left(\frac{C_g+C_d}{C_f}\right)^2\right] \tag{3.20}$$

from (3.20), by selecting an optimum $\tau$, the noise can be minimized, rewriting the (3.20) to

$$\overline{V_{shaping}^2}=\frac{A_0^2}{C_f^2}\left(S_1\tau+\frac{S_2C_T^2}{C_g}+\frac{S_3C_T^2}{\tau}\right) \tag{3.21}$$

$$S_1=\left(\frac{kT}{2R_b}+\frac{kT}{2R_f}+\frac{qI_d}{4}\right),\ S_2=\frac{K_f}{2},S_3=\frac{kT}{3g_m}\ \text{and}\ C_T=C_g+C_d$$

Differentiation to find the minimum yields,

$$S_1\tau=\frac{S_3C_T^2}{\tau}\Rightarrow\tau=C_T\sqrt{\frac{S_3}{S_1}} \tag{3.22}$$

and the minimum noise is

$$\overline{V_{\min}^2}=\frac{A_0^2}{C_f^2}\left(C_T\sqrt{S_1S_3}+\frac{C_T^2S_2}{C_g}+C_T^2\sqrt{S_1S_3}\right) \tag{3.23}$$

The total noise is usually expressed by using the concept of equivalent noise charge(ENC). It is defined as the charge signal at the input which will produce the same output as the RMS noise. ENC is usually presented in units of electrons RMS ($e_{rms}$) or as Full Width Half Maximum (FWHM) expression in eV.

$$FWHM(\text{eV in silicon})=2.35W^*\ e_{rms}=8.5\ e_{rms} \tag{3.33}$$

Figure 3.4 shows a typical charge sensitive preamplifier noise performance vs. shaping time constant.

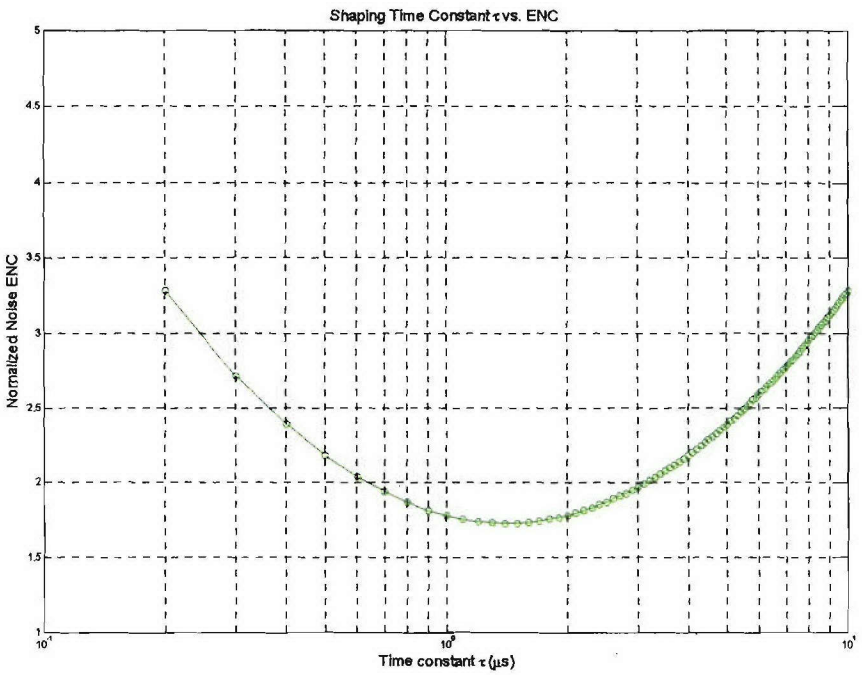


Fig.3.4 Charge sensitive preamplifier noise performance

# Chapter 4: The ΔE-E Particle Identification

## *4.1Bethe-Bloch Equation*

### 4.1.1 Interaction of Heavier Charged Particles

The loss of energy by charged particles traveling through a material is broken into two parts based on the mechanism of energy transfer- either collision or radiative energy loss. The total *stopping power* is

$$\frac{dE}{dx} = \left(\frac{dE}{dx}\right)_{col} + \left(\frac{dE}{dx}\right)_{rad} \tag{4.1}$$

where $(dE/dx)_{col}$ is the electronic energy loss due to Coulomb interaction (i.e. ionization and excitation), and $(dE/dx)_{rad}$ is the nuclear energy loss (e.g. due to emission of Bremsstrahlung radiation, and nuclear interactions).

Heavy particles lose their energy essentially by Coulomb interaction with the nuclei and electrons of the absorbing material. The stopping power of heavy particles such as protons and alpha particles is given by Bethe-Bloch formula

$$\frac{dE}{dx} = -2\pi N_a r_e^2 m_e c^2 \rho \frac{Z}{A}\frac{z^2}{\beta^2}\left\{\ln\frac{2m_e c^2\gamma^2\beta^2 W}{I^2} - 2\beta^2\right\} \tag{4.2}$$

Na is Avogadro's number
Z is the atomic number of the absorbing material
A is the atomic weight of the absorbing material
ρ is the density of the absorbing material
z is the charge of the incident particle
$m_e$ is mass of electron
I is the mean excitation potential
The maximum energy transfer W is given by

$$W = \frac{2m_e c^2\eta^2}{1+2s\sqrt{1+\eta^2}+s^2} \tag{4.3}$$

$$\eta = \gamma\beta, s = m_e/M$$

$$\gamma = \frac{1}{\sqrt{1-\beta^2}} \tag{4.4}$$

$$\beta = \frac{v}{c}$$

c is the speed of light
v is the speed of particle
M is the mass of incident particle

### 4.1.2 Interaction of Electrons

The interaction of electrons with matter is slightly more complex than for heavy ions. Because it is necessary to consider radiative processes in addition to the inelastic electronic collisions. Moller and Bethe have established an equation giving the specific energy loss for an electron of energy E, which is

$$\frac{dE}{dx} = -\frac{2\pi q^4 NZ}{m_e v^2}\left\{\ln\left(\frac{m_e v^2 E}{2I^2(1-\beta^2)}\right) - \left(2\sqrt{1-\beta^2} - 1 + \beta^2\right)\ln(2) + 1 - \beta^2 + \frac{\left(1-\sqrt{1-\beta^2}\right)^2}{8}\right\} \quad (4.5)$$

where q is the unit electrical charge
other quantities are as defined in (4.2-4.4)

***4. 2 Particle Identification***

For a thin detector which is penetrated by a charged particle, the energy deposited within the detector can be calculated from:

$$\Delta E = \left(-\frac{dE}{dx}\right)_{ave} \cdot t \quad (4.6)$$

where t is the thickness of the detector and $(-de/dx)_{ave}$ is the linear stopping power average over the energy of the particles while in the absorber. If the energy loss is small, the stopping power does not change much and it can be approximated by its value at the incident particle energy.

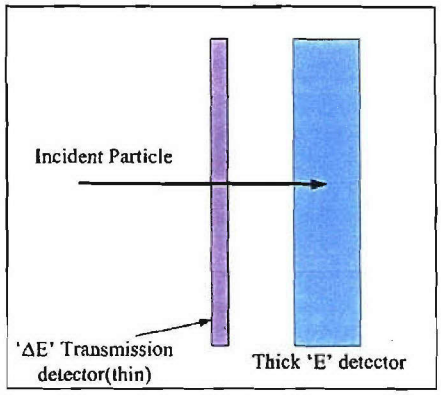


Fig. 4.1 ΔE-E particle indentification telescope

For nonrelativistic charged particles of mass *m* and charge *ze*, Bethe-Bloch formula (4.2) can be written in another format[1],

$$\frac{dE}{dx} = C_1 \frac{mz^2}{E} \ln C_2 \frac{E}{m} \quad (4.7)$$

where C1 and C2 are constants. If we form the product $E\frac{dE}{dx}$, the result is only mildly dependent on the particle energy, but is sensitive to $mz^2$ value which characterizes the incident particle. If we use a telescope with a thin and a thick detector, arrangement diagrammed in Fig. 4.1, the responses of which are respectively proportion to the differential energy loss dE/dx and to the residual energy of the particle. Because the incident energy can be obtained by summing the pulse amplitudes from ΔE and E detectors, simultaneous determination of both mass and energy of each incident particles is therefore possible.

# Chapter 5: RENA chip

## *5.1 Introduction of RENA chip*

The Readout Electronics for Nuclear Applications (RENA) Integrated Circuit is a monolithic integrated circuit (IC) developed for x-ray and gamma ray sensor systems. The RENA IC has 32 parallel signal channels with, signal polarity control for use with either electron or hole collection from detectors. The input amplifier is optimized for a detector capacitance of 6 pF, but may be used with detector capacitances up to 50 pF. The Shapers' peaking time is digitally selectable, for optimum noise filtering, with peaking times geometrically spaced from 400 ns to 6 μs. Up to 16 RENA ASICs may be daisy chained together to make a system with 512 detector channels. Various trigger modes are available with a user-defined threshold over the full signal range of 50K electrons.[11]

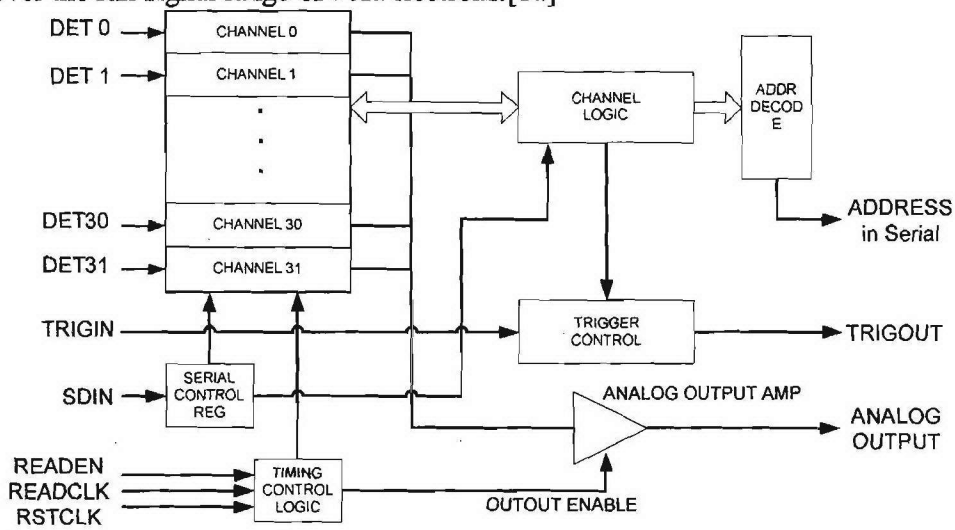


Fig. 5.1 RENA system diagram

## *5. 2 RENA System*

The RENA system block diagram is shown in Figure 5.1. There are 32 parallel Analog Signal Paths, which process the collected charge from 32 external detectors connected to the DET0-31 inputs. The processed analog signals are multiplexed and output through the Analog Output Amplifier. The Analog Signal Path and the Channel Logic are configured using a Serial Control Register. The inputs to the Serial Control Register are serial data input SDIN, and a clock SDCLK. RENA ASICs may have the control registers daisy chained by connecting the serial data output SDOUT from one chip to the SDIN of a following chip. The Serial Control Register is

used to configure the following items:

A. Shaper Peaking Time
B. Polarity of Input Charge
C. Chip Level Calibration Input
D. Peak Detect or Follower Operation
E. Global Trigger enable

F. External Trigger Disable Mode
G. Near Neighbor Trigger Enable
H. Channel Enables (32)
I. Calibration Enables (32)

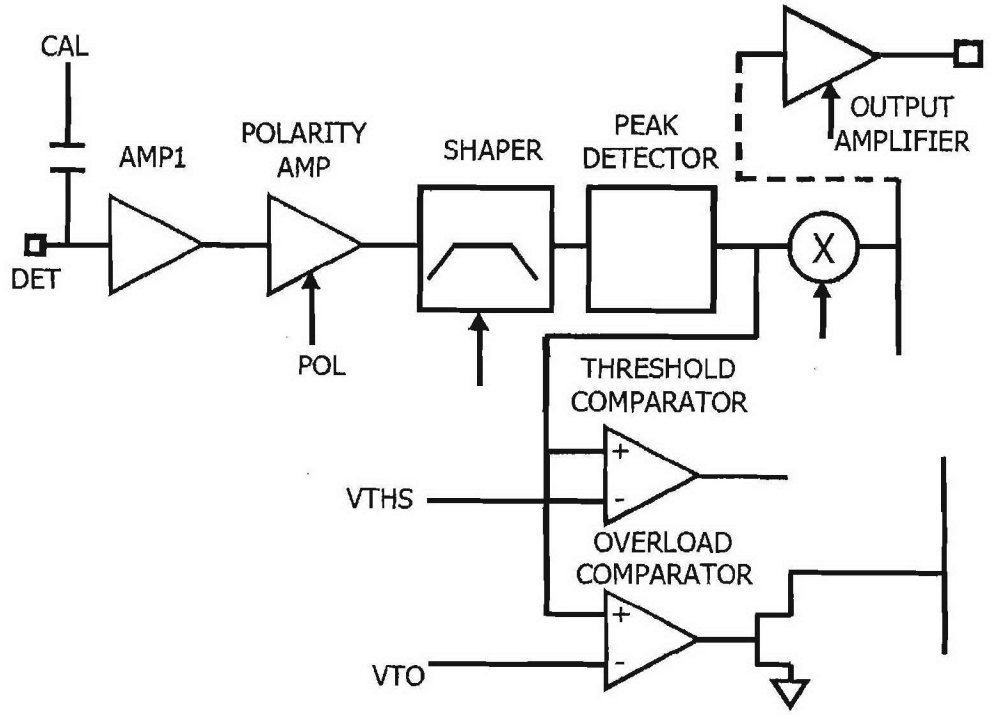


Fig. 5.2 Analog signal path of RENA

The Timing Control Logic block controls the operation of the RENA ASIC. There are three states of operation shown in the timing diagram in Figure 5.3. The first state of operation is the resetting of the Analog Signal Paths and Channel Logic Trigger Flags. This is accomplished by setting the RESET input high. After the chip is reset the channels wait for trigger events, which is the second state of operation. The Read Out of the triggered channels is the final state of operation.

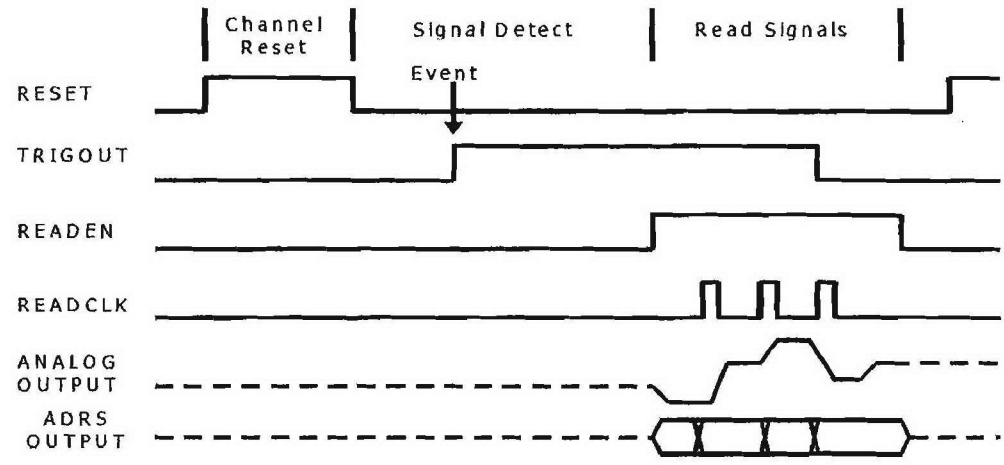


Fig. 5.3 Timing sequence of RENA readout

# Chapter 6: preliminary Results

## *6. 1 Thin detector amplifier*

### 6.1.1 High input capacitance charge sensitive amplifier

LCI sensor head uses one thin silicon detector in each telescope. The thickness of each detector is about 4-6μm and the area is 25mm$^2$. The capacitance of the detector can be as high as a few hundred pFs. A special charge sensitive amplifier is needed to match this high capacitance detector. As describe in Chapter 3, (3.15) gives the total noise of the amplifier. In order to minimize it, larger $g_m/C_g$ ratio JFET should be chosen and $C_g$-$C_d$ matching should be considered.Fig.6.1 shows one channel of thin detector amplifier. A250F and A275F are special hybrid op-amp from Amptek.

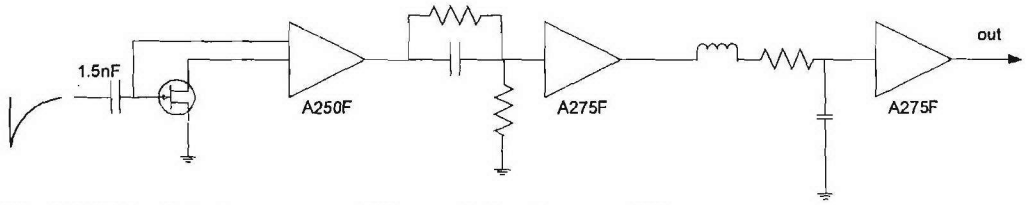


Fig.6.1 Thin detector pre-amplifier and shaping amplifier

Table 6.1 list three low noise JFET candidates for the pre-amplifier. All of them have large transconductance and high input capacitance which are good for high capacitance detector. Using these JFETs, noise of the pre-amplifier is measured in

Fig. 6.2 setup. FWHM is measured for each pre-amplifier. 2N6550 has similar noise as IF3601.

| Parameter | IF3601 | 2N6550 | IFN147(2SK147) |
|---|---|---|---|
| $g_m$(ms) / Id (mA) | 750 | 40/10 | 40/5 |
| $g_m$(ms) / Id (mA)(measured) | 52/3;80/5 | 32/3;40/5 | 21/3;26/5 |
| $I_G$ (nA) | 0.1 | 3 | 1 |
| Ciss (pF) | 300 | 30 | 75 |
| $e_n$ ($nVHz^{-1/2}$) at 1kHz | 0.3 | 1.4 | 0.75 |
| $I_n$ ($fAHz^{-1/2}$) at 1kHz | | 100 | |
| FWHM(keV) (Cin=472pF,$\tau$=1$\mu$s) | 19.8 | 18.8 | 28.4 |

Table 6.1 relevant specification for JFETs

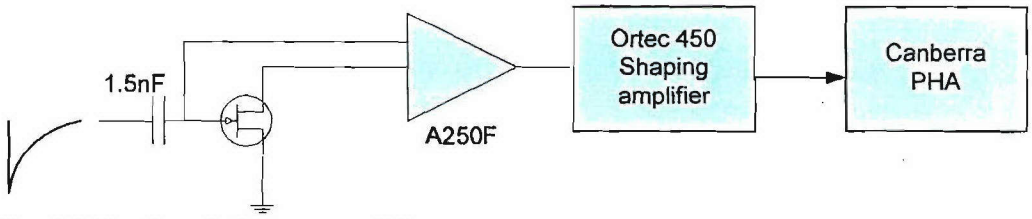


Fig. 6.2 Test bench for pre-amplifier

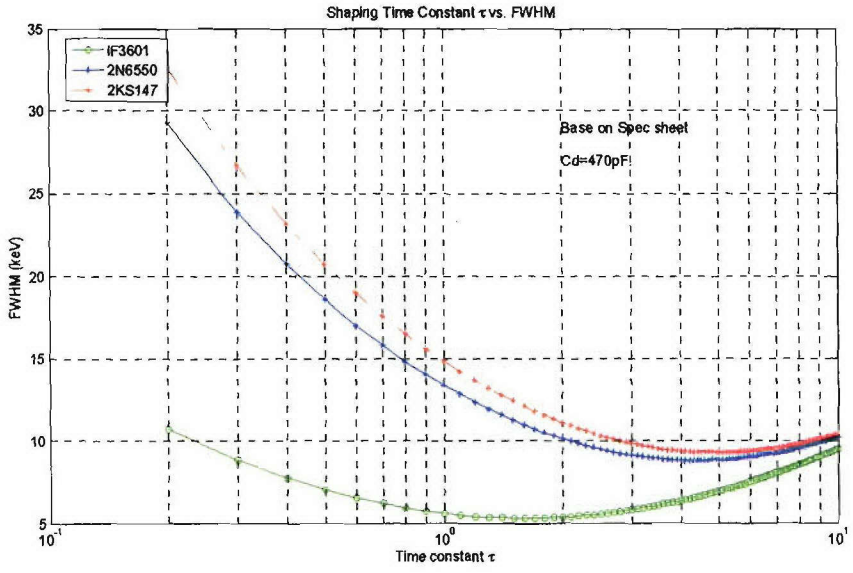


Fig.6.3 FWHM of pre-amplifier of 3 JFET based on spec sheet

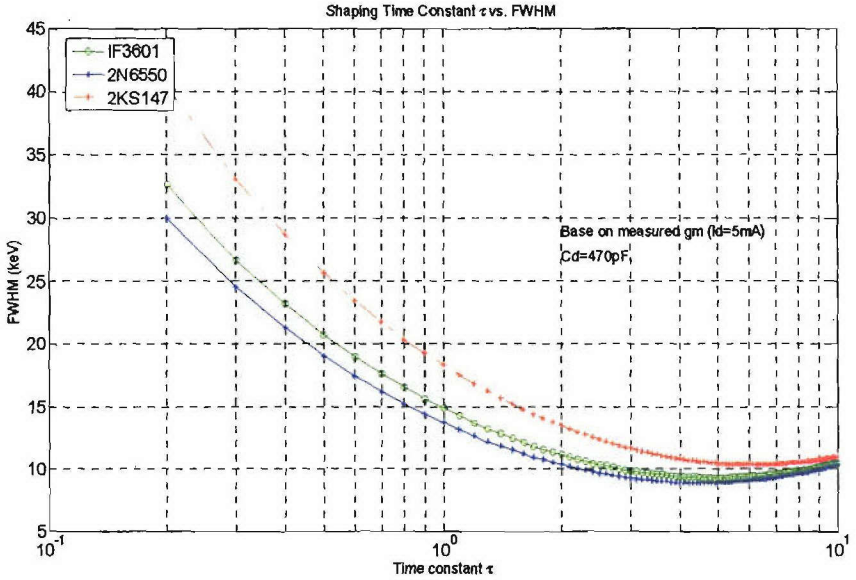


Fig.6.4 FWHM of pre-amplifier of 3 JFET based on measured transconductance at $I_d$=5mA

There is a big difference of the FWHM plot for IF3601 on Fig.6.3 and Fig. 6.4, because the transconductance of the FET is only 80mS which is much lower than the 750mS on the spec sheet. The transconductance will drop down with the drain current decrease. The 750mS is applicable only when the drain current is much higher than 5mA (>100mA).

### 6.1.2 Reduce the noise level of pre-amplifier

From the previous plot of FWHM for the 3 JFET, 2N6550 has the lowest noise level. The measurement also proved it. In order to achieve the best noise performance, parallel connected JFETs may be used. Fig. 6.5 shows the calculation of FWHM for different JFET combination of pre-amplifiers. Shaping time constant is 1us and total drain current is 5.75mA. A pre-amplifier with 2 JFET 2N6550 is tested and FWHM 16.0keV is achieved at $I_d$=2.875mA (for each FET), $C_d$=472pF. Increasing the number N (>2) of parallel JFET does not help the FWHM, because the transconductance will drop when drain current decreases. Drain current of each JFET is $I_d$_total/N.

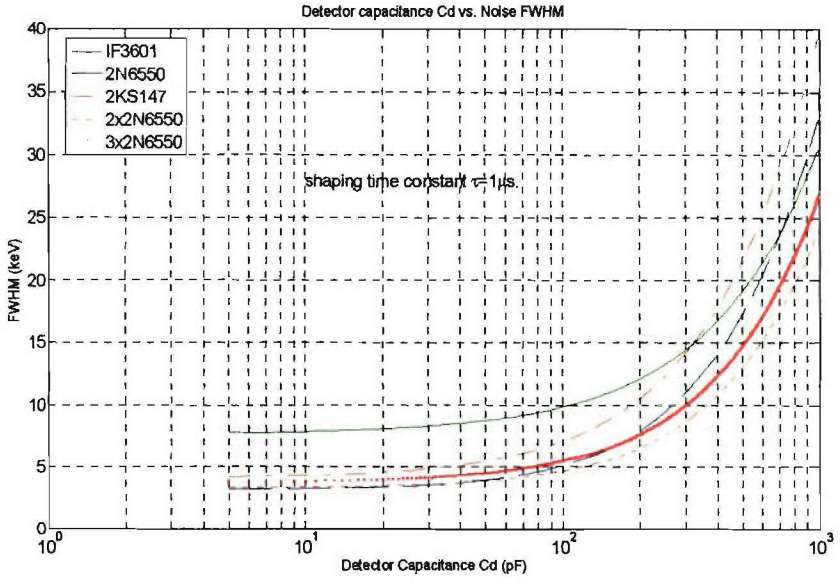


Fig.6.5 comparison of FWHM of pre-amplifier with parallel JFET based on measured transconductance. ($I_d$_total = 5.75mA)

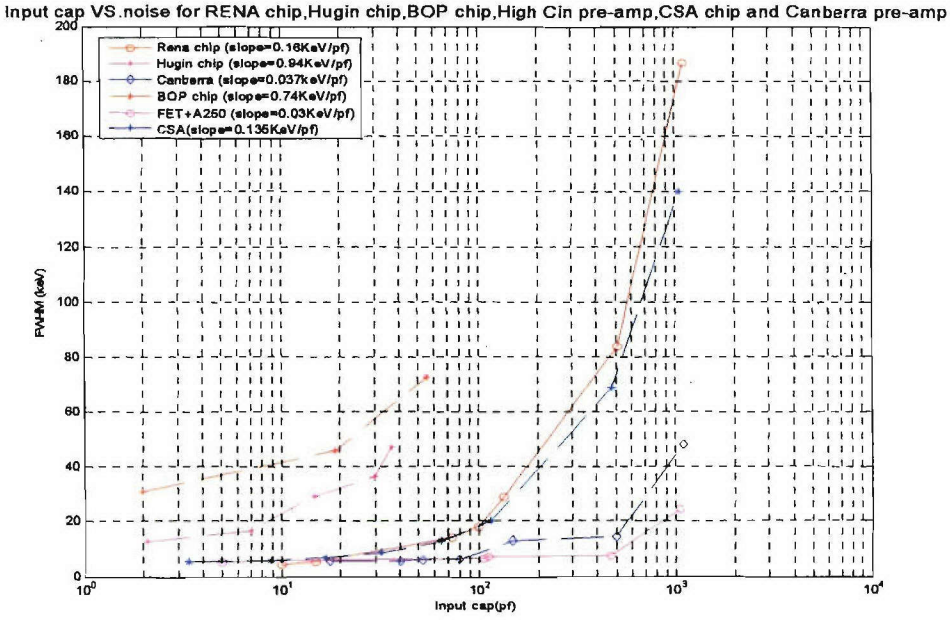


Fig.6.6 Comparison of FWHM of different pre-amplifiers

### 6.1.3 Thin detector signal channel electronic

The signal from the thin detector is amplified by pre-amplifier and the output of the pre-amplifier goes to two shaping amplifier: one fast shaping and one slow shaping. The slow shaping is 3-pole shaping circuit with 1μs shaping constant. Base line restore (BLR) is used to compensate the DC base line shift. Peak and hold

detector (PH300) detects the peak of the shaped pulse and send it to 8-bit ADC (AD7821). The pulse height is digitized to 8 bits and 1 overflow bit.

The fast shaping channel is a 3-pole shaping circuit with 500nS time constant. A single level discriminator (A150) connects to the output of the fast shaping and output a fast pulse train to DPU. Three discriminator outputs from 3 telescopes are latched and transferred to a shift register as address. The shift register is clocked by DPU and the ADC data and address can be shift out to DPU for further processing.

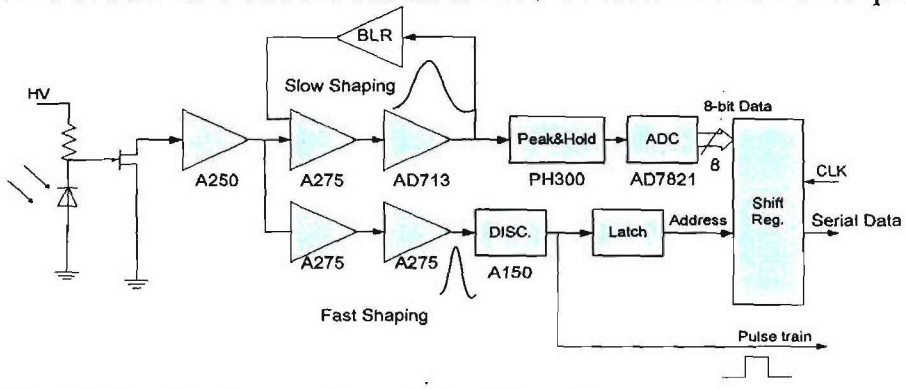


Fig. 6.7 One thin detector channel signal flow diagram

## *6.2 Thick detector amplifier (RENA)*

### 6.2.1 Thick detector signal channel

There are 3 telescopes in each sensor head; each telescope has 6-pixel detectors. There are 18 Si detectors in each sensor head. The capacitance of each pixel is about a few pico farads. The RENA chip is designed for Si, CZT, Ge, etc detectors with a few pico farads to 50 pico farads. The 32 channels in RENA can handle all 18 detectors. All the channels are self-triggered. The charge signal from the detector is amplified, shaped and the peak of the signal is held at the output. The address of the triggered pixel is simultaneously ready on the address bus of RENA chip. The trigger threshold is set by external 14-bit DAC. The analog output of RENA chip is digitized by 8-bit ADC.

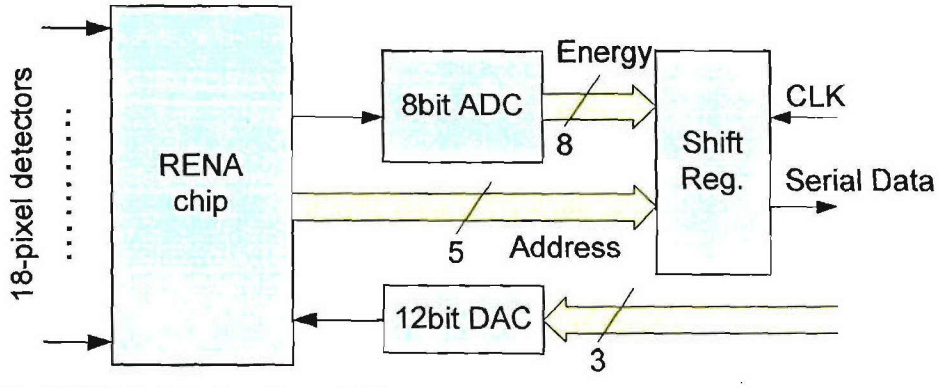


Fig.6.8 thick detector channel diagram

### 6.2.2 Characterization of RENA chip

RENA chip is characterized in the lab by the evaluation system in Fig. 5.9. Ortec research pulser simulates the signal from the Si detector. The pulse height data was collected by a computer and analyzed using Matlab. Fig.5.10 shows the FWHM of the RENA chip with 100keV and 250keV equivalent pulser input. The FWHM are 4.5keV and 8.2keV. Temperature test was also done in a thermal-chamber from -30°C to +35°C. The variance of FWHM is about 10% within this temperature range.

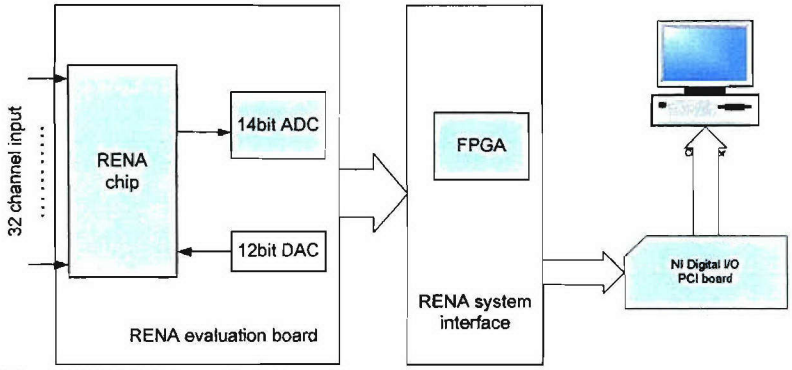


Fig. 6.9 RENA evaluation system

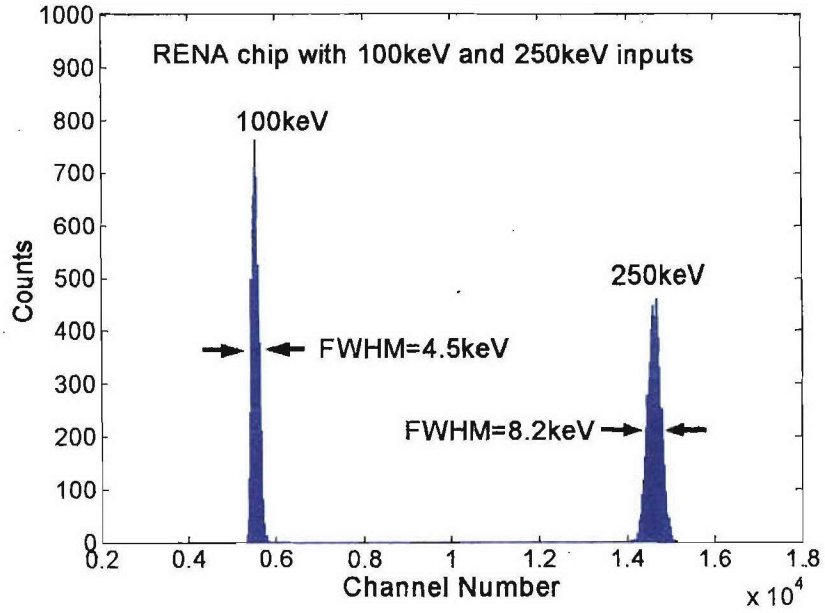


Fig. 6.10 Noise performance of RENA chip with pulser inputs

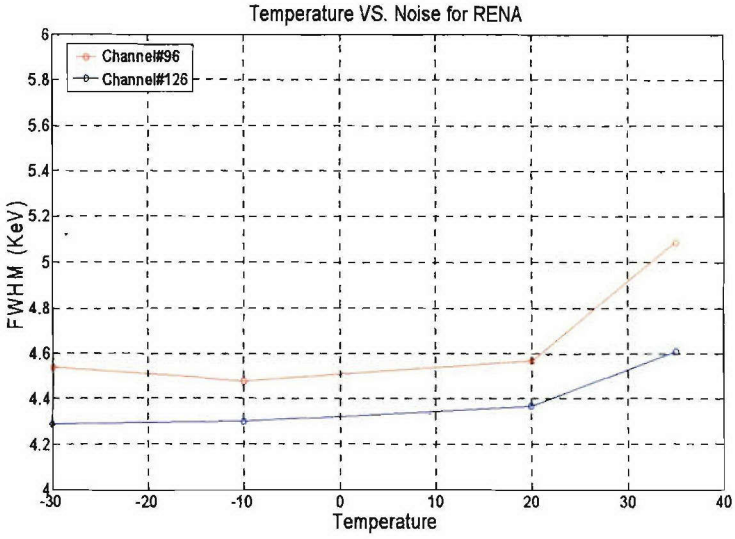


Fig.6.11 Temperature test of RENA chip

### 6.2.3 Pileup rejection of RENA chip

In order to test pileup of a channel, double pulsers with same amplitude and variable time interval are used. A double-pulser generator is applied to the input of RENA chip. The output of RENA is monitored by Canbeera PHA. Fig.6.12 shows the RENA output amplitude. We can see there is a pileup when the double pulse interval is less than 2us. When the interval is larger than 2us, the output amplitude is not affected by the 2nd pulser. Because the input channel shuts off at 2us, further signal input will not affect the output of that channel.

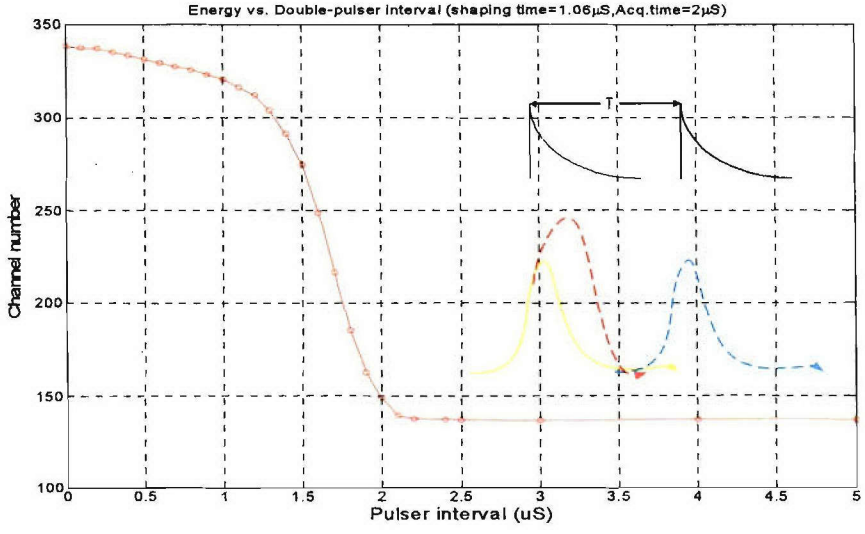


Fig. 6.12 RENA output amplitude vs. Double-pulse interval

## *6.3 HST*

### 6.3.1 Detectors in HST

Fig. 2.10 has shown the detector placement in the HST. There is a light tight Al/Mylar foil in front of the detector stack to block photons and ions. The front detector is a 1000μm Si detector, whose surface area is 962mm$^2$. The capacitance is about 97pF. The back detector has the surface area of 1256mm$^2$, which has same thickness. The capacitance of back detector is about 126pF. These detectors are placed in an Al/Tungsten collimator with 6.7 degrees view angle. The Al/Tungsten shielding also eliminate the background noise from omnidirectional particles.

### 6.3.2 Electronics in HST

High input capacitance pre-amplifier is used for HST detectors because of the high capacitance of the large area detectors. Fig.6.13 shows the electronic circuit diagram for the front detector. The slow shaping channel has 1μs shaping time constant to get best energy resolution. The pulse height is digitized by an 8-bit ADC. A 5-level fast discriminator is applied to the output of fast shaping channel which has 0.25μs time constant. The discriminator outputs the fast pulse trains to DPU so that a high counting rating can be achieved. The threshold levels of the discriminator is set to 20,40,80,160 and 320keV.

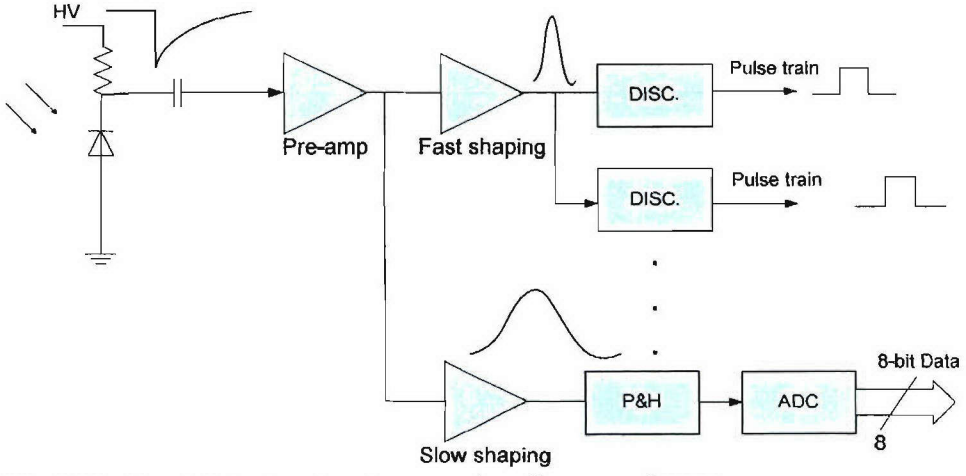


Fig.6.13 Front detector signal processing diagram of HST

### 6.3.3 Coincidence logic of HST

The energy information of particles is only taken from the front detector in HST. The back detector works as an anti-coincidence detector. If $A_0$ is the signal from front detector and B is the signal from back detector, only the signal, when $A_0$ is triggered and B is not, is processed. The front detector channel is gated by '$A_0 \bullet \overline{B}$' which shown in Fig. 6.14.

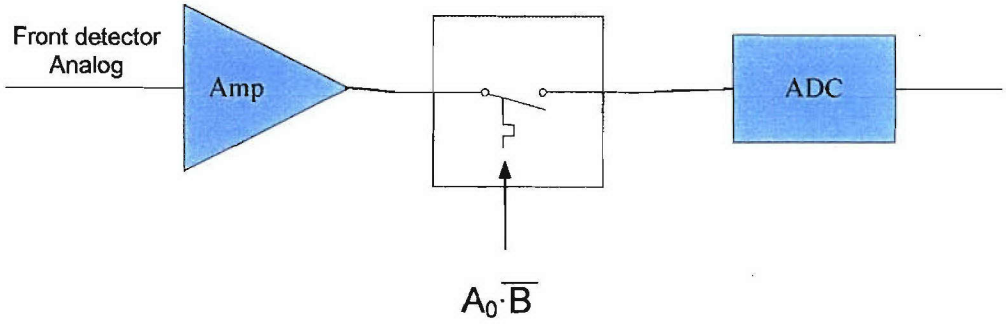


Fig.6.14 Front detector signal is gated by coincidence logic

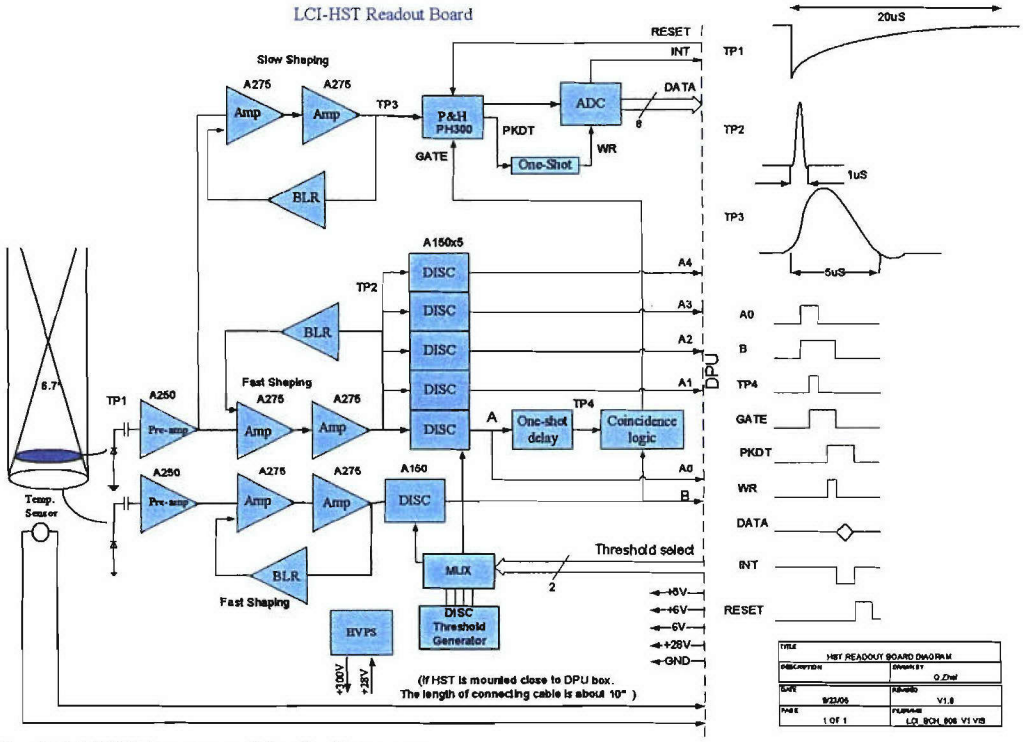


Fig.6.15 HST system block diagram

## *6.4 dE/dx simulation*

### 6.4.1 Bethe-Bloch equation simulation

Bethe-Bloch equation is given in Chapter 4. We will use 5μm Si detector in LCI sensor head. Assume the stopping power is uniform inside the thin detector. We can use Bethe-Bloch equation to simulate the energy loss in the thin detector (Fig.6.16). We can see the electrons deposit very small amount of energy in thin detector. Penetrated ions leave more energy depended on their $Z$ number, higher the $Z$, more energy is deposit in the detector.

If we plot Fig. 6.16 plot by energy in thin detector and thick detectors, it will be Fig.6.17. We can set energy thresholds for thin detector or energy matrix for both detectors according to the plot. Each energy pair can be a point on the plot. Particle identification can be done by matching the point to the curve.

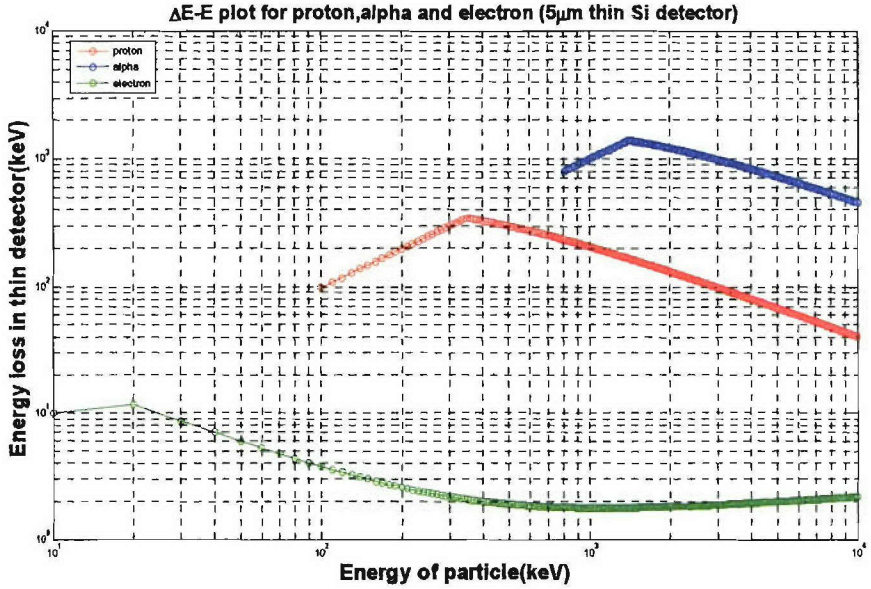


Fig.6.16 Energy deposit in thin detector

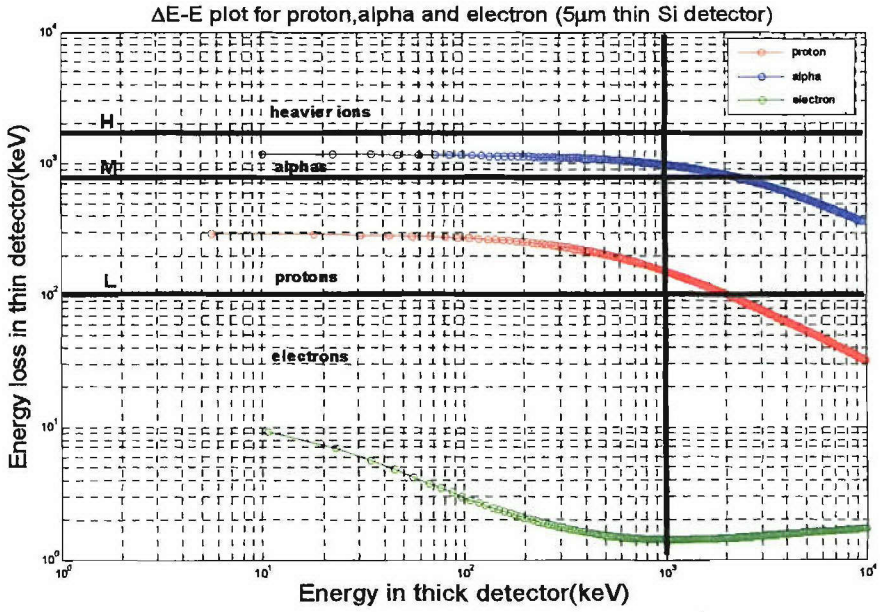


Fig.6.17 Energy deposit in thin and thick detectors

### 6.4.2 Monte Carlo Simulation

The Bethe-Bloch simulation is accurate to about 1% at high energy (>1MeV for proton). The accuracy decreases fast at low-energy level. GEANT4 Monte Carlo simulation is used to get more realistic results.

GEANT4 [12]is a toolkit for simulating the passage of particles through matter. It includes a complete range of functionality including tracking, geometry, physics models and hits. The physics processes offered cover a comprehensive range, including electromagnetic, hadronic and optical processes, a large set of long-lived particles, materials and elements, over a wide energy range from 250eV to TeV.

1. **Monte Carlo simulation for thin/thick detector stack (LCI)**

Fig. 6.18-6.19 shows the GEANT4 simulation for thin and thick detector stack.

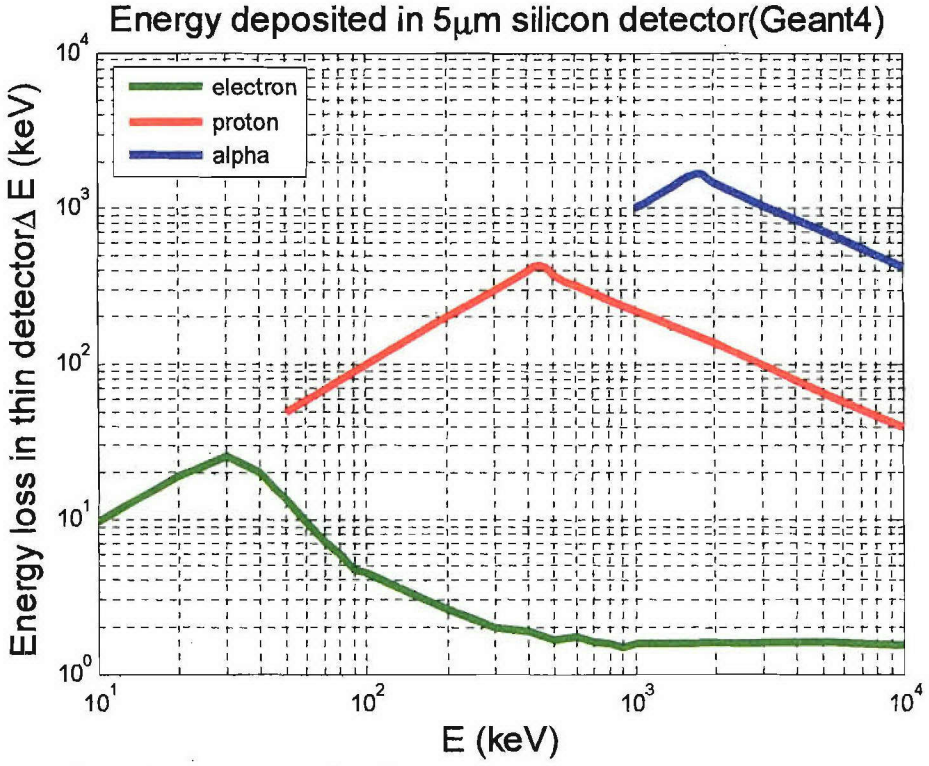


Fig.6.18 Mean energy loss in 5μm detector

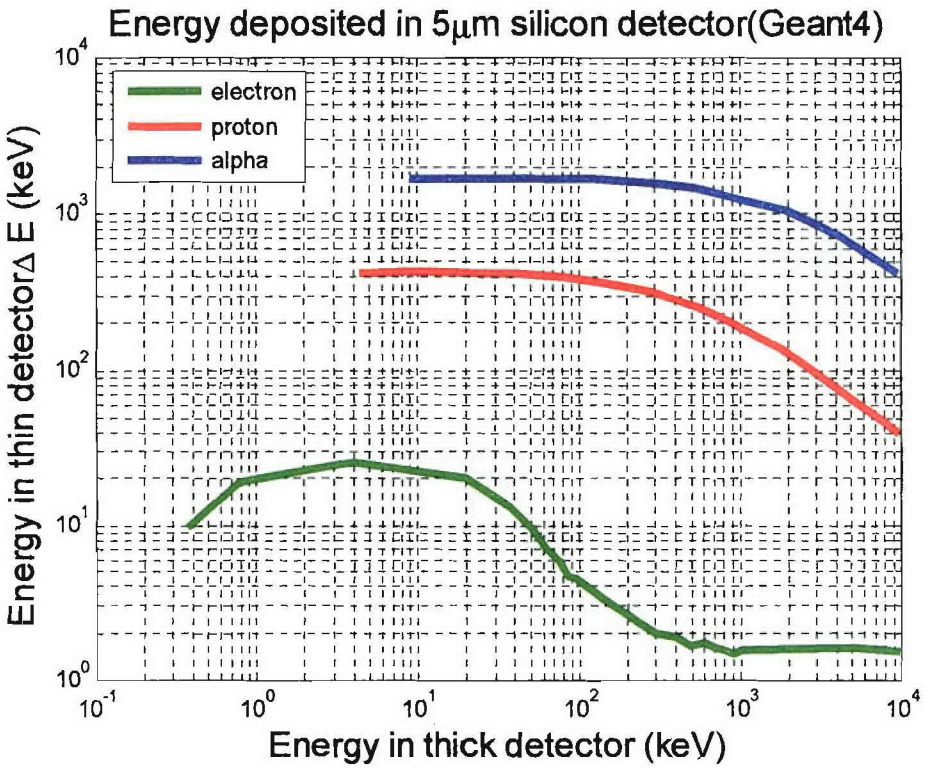


Fig.6.19 Mean energy in thin and thick detectors

## 2. Monte Carlo simulation for thick/thick detector stack (HST)

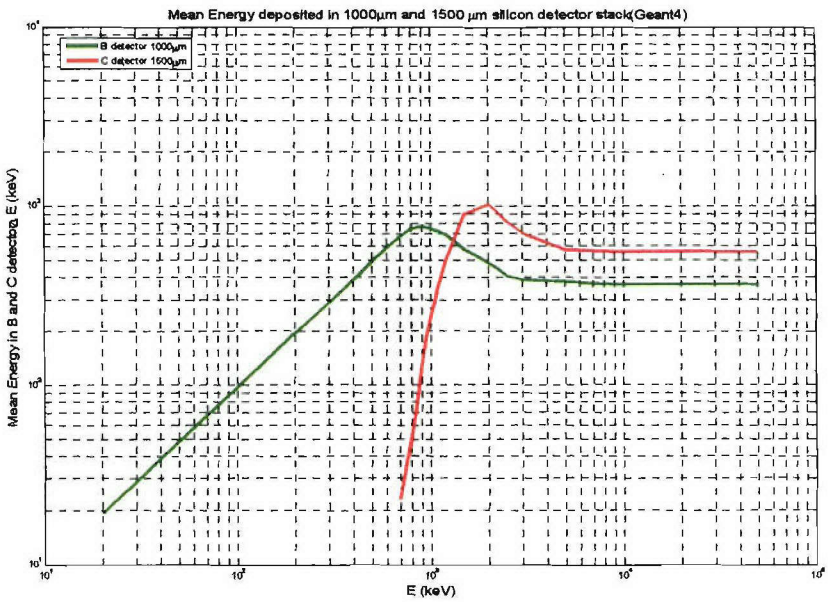


Fig.6.20 mean energy deposited in HST detector stack for electrons

Assuming only electrons can pass through the thin foil in HST, the detector stack will only response to electrons. Fig.6.20 shows the GEANT4 simulation of HST response to electron particles. Electrons with energy less than 600keV will be stopped by 1000μm front detector. Less than 5% 700keV electrons can pass through the front detector. When the energy goes higher, both front and back detector will be triggered, the anti-coincidence logic will get rid of these events.

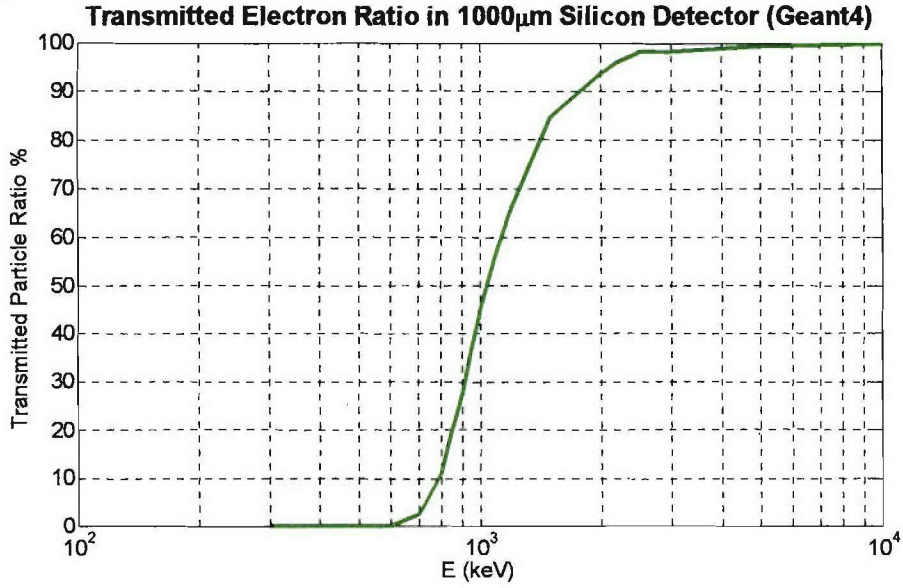


Fig.6.21 Electron penetrating ratio in 1000μm Si detector

# Chapter 7: Research Proposal

In our preliminary work, we have designed the preamplifier, analog signal processing circuitry for LCI and HST. We also measured the noise of the preamplifier with different front in JFETs. Preliminary Monte Carlo simulation has been done for the detector stacks.

In this research proposal, we propose to continue the work in the following areas:

- Implement the design of LCI and HST
- Test LCI sensor head with radiation source
- Further Monte Carlo simulation on LCI and HST

## *7.1 Implement the design of LCI and HST*

Printed circuit boards for LCI sensor head are being designed. The circuit board will be used as prototype. A thin detector channel evaluation circuit has been made and being tested to verify the function of the amplifier and logical function. The thick detector channel PCB has been sent out for manufacture. The RENA chip will be mounted on the PCB.

## *7.2 Test LCI sensor head with radiation source*

Am-241 is a 5.48MeV alpha particle source. We will use it to test the sensor head. Assume that the thickness of the thin detector is 5μm; 5.48MeV alpha particle will deposit a few hundred keV in the thin detector, the residual energy in the back detector is a few MeV. That will overflow the ADC in the thick detector channel. But we can still get particle composition information from the front detector.

Eu-155 and Am-241 X-ray source can also be used for calibration and test. Eu-155 has three peaks at 43KeV, 86KeV and 105KeV. Am-241 with a thick window, which blocks the alpha particles, has a 60KeV X-ray peak.

## *7.3 Further Monte Carlo simulation for LCI and HST*

In order to get better understanding the instrument response to energetic particles, we are going to develop our own instrument model including geometry definition and particle tracking within the detectors. Scatting effect of the thin foil and thin detectors will be analyzed in GEANT4 for LCI sensor head.

# Appendices

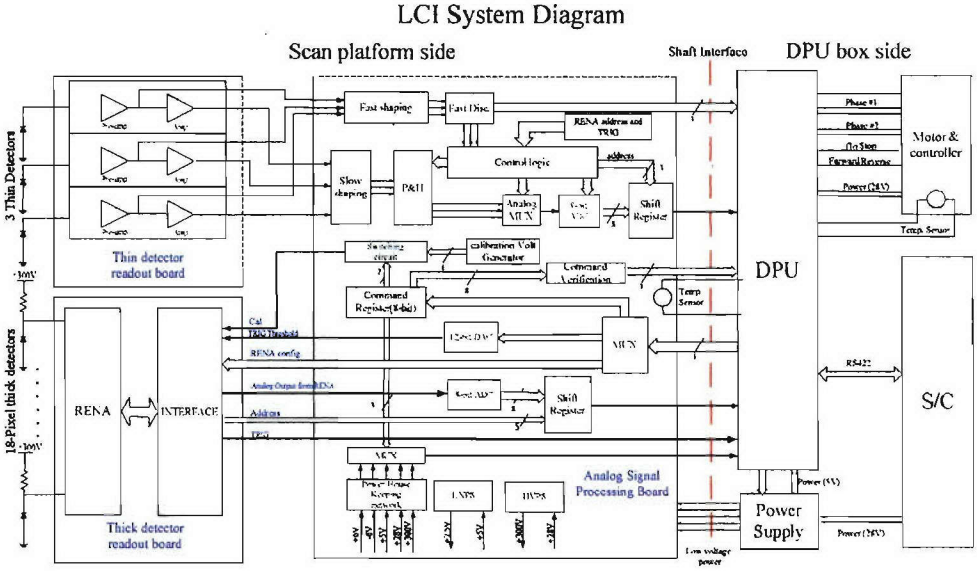


**LCI rotating head electronic system diagram**

**References:**


1. Knoll, G.F., *Radiation detection and measurement.* 1979, New York: Wiley. xv, 816.
2. W.SHOCKLEY, Czech. J. Phys, 1961. **B11**: p. 81.
3. H.Palevski, D.J.H., W.Kley and E.Tunkelo, Phsy,Rev.Letters 2, 1959: p. 258.
4. P.K.Iyengar, B.N.B.a., Phsy,Rev. 111, 1958: p. 747.
5. V.S.Vavilov, Phys.Chem.Solid 8, 1959: p. 223.
6. W.Schottky, Z. Physik, 1939. **113**: p. 367.
7. A.Coche, P.S., *Semiconductor Detector.* 1968: p. 107.
8. D.John, K.M., *Analog Integrated Circuit Design.* 1997: p. 214.
9. E.Kowalski, *Nuclear Electronics.* 1970.
10. Nicholson, P.W., *Nuclear electronics*. 1974, London, New York,: Wiley. xiv, 388.
11. Dale G. Maedinga, T.O.T., *Readout Electronics for Nuclear Applications (RENA) IC.* SPIE Symp. Proc., 1998. **3445**: p. 364.
12. S.Agotinelly, *Geant4-a simulation tookit.* Nucl.Instrum.Meth.A506:250-303,2003 2003.
13. Prof. James Sullivan's HST internal memo

# APPENDIX D: GSE DEVELOPMENT (D. Voss)

BOSTON UNIVERSITY

COLLEGE OF ENGINEERING

Thesis

# The Design of the Ground Support Equipment for the Loss Cone Imager

By

**DAVID LEE VOSS**

B.S. Taylor University, 2003

Submitted in partial fulfillment of the
Requirement for the degree of
Master of Science
2006

Approved By

First Reader

Theodore Fritz, Ph.D.
Professor of Astronomy and ECE

Second Reader

Anton Mavretic, Ph.D.
Retired Professor of ECE

Third Reader

Allyn Hubbard, Ph.D.
Professor of ECE

Fourth Reader

Mike Ruane, Ph.D.
Professor of ECE

**THE DESIGN AND DEVELOPMENT OF THE GROUND SUPPORT EQUIPMENT FOR THE LOSS CONE IMAGER**

**DAVID VOSS**

ABSTRACT

The Ground Support Equipment (GSE) has been designed to serve multiple functions in the development of the Loss Cone Imager (LCI), a particle detector instrument flying on the Deployable Science Experiments (DSX) satellite in 2009. The Ground Support Equipment's function can be broken into two phases: the development phase, and the testing phase. In the development phase the GSE is used to design and verify various components of the instrument including the Data Processing Unit (DPU), motors and motor drivers, and various circuit boards. In the testing phase the GSE accepts the data from the LCI instrument, stores, and parses the data for analysis. In this phase it will be used during environmental testing as well as satellite integration. The hardware used for the GSE is a National Instruments (NI) PXI chassis that houses a NI Pentium 4 computer, NI Data Acquisition Card, NI RS422 transceiver, NI 50 MHz waveform generator, Chroma Power Supply, and several in-house designed boards. The software was developed with NI Labview and Mathworks Matlab.

# TABLE OF CONTENTS

# LIST OF TABLES

# LIST OF FIGURES

## Introduction

The Ground Support Equipment (GSE) is used in the design and development of the Loss Cone Imager (LCI), an instrument being flow upon the Deployable Science Experiments (DSX) satellite in 2009. LCI is a particle imager that utilizes solid state detectors combined with a rotating interface that allows it to be able to image the entire sky in approximately five seconds. In addition to the rotating interface there is a fixed, large area, solid state detector used for looking at an area where low particle counts are to be expected.

The LCI is one of the instruments that will be coupled with a large, very low frequency (VLF) transmitter on the DSX satellite that will be used to better understand wave particle interaction and the subsequent interaction of these energetic particles in the atmosphere, particularly the ionosphere. The DSX satellite is funded by the United States Air Force Research Labs in collaboration with various academic and private organizations. The LCI instrument is being developed at Boston University through the efforts of professors, graduate, and undergraduate students.

The purpose of the Ground Support Equipment is to assist in the design and development of the LCI, as well as provide a platform for instrument designers to interface to the instrument during environmental testing, satellite integration, and initial in-orbit analysis. Due to the variability of the development of the instrument, this paper will focus on the second goal of the GSE which is to provide an interface to the DPU that emulates the satellite.

This document is broken up into three primary sections. The first section will deal with the theory of the DSX satellite and the Loss Cone Imager which involves the need for flying both the satellite and the instrument. The second section will deal with the hardware purchased and the hardware developed for the GSE and the rational for why it was chosen. The final section will discuss the software and modes of the GSE.

## Part 1 – GSE Design Requirements

Requirements are established to guide the design of the Ground Support Equipment. Functional requirements are high level requirements that define the purpose of the GSE. In order to achieve the functional requirements a set of sub-requirements are established to ensure the functional requirements are met. The GSE has five functional requirements as can be seen in Table 1.

**Table 1 - Functional Requirements of the GSE**

| | |
|---|---|
| F1 | To accurately simulate the DSX interface between the LCI instrument and the DSX satellite |
| F2 | To monitor the LCI instrument during environmental and integration testing |
| F3 | To simulate the LCI Sensor Head by providing known particle spectrum signals to the DPU for purpose of calibration of the DPU |
| F4 | To provide power profiles of the LCI instrument |
| F5 | To support the design and development of the LCI instrument |

## *F1 – Simulate the Spacecraft interface*

The first functional requirement allows the LCI instrument development team to both understand, and test the interface between the spacecraft and the LCI instrument. The interface simulates the signals that come from the spacecraft, and receives the signals coming from the LCI instrument. In addition to the electrical signals the GSE will mimic the mechanical interface for the cables. A list of requirements that make up the F1 Functional Requirement can be seen in Table 2.

**Table 2 - Sub-requirements for the simulate the spacecraft interface functional requirment**

| | |
|---|---|
| F1-1 | Provide one, fused, 28V power interface to the LCI instrument |
| F1-2 | Must interface to instrument through RS422, UART serial interface |
| F1-3 | Must be able to send a Pulse Per Second (PPS) once a second with a period accuracy of 1 μs |
| F1-4 | Ability to send all LCI commands to the instrument |
| F1-5 | Must be able to send spacecraft commands including the Time command, the VMAG command, and the VMAG offset/gain command. |
| F1-6 | Must store all commands sent to the LCI instrument with a time stamp of when the command was sent |
| F1-7 | Must be able to store all bytes sent to the GSE from the LCI instrument |
| F1-8 | Be able to extract and show housekeeping information sent to the GSE from the LCI instrument |
| F1-9 | Must connect to the LCI instrument through instrument connectors |

## *F2 – Environmental Testing and Integration Instrument Monitoring*

The GSE will be used for monitoring the health of the LCI instrument as it goes through a variety of tests. These tests include instrument vibration testing, thermal vacuum testing, and EMI testing. It will also be used for verification of proper function after it has been integrated on to the DSX satellite.

**Table 3 - Sub-requirements for the testing functional requirment**

| | |
|---|---|
| F2-1 | The GSE must be able to be accessed remotely |
| F2-2 | The GSE must be modular for the purpose of bringing it, and supporting electronics, to various testing locations |
| F2-3 | The GSE must be robust in design because of frequent transportation |
| F2-4 | The GSE must be powered from a standard 20 AMP receptacle |

## *F3 – Simulate the LCI Sensor Head*

The third functional requirement of the GSE is to test the accuracy and limits of the LCI DPU. This is needed to verify that the signals being sent from the LCI Sensor Head representing the particle information is accurately being stored and transmitted to the DSX satellite.

| | |
|---|---|
| F3-1 | Must send all signals from the Sensor Head to the DPU pertaining to the interpretation of particle data. This does not include Housekeeping data, or power lines |
| F3-2 | Must record all signals sent to the DPU and all signals received from the DPU |

## *F4 – Provide Power Profiles*

The GSE must provide detailed power profiles for all components of the LCI instrument, as well as power profile for the LCI instrument through all operational modes. The GSE must be able to see any power spikes with duration longer then 10 ms.

| | |
|---|---|
| F4-1 | Provide current and voltage monitoring on 28V interface(s) with the ability to see power spikes of duration 10ms or longer |
| F4-2 | Provide power for the LCI instrument subsystems with voltage and current monitoring on each line. (5V, 3.3V) for the DPU Board, (12V,-12V, 5V, 28V) for a Sensor Head, variable voltage for the motor (up to 32V). |
| F4-3 | Provide the ability to vary the 28V line -6V to +4V. |
| F4-4 | Provide over current protection for all powered lines with automatic power down if over current state exists. This can be through a fused design or through a constant current/voltage design. |
| F4-5 | Provide the ability to turn on/off individual powers lines |

## *F5 – Support the Design and Development of the LCI instrument*

In addition to fulfilling the above functional requirements the GSE can be used for testing and understanding lower level aspects of the instrument. This includes providing power to circuit boards, digital and analog inputs and outputs, and various data bus communication systems.

| | |
|---|---|
| F5-1 | |

# Part 2 – Ground Support Equipment Hardware

## *Introduction*

The ground support equipment (GSE) is a multi-faceted set of instruments that serves two purposes: first, the development of the instrument, and second, the testing of the instrument as an integrated system. The GSE assists in the development of the instrument by helping the designer to test his design and verify that the component of the instrument being developed is working properly. After the instrument has been integrated together the GSE is used for monitoring the instrument and verifying correct operation during system testing such as thermal vacuum testing, life testing, and other instrument functionality tests. The GSE will also initially be used to parse the LCI data packets being transmitted from the satellite to the ground. Because of these stated objectives, a complex set of instruments have been selected, and designed to meet the above testing requirements. Fulfilling the above requirements for testing and monitoring includes power monitoring, data transmission, both high frequency and low, and a variety of other capabilities. In the below sections each component of the GSE will be discussed and its role in the fulfilling the stated objectives of the system.

## *Purchased Hardware*

There are a large number of providers for integrated instruments; however, due to our desire to use the GSE in various places we wanted a mobile unit. The mobile unit must be able to perform all of the objectives of the GSE, but must not require a large

effort in moving instruments around. For this reason PXI (PCI eXtensions for Instruments) was chosen. PXI is an industry standard that is regulated by more then 65 companies[i], it is a modular, compact, rugged, high-performance solution that allows for mobile instrumentation and computing and is composed of three components: the Chassis, the Controller, and the Modules. National Instruments (NI) is known throughout the industry as a company that provides a large number of instruments capable of performing a large variety of functions in the PXI configuration. For this reason many of the instruments that we have chosen are NI instruments.

## PXI Chassis

The chassis provides a strong, rugged case, a high performance backplane, and a power supply. The backplane is a 132 Mbyte/s, 33 MHz, 32 bit PCI bus that connects the modules to the controller. The power supply offers

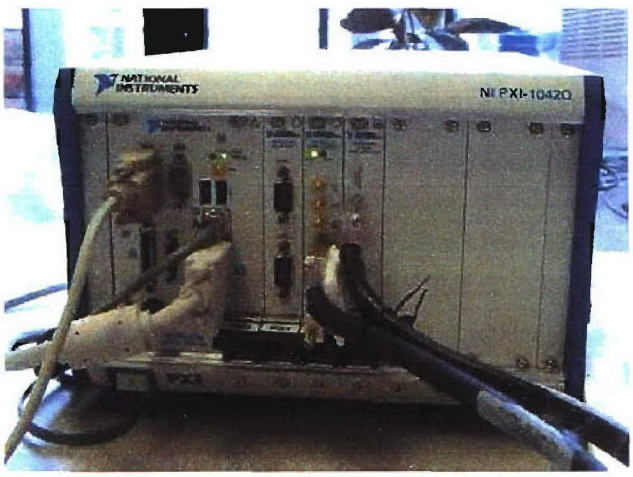


**Figure 1 - National Instruments PXI-1042 chassis**

a variety of voltages to each module including 5 Volts up to 2 Amps. The chassis has a built in cooling system that prevents the power supply, controller, and modules from

overheating. The PXI chassis that we purchased, as can be seen in Figure 1**Error! Reference source not found.**, is an 8-slot National Instruments PXI-1042.

## PXI Controller

There are two options for controlling the modules in a PXI chasses, an embedded controller, or a remote controller. We have decided to use an embedded controller that is the NI-PXI-8186. The specifications of the controller can be seen in Table 4. We decided to use the embedded controller for its rugged, integrated design. It would also, ensure that the modules would always be able to be controlled by a dedicated computer, a problem that arises in an academic environment. Also, all software that is applicable to the GSE will be loaded on this controller in a centrally located location. The processor is able to run under two operating Systems: Windows XP, or LabVIEW real-time. LabVIEW real-time gives the user the ability to operate the control software for the modules down to microsecond precision, something XP is not able to do because of the overhead associated with Window. Windows XP is able to provide approximately millisecond resolution in the controlling software. However, programs downloaded to the modules are able to run at significantly higher resolution. Because of

| | NI-PXI-8186 |
|---|---|
| CPU | 2.2 GHz Pentium 4-M |
| On-die cache | 512 KB |
| DDR RAM | 512 MB |
| Hard drive | 30 GB, minimum |
| 100 BaseTX Ethernet | 3 |
| GPIB (IEEE 488.2) interface | 3 |
| Serial ports | 2 |
| Parallel port | 3 |
| USB 2.0 ports | 2 |
| PS/2 keyboard/mouse connector | 3 |
| PXI trigger bus input/output | 3 |
| Operating system | Windows 2000/XP, |
| | LabVIEW Real-Time |

**Table 4 - NI PXI 8186 controller**

the low frequency of our testing and monitoring we determined that we would only need Windows XP and the LabVIEW real-time system. Functions that need to operate at higher frequencies are able to be performed through the modules functions. However, if at a later date that it is needed it is able to be purchased from NI and activated on our system.

## Chroma Power Supply

One of the required functions of the GSE is to perform accurate power monitoring, both for the overall instrument, and for the subsystems of the instrument. Although the PXI chassis provides four standard voltages to the modules we needed a variety of custom voltages and a method of monitoring both the current and voltage on each of these lines. We also needed the ability to switch on and off each of the voltages lines. The solution to these requirements resulted in a purchased power supply, and a custom switching board (the switching board will be discussed in a later section). The design and development of a power supply was discussed and initial began, but was later ruled out due to its complexity and the time frame of development. It was felt a better solution was to buy a fully functional supply. The unit we purchased is a Chroma 52914 DC power supply that fits into the PXI configuration and fills three slots. It has two channels that have the ability to be current or voltage limiting, software controllable, and full power monitoring. It also has a built in AC to DC converter so power is not taken from the PXI chassis eliminating the potential problem of maxing out the PXI power supply.

## Data Acquisition Module (DAQ)

The Data Acquisition Module (DAQ) was purchased from National Instruments for the purpose of assisting in the design of instrument subsystems in partial fulfillment of functional requirement F5. It also serves the purpose of controlling and monitoring the Power Switching Board discussed later in this paper. The DAQ board provides the ability to do voltage monitoring, low-speed, digital monitoring, digital controlling, and creating a voltage. The specifications of the DAQ chosen can be seen in Table 5.

**Table 5 - NI DAQ specifications**

| | |
|---|---|
| Part Number | NI 6251 |
| Bus | PXI |
| Analog Inputs | 16 |
| Input Resolution | 16bits |
| Max Sampling Rate | 1 MS/s |
| Input Range | ±0.05 to ±10 V |
| Analog Outputs | 2 |
| Digital I/O | 24 |

We also purchased an NI BNC-2120 breakout accessory sold with the NI DAQ card which can be seen in Figure 2. The breakout accessory provides an easy access to 8 analog input terminals, 8 digital I/O terminals, 2 analog output terminals, and a variety of other features built into the accessory for instrument monitoring and controlling.

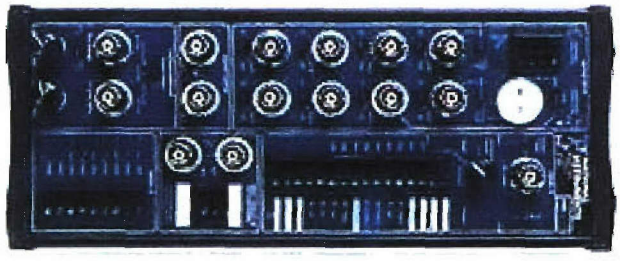

**Figure 2 - NI breakout board for the NI DAQ**

## High Speed Digital Waveform Generator

The High Speed Digital Waveform Generator is used through out the GSE to provide digital signals with microsecond precision. This accuracy is needed to fulfill requirement F1-3 and much of functional requirement F3. We purchased an NI PXI 6541 waveform generator that has 32 channels with the ability to transfer up to 50 MHz digital waveforms. Each channel is able to be selected individually for input or output, but all channels must operate at the same clock frequency. Digital outputs are able to be compatible with 5V, 3.3V, 2.5V, and 1.8V through a software selectable interface. An overview of the specifications for the NI 6541 can be seen in Table 6. Waveforms for the 6541 can be created in any program that creates arrays or spreadsheets and able to save it as a .txt file. LabVIEW is also able to read directly from MatLab, or Excel. LabVIEW will be able to read in the spreadsheet file, convert it to the proper format, and store the waveform to the waveform generators onboard memory. The user is able to control the waveform generator through an express VI in LabVIEW, or through custom VI's in LabVIEW.

**Table 6 - NI PXI 6541 Specifications**

| | |
|---|---|
| Part Number | NI PXI 6541 |
| Max Clock Rate | 50 MHz |
| DIO Voltage Compatibility | 5V, 3.3V, 2.5V, 1.8V |
| Number of channels | 32 |
| On board memory per channel | 1MB |

We also purchased a breakout board from National Instruments for the Waveform Generator to help facilitate instrument testing. The breakout board can be seen Figure 3. The breakout board is designed with header pins for all 32 signal lines as well as a

breadboard area for soldering in user defined chips. There are also connectors for Vdd, and ground that is available for powering any development chips.

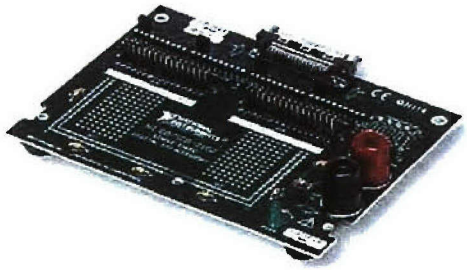

**Figure 3 - High Speed Waveform Generator Breakout Board**

## RS422 Data Card

The RS422 converter provides the GSE the ability to communicate to the LCI Instrument over a UART standard interface. This is required to fulfill the Functional Requirement F1 and its sub-requirements F1-1, F1-4, and F1-6. The Data Card was purchased from National Instruments and is able to be integrated into the PXI chassis. It is a two port card that is able to be accessed through LabVIEW, or any program that is able to communicate through a PC COM port.

**Table 7 - NI 8431 Data Card Specifications**

| | |
|---|---|
| NI Part Number | PXI 8431/2 |
| Baud Rate | 57b/s to 3Mb/s |
| Hardware buffer size | 128 B FIFO buffer |

## Pickering Prototype Board

The Pickering Prototype Board was purchased to provide access to the backplane of the PXI chassis, and to house the Power Switching Board in fulfillment of Functional Requirement F4. A picture of the prototype card can be seen in Figure 4. The card is laid

out for use by the Pickering Development board; however, we did not need the various accessories of the Development board, but only required access to the PXI backplane. The PXI backplane provides 12V, -12V, 5V, and Ground. It was determined to make a separate Power Switching board because of the lack of prototyping area on the Prototyping Board.

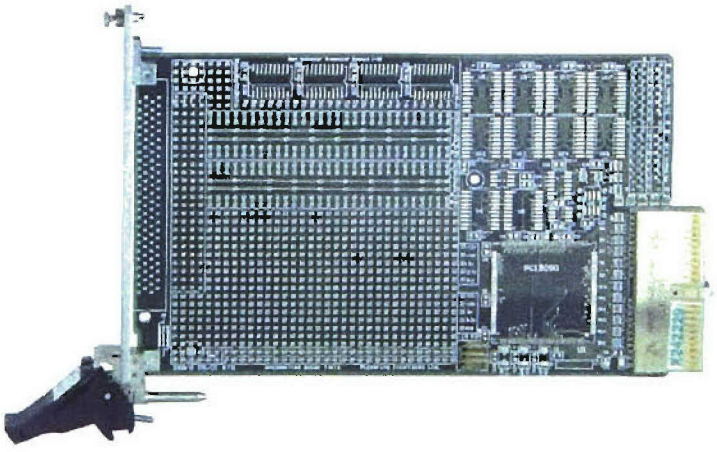

**Figure 4 - Pickering Prototype Card**

## Dell Latitude Laptop

It was determined a Laptop computer would be beneficial for the GSE during operation at remote facilities. The PXI Processor does not have a monitor so it was determined the laptop would provide a method of communicating with the PXI processor through the XP remote desktop feature. It was also determined the laptop would be a repository for extra data that may be generated and provide a method for backing up the data.

**Table 8 - Dell Latitude Specifications**

| Dell Part Number | Latitude |
|---|---|
| RAM | 512 MB |

| | |
|---|---|
| Processor | |
| Hard Drive | |
| Drives | 3.5 Floppy, DVD-R/W |
| Ports | 1 Serial, 1 Parallel, 4 USB, 1 VGA |

## *Developed Hardware*

### Power Switching Board

The Power Switching Board (PSB) was developed in order to fulfill Functional Requirement F4. The LCI instrument has a variety of power needs that necessitated the development of a custom GSE board in order to fulfill the requirements. A block diagram of the Board can be seen in Figure 5 where PXI cards control and monitor various parts of the PSB. On the right side of the block diagram is the output to the various parts of the instrument through the Connector Board.

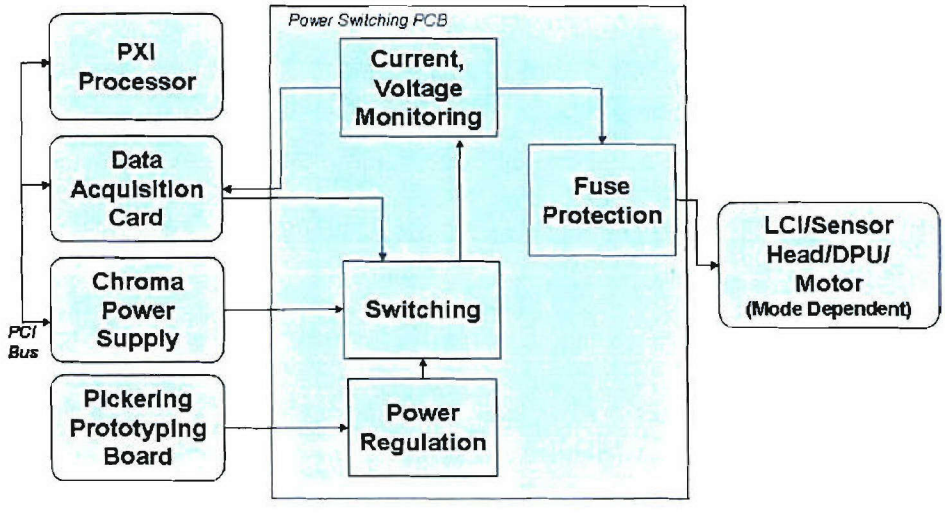


**Figure 5 - Block Diagram of Power Switching Board**

Items to place in Section:

1. which signal opens which voltage
2. explain the MUX
3. explain the current monitoring design
4. explain the fuses
5. connector pin out
6. schematic in appendix
7. Parts List in Appendix
8. table of input voltages and output voltages

## Connector Board

The Connector Board was designed to be an interface between the connectors of the various PXI cards, and the custom connectors of the LCI instrument. Due to requirement F2-3, and F2-4, it was determined that a PCB provides a more reliable, robust, and modular design then a complex custom cable. In addition to providing connections between the PXI cards and the LCI instrument, the Connector Board has a number of testing features built into the design as can be seen in Table 9.

**Table 9 - Testing features of the Connector Board**

| | |
|---|---|
| 1. | RS 422 drivers for simulating LCI external cables |
| 2. | Test headers on all connectors for oscilloscopes and digital waveform analyzers |
| 3. | Breadboard area with fused 5V and Ground |
| 4. | Extra DAQ ADC pins, DAC pins, and digital I/O pins brought to a header |
| 5. | Extra High Speed Waveform pins brought to a header |
| 6. | Shield pins on all LCI connectors able to be tide to ground of left floating |
| 7. | LED screen showing voltage and current on Mode 1 28V line. |
| 8. | LED's showing if data is be transmitted on the RS422 UART data line |

The LCI instrument is comprised of three modules that are separated from each other by approximately 2 meters. Interfacing the modules together are two cables that are exposed to electric and magnetic interference (EMI) from the transmitters on the satellite, and from the space environment. In order to be able to send high speed digital signals over this interface the LCI circuitry is equipped with RS422 differential line drivers.

However, to understand how the cable affects the signal the GSE is able to send and receive high speed, differential signals to characterize the cable.

Test headers were placed on all major data busses to allow for instrument developers to be able to use an oscilloscope or digital waveform analyzer to "listen in" on the data bus. This feature allows for debugging of software problems during instrument integration.

A bread-boarding area was designed into the board to accommodate for future testing applications. The breadboard area has a header next to it with a fused 5V and Ground that allows the user to either solder or wire wrap to.

The Data Acquisition Card (DAQ) and the High Speed Digital Waveform Generator that was purchased from National Instruments have more inputs and outputs then is currently needed in the LCI design. To be able to use these signal lines at a later time for testing and analysis, the lines have been brought to headers.

# Part 3 – GSE Software

## *Development Software*

- Talk about LabView
- Talk about Matlab
- Talk about the decision in choosing software

Ground Support Equipment software can be written in a variety of software packages, and computer languages. Decision of which software package to use is primarily dependent upon the requirements of the GSE, but also on cost of the software package, development time, and the familiarity of the developer with the various packages. Table

10 shows a list of various considerations that were taken into account in determining which software package to use. We looked at three basic software packages for the GSE: LabVIEW, MATLAB, and C++.

**Table 10 - Software Determination Matrix**

| | Software | | |
|---|---|---|---|
| | LabVIEW | MATLAB | C++ |
| Software company makes testing hardware | Yes | No | No |
| Software interfaces to standard testing hardware | Yes | Yes | Yes |
| Software has simple Graphical User Interface features | Yes | No | No |
| Selected software allows other software packages | Yes | No | No |
| Good data analysis software | No | Yes | No |
| Good technical support | Yes | Yes | No |
| Boston University has software | Yes | Yes | No |
| Developer familiar with software | Yes | Yes | No |

LabVIEW software was created by National Instruments and is a visual programming language by using objects or symbols to perform the programming. LabVIEW also supports the ability to nest MATLAB, of C++ routines in its "code" for added flexibility. National Instruments started out originally as a Data Acquisition Hardware company before expanding to include the LabVIEW software language as part of its products. Today, National Instruments creates dozens of various instrumentation boards in a wide variety of packages.

## *Mode 1*

### User Interface

S;lkfjs;lfkj

# APPENDIX E: ORIENTAL MOTOR TESTING (K. Matarese)

# LCI Vacuum Test w/ Load

**Motor:** Oriental Motor #2 (Serial TQ81VB3502)

**Operation:** 180° scan at 100 °/s

**Vacuum Pressure Range:** 35-45 μTorr

| | **Cycles**<br>1) Total<br>2) Loaded<br>3) No Load | **Temperature**<br>1) Loaded +/- 1 °C<br>2) No Load +/- 1 °C<br>3) Frame +/- 1 °C<br>4) Ambient +/- 1 °C | **Avg. Power**<br>1) Loaded (W)<br>2) No Load (W) |
|---|---|---|---|
| **In Vacuum** | 1) 350,000<br>2) 264,000<br>3) 86,000 | 1) 52<br>2) 51<br>3) 30.5*<br>4) 23 | 1) 6.8<br>2) 6.3 |
| **On Bench** | 1) 5,000**<br>2) 4000<br>3) 1000 | 1) 30.5<br>2) 30<br>3) 26<br>4) 23 | 1) 6.8<br>2) 6.3 |

* Measurement taken during loaded vacuum test

** Bench cycles were run in several different modes. The temperature numbers here correspond to a 180° scan at 100 °/s.

**Remarks**

The Oriental motor reached a peak temperature of 52.9 °C during loaded vacuum testing. This is a worst case estimate of the motor's steady state temperature in vacuum because our operational test mode uses more power than the planned flight modes. A subsequent test was run using 10°/0.1s incremental movements with 0.4 second delays for measurement, which is similar to the full-sky mode for the LCI. The result was a final temperature of 48.7 +/- 1 °C with an average driver power of 6.0 Watts.

Figure 1 shows the results of a 24 hour loaded vacuum test including motor temperature, frame temperature, and ambient room temperature. The equilibrium temperature is reached in roughly 10 hours. 24 hours equates to 24,000 cycles, where one cycle is defined as the motor turning 180° and back.

# LCI Vacuum Test w/ Load

Figure 1 – Loaded Temperature Results

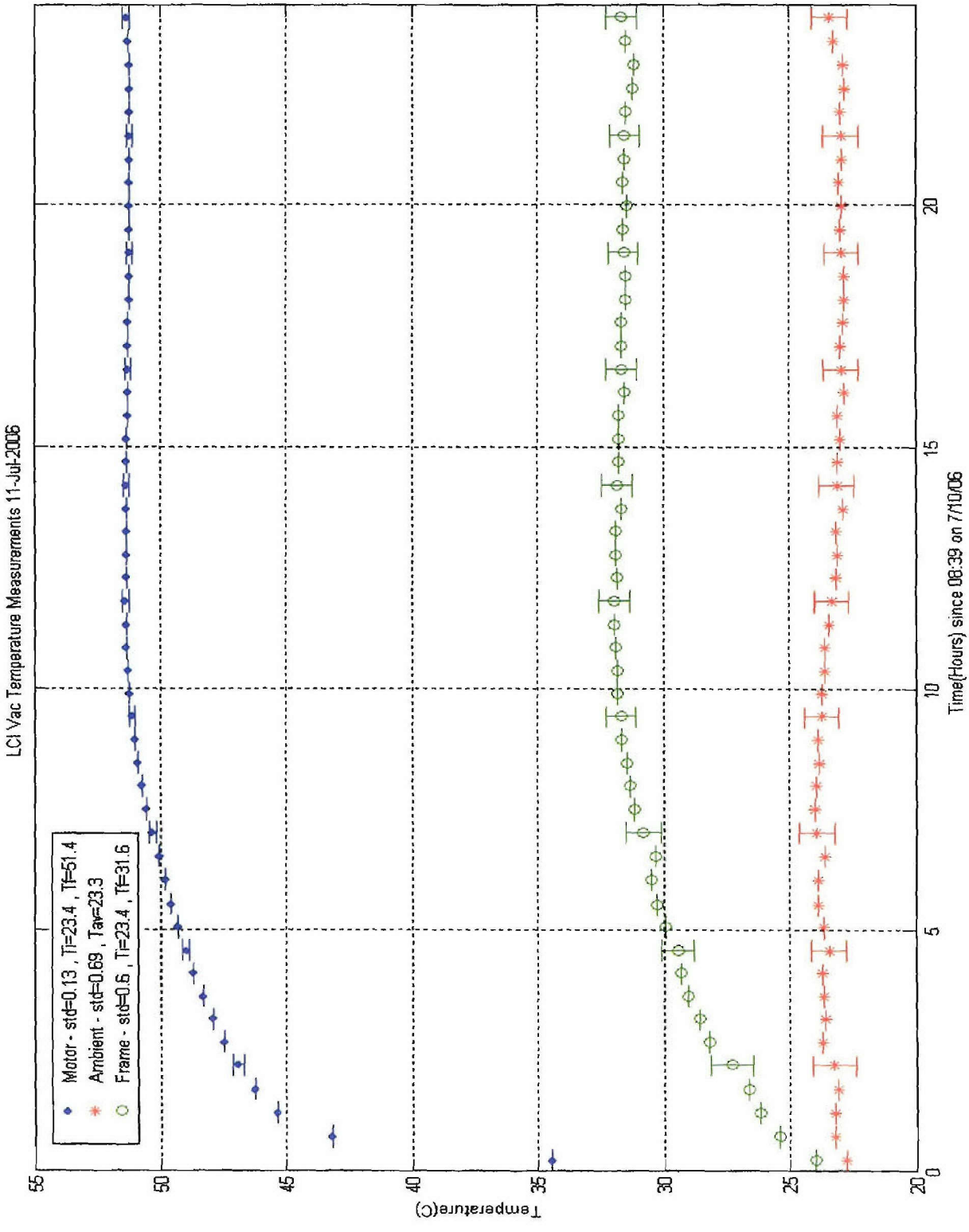

# LCI Vacuum Test w/ Load

**Motor Mount**

The mount was not thermally isolated from the chamber. Instead, we attempted to thermally isolate the motor from the mount using nylon mounting screws and kapton tape. The frame temperature was included in figure 1.

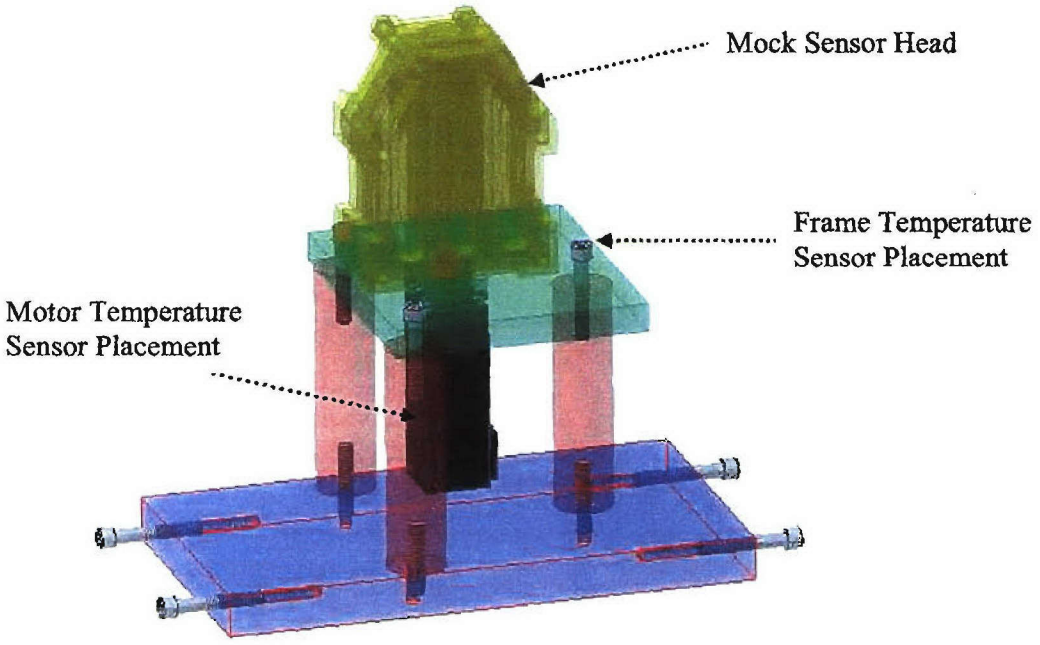


Figure 2 – Motor Mount

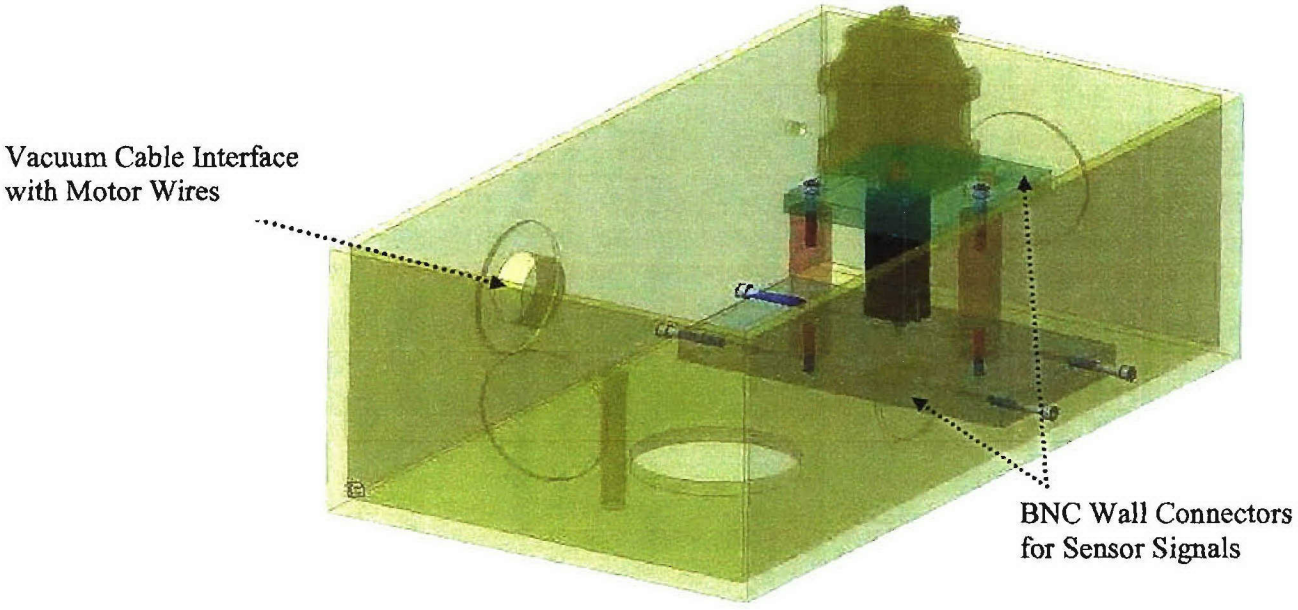


Figure 3 – Mount in Small Vacuum Chamber